ABSTRACT

Title of Document: Miniaturized Thin-Film Piezoelectric Traveling Wave Ultrasonic Motor

Ryan Quenon Rudy, Doctor of Philosophy, 2014

Directed By: Professor Don L. DeVoe, Mechanical Engineering

For many small-scale systems, compact rotary actuators are highly attractive. Many current millimeter-scale motor technologies, such as electrostatic motors and electromagnetic motors, operate at high speeds (on the order of 10^5 RPM) but low torque, usually pico- or nano-newton-meters. In order to drive large loads at speeds closer to 100 to 1000 RPM, gearing would be required, which drastically increases system complexity and size. Electromagnetic motors, which are effective at the macro-scale, become less practical at the millimeter-scale due to unfavorable scaling of energy density and complex fabrication. Electrostatic micro-motors require approximately 100 V for operation and produce limited torque. Traveling wave ultrasonic motors (TWUM) can provide micro- to milli-newton-meters of torque at low speeds and fill a necessary place within the millimeter-scale rotary motor landscape. Using recent developments in high quality piezoelectric film deposition and microfabrication techniques, TWUM can be made an order of magnitude smaller than currently possible.

The fabrication process for the TWUM is described within, with a focus on stator fabrication and the enabling fabrication methods developed for the manufacture of TWUM, including backside vapor-HF release, deep reactive ion etch footing release, and photoresist deep-trench refill. Design and characterization of the traveling wave stator component, both disc and ring are described. Disc stators, 1 to 3 mm in diameter, exhibited traveling waves up to 1 µm in out-of-plane amplitude with quality factors in air of 95. The design process for ring stators with mechanical impedance transformer tethers is presented. The tethers are designed to allow large motion at the stator perimeter, while tethering the stator to the anchored substrate. This mechanical impedance transformer tether allowed for an in increase in standing wave amplitude by over 100% compared to straight tethers. TWUM were demonstrated and characterized, and represent the smallest TWUM currently reported, at 2 to 3 mm in diameter and less than 1 mm thick. Motor performance characteristics are presented, with speeds exceeding 2000 RPM while consuming 4 mW of power at 10 V. These millimeter-scale motors have potential applications in fields such as fuzing, medical imaging, micro-robotics, and sensor steering and calibration.

Miniaturized Thin-Film Piezoelectric Traveling Wave Ultrasonic Motor

By

Ryan Quenon Rudy

Dissertation submitted to the Faculty of the Graduate School of the
University of Maryland, College Park, in partial fulfillment
of the requirements for the degree of
Doctor of Philosophy
2014

Advisory Committee:
Professor Don DeVoe, Chair
Professor Amr Baz
Professor Sarah Bergbreiter
Dr. Ronald Polcawich
Professor Ichiro Takeuchi
Professor Miao Yu

Acknowledgements

There are many people who were important in allowing this work to be completed. I start with thanking someone who I don't know, Andy Crouch, for giving me a big view of work, culture, and culture making, challenging that real artists ship, and for also providing great guidance in recognizing that there are often three groups, the 120, the 12, and the 3 that require great thanks from even the most secluded culture maker. Within the 120 (or so) that are peripherally connected to this work and my experience, I acknowledge Toshiiku Sashida and his invention of the traveling wave ultrasonic motor (TWUM), without which this work would never have started, and Anita Flynn, who laid the foundation for the miniaturization of the TWUM. Thanks are due to Takashi Kenjo, Sadayuki Ueha, Yoshiro Tomikawa, Chunsheng Zhao, and Kenji Uchino for their broad shoulders upon which this work stands, and to Amit Lal who initially funded the project under the ITMARS program. I must thank Martin Schmidt, who steered me away from his top ranked university toward a project I would enjoy. Thanks to Amr Baz, Sarah Bergbreiter, Ichiro Takeuchi, and Miao Yu for serving on my committee. I am grateful for my MEMS and Microfluidics Laboratory (MML) co-members, especially, Kunqiang Jiang, Chenren Shao, Renee Hood, Eric Kendall, Annie Lu, Omid Rahmanian, Jung Yeon Han, Alex Sposito, and Michael Weidroder. Special thanks are due to MML members Isaac Misri, Jason Felder, Mona Mirzaei, and Prakruthi Hareesh for their support and companionship throughout years of MEMS group meetings. This project would not be possible without the work of William Benard, Nelson Mark, Jim Mulcahy, Brittany Poetzsch, Madhu Roy, Nick Strnad, and Woody Windsor of the Army Research Laboratory (ARL) cleanroom staff. Thanks to Tony Ivanov, Dan Judy, Roger Kaul, Dan

Potrepka, Richie Piekarz, Sarah Bedair, Chris Meyers, Iain Kierzewski, and Rob Proie for their enabling work in PZT MEMS. Thanks to Matt Chin, Rob Proie, Simon Ghionea, Matin Amani, Lisa Ramsay, Mary Tellers, and Steve Hornbach for being my regular lunch companions and friends at ARL. I thank Kevin Offner, Carl Sanders, Jonathan Kreamer, Karie Cross, Rochelle Mellish, Elizabeth Hogsten, Renee Campbel, Eddie Hodges-Kluck, Mark Lai, Katie Willis, Andrew Flavin, Christina England, Rachel Lamb, Caitlin Williams, and Nathan Shumway for sorting out with me what it means to be a faithful graduate student. For their faithful support and friendship in so many ways I would like to thank Daniel and Melinda Seibert, Alex and Kira Hettinger, Adam and Adrienne Weaver, Bryant and Anne Webber, Nate and Julie Patrick, Scott and Stephanie Weidle, Bryan and Heidi Lewis, Allison James, Greg and Anna Glenn, Fred and Cecelia Hubach, Laszlo and Maria Korossy, Amber Marble, Rob and Liz Yancey, Sterling and Connie Mehring, Zack and Marj Koutsandreas, Stephen and Linnea Byers, Michael and Hannah Lyons, Melissa and Jerry Wang, Alicia Chen, Tom Carroll, Nick Lockard, Spencer Chang, Rik deVoest, Ryan Workman, Andy and Karen Myers, Paul Lauerman, Arpad Korossy, Elliot Chiu, Evan Chuang, Rob McNeely, Collin and Kristen Christensen, Caleb Shoultz, Aleks Brady, Peter Gilbert, Bready Johnston, Jack McCormack, Garrett Robinson, Ben Holloway, Corey Gray, Sara Chang, Laura Li, Grace Lee, Stephanie Chang, and David and Belinda Lee. For many times encouraging me toward diligence in my work and purity in my life, I would like to thank my accountability group: Dan Ware, Brandon Lacy, Jeff James, Josh Kester, Derek Marble, Andy Woo, Joseph Siagian, and Chase Wilkins. Thanks to Blair and Lisa Smith for constantly ministering to me and showing that there are bigger things than the biggest college rivalry. Thanks to Dave and Laura O'Connell for being such welcoming people who made a new state feel more and more like home, and for opening their home when things were at their worst. I greatly appreciate Bob Lynn, a great friend and mentor, who formed me like wet cement. I’d like to thank Terence Little, who has spent many hours with me mulling over our walks through life. Thanks are due to Sam Li, Liu Jing (Susan), and Li Yuenian (Richard) for their love and support as new members of my family.

For the twelve directly connected to this work and my experience, thanks to Brian Power, Joel Martin, and Steve Isaacson for direct fabrication support, and patience with me as I asked for the fourteenth time how to use a tool or run a process. Appreciation is due to the SMART Program Office for generous financial support and freedom to explore an area of research. Thanks to Kenn Oldham, who first piqued my interest in research and invested in me as an undergraduate researcher. Thanks to Brett Piekarski and Paul Amirtharaj, who took me on as an undergraduate, were instrumental in providing the infrastructure and environment for a successful project, and always challenged us to transition the project. Thanks to Jeff Pulskamp for extremely helpful (and long) conversations and great help in designing tethers and developing a model for the motors. I would like to thank Luz Sanchez for her excellent PZT, her constant companionship throughout the graduate school process, and always being good for stories and laughs. Thanks to Rachel Rudy for modeling dedication, hard work, and a goofy joy (most memorably relating to barbecue). To my parents, Mark and Sara Rudy, for being so present and caring, for algebra walks through the neighborhood, for playing “Equations” with me as a kid, and for supporting me with so much love.

I would also like to thank the three people most intimately involved in this work. Thanks to Don DeVoe for the initial idea and for pitching a project that convinced me to come to UMD, as well as always challenging me to develop professionally. To Ron Polcawich, thanks for your guidance and support, always-open door, and enthusiasm for our work together. Lastly, thanks to Gabe Smith, who performed much of the initial design and fabrication work, was always coming up with new ideas (often right before a mask set was finished), and who shamelessly sold motors to whoever would listen.

Finally, I would like to boldly suggest that Crouch may have stopped one level too early in his 120/12/3 acknowledgments, as I note that the ultimate culture maker, Jesus, was an inseparable three in one. To this end, I would like to recognize that I am not alone in this work. I bring forth my deepest thanks and appreciation for my loving, joyous, and patient wife, Lily, who is one with me and sustained me throughout this time, proof-read so much of my work, and helped me explain what a traveling wave ultrasonic motor is to a normal person. Her commitment and dedication to living life with me have made this process a great joy. Finally, my praise and thanks can never be sufficient for the great grace and power that I have experienced every day from the love of God through the person of Jesus, who continually leads me out of my darkness and into his glorious light, freeing me to experience eternally good life forever in his presence.

Soli Deo Gloria.

Table of Contents

List of Tables

List of Figures

1 Introduction

Microelectromechanical systems (MEMS), which grew out of the microelectronics industry in the 1970s, have produced a number of commercial products. MEMS devices can often be separated into two classes: sensors, and actuators. Sensors, such as accelerometers and gyroscopes, are used to measure various physical phenomena and transform this into electrical signals. Actuators transform electrical energy into mechanical motion. At the macro-scale, rotary motors are a common form of actuator. Electromagnetic motors dominate the macro-scale motor landscape, however traveling wave ultrasonic motors (TWUM) represent an important class of actuators for quiet, high resolution operation, widely used in applications including camera autofocus lenses, robotics, medical actuators, and various aerospace systems. TWUM are an attractive actuator technology because they are compact, efficient, reversible, and can provide low-speed high-torque output without gears. If the motors are vertically preloaded, a zero-power holding torque and large output torque can also be achieved [1].

For many small-scale systems, compact rotary actuators are highly attractive, especially those that produce high torque at low speeds and do not require gears. Electromagnetic motors, which are effective at the macro-scale, become less practical and attractive at the millimeter-scale due to unfavorable scaling of energy density and the complex motor components are difficult to fabricate. Electrostatic motors require relatively high voltages and produce limited torque [2]. Electrostatic and electromagnetic motors at this scale both operate at high speeds (on the order of 10^5 RPM). Transitioning electrostatic and electromagnetic motor technologies to the millimeter-scale would require gearing for many applications in order to transform the motor power to lower, more usable speeds on the order of 100 - 1000 RPM. This requirement for gearing adds a complexity to systems that cannot be easily overcome. Gears reduce the efficiency and compactness of the system in addition to adding complexity to the overall motor design. Thus for low speed applications (100 - 1000 RPM), TWUM fill a necessary place within the rotary motor landscape, especially at the millimeter-scale. For this reason, researchers and commercial entities have attempted miniaturizing TWUM. The literature indicates that miniaturization of TWUM using traditional manufacturing techniques is limited by manufacturing precision when fabricating motors on the order of 10mm in diameter [3]. Using recent developments in high quality piezoelectric film deposition and patterning, and MEMS fabrication techniques, it is proposed that TWUM can be made an order of magnitude smaller. Beyond enabling miniaturization, it is proposed that MEMS fabrication will allow for low-voltage and low-power motor operation, as well as batch production of motors, driving down cost and opening the door to possible high-volume application spaces such as consumer electronics, medical actuators, and small-scale military devices.

The objective of this work is to create a wafer-scale integrated millimeter-scale traveling wave ultrasonic stator combined with a rotor to create motor action, with power consumption lower than 10 mW, and amenable to batch production. At completion of this project, this dissertation contributes the following to the field:

- Demonstration of a millimeter-scale thin-film traveling wave ultrasonic motor (the smallest demonstrated TWUM).
- Design of a vertically compact millimeter-scale ultrasonic motor

- Fabrication of a wafer-scale integrated traveling wave ultrasonic motor
- Design lessons for resonant MEMS devices including, but not limited to traveling wave ultrasonic motors

Following a short overview of traveling wave ultrasonic motors in this section, the fabrication process for the motors is described in Section 2, with a focus on stator fabrication and the new processes to enable manufacture of miniaturized TWUM. Sections 3 through 5 describe the design and characterization of disc stators, ring stators, and motors respectively. Section 5 includes performance results of a prototype motor, with speeds exceeding 2000 RPM while consuming 4 mW of power at 10 V. Concluding remarks are contained in Section 6, including future works, and potential applications, such as fuzing, medical imaging, micro-robotics, and sensor calibration.

1.1 What is a Traveling Wave Ultrasonic Motor

A traveling wave ultrasonic motor (TWUM) is a motor which uses the surface motion caused by a traveling wave in a stationary vibrating component (the stator) to propel a movable component (the rotor). The traveling wave is generated in the stator by exciting two standing waves that are separated in space and phase. These standing waves are created by exciting resonance modes. An example of a standing wave in a disc is shown in Figure 1.1. The red sections, or anti-nodes, move vertically while the blue sections, or nodes, are stationary. The nodal points are collected in nodal diameters and nodal circles, both pictured in Figure 1.1.

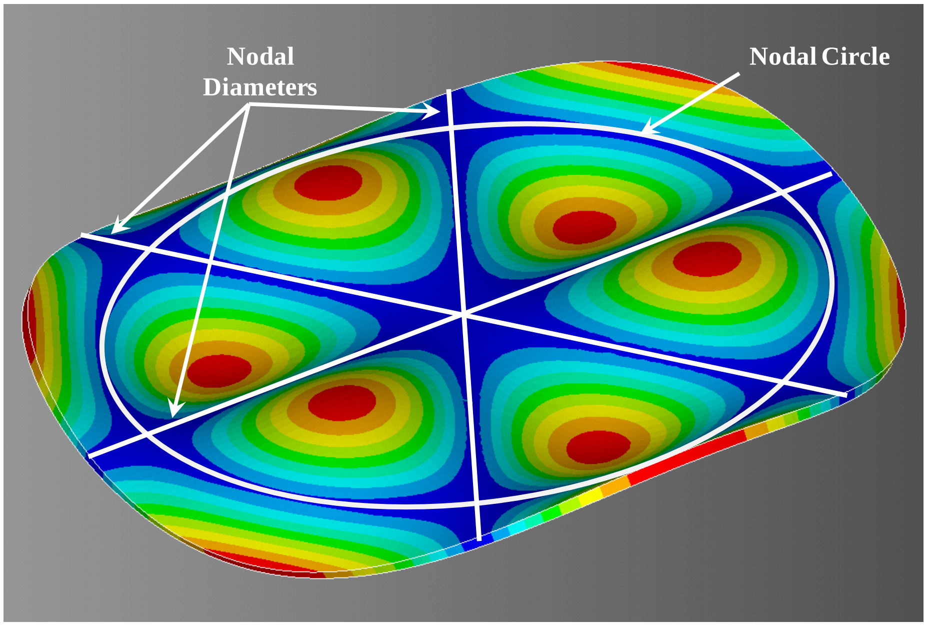

Figure 1.1. Simulated standing wave achieved through modal finite element analysis of resonance excitation using ANSYS. The red sections move vertically and are called anti-nodes. The blue sections are stationary and are called nodes, collected as either nodal diameters or nodal circles. This mode is called the B_{13} mode.

In discrete systems, such as simple mass-spring systems, there are a limited number of resonances related to the number of independent energy storage elements. For these discrete systems, resonances are often identified by their order in frequency from lowest to highest. In contrast, a continuous system has infinite resonances. For each resonance there is an associated frequency and mode shape. For simple structures like rings, discs, and rectangular plates, the mode shapes are expressed in predictable patterns. Although these general patterns are consistent from disc to disc, the order of the resonance frequencies can be altered by geometric and material properties. For this reason, resonance modes in these simple continuous systems are often categorized by their mode shape. These mode shapes are classified by the characteristics of their nodal regions, colored blue in Figure 1.1. These nodal regions experience no motion and are expressed symmetrically in these discs and rings along principal coordinates. In rings and discs, these axes are radial and circumferential (*r* and *θ*). The mode shape shown in Figure 1.1 is classified as a B_{13} mode because there is one nodal circle and three nodal diameters. To further illustrate this categorization principle, another mode shape is shown in Figure 1.2. This mode shape is classified as the B_{21} mode shape with two nodal circles and one nodal diameter.

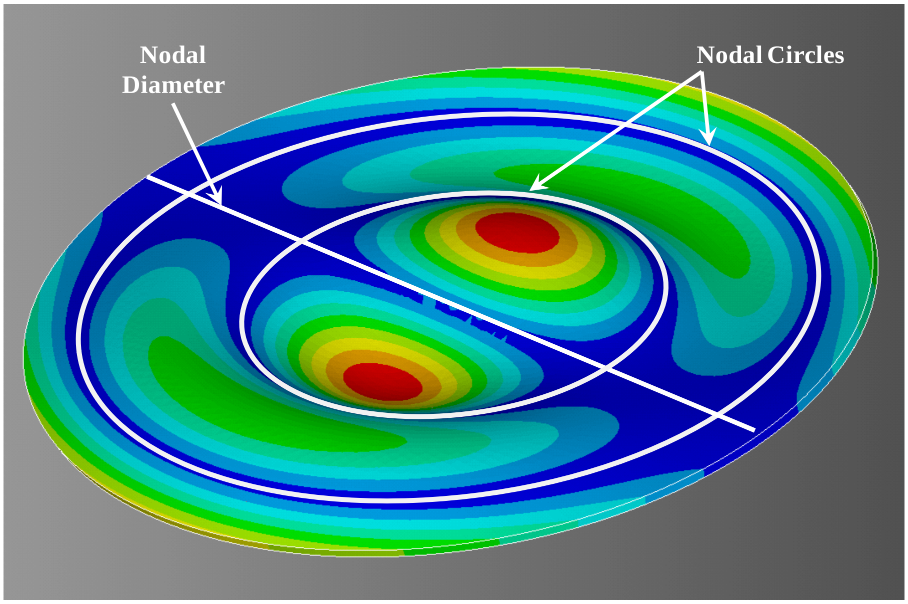

Figure 1.2. Illustration of the B_{21} mode of a disc stator with two nodal circles and one nodal diameter.

When a single resonance mode is excited, a point on the neutral axis of the stator moves vertically in a sinusoidal pattern. The relative magnitude of the vertical oscillation is determined by the spatial location as governed by the mode shape. For a point on the neutral axis, the vertical deflection over time, w, can be represented in polar coordinates by Equation 1.1.

$$w(r,\theta,t) = A_{mn}(r)\cos(n\theta)\cos(\omega_{mn}t) \tag{1.1}$$

In Equation 1.1, A_{mn} is the radial magnitude of the mode with m nodal circles and n nodal diameters, and ω_{mn} is the resonance frequency associated with the mode, while r is radius, θ is angle and t is time. Figure 1.3 shows $A_{mn}(r)$ for the B_{21} resonance mode shown in Figure 1.2.

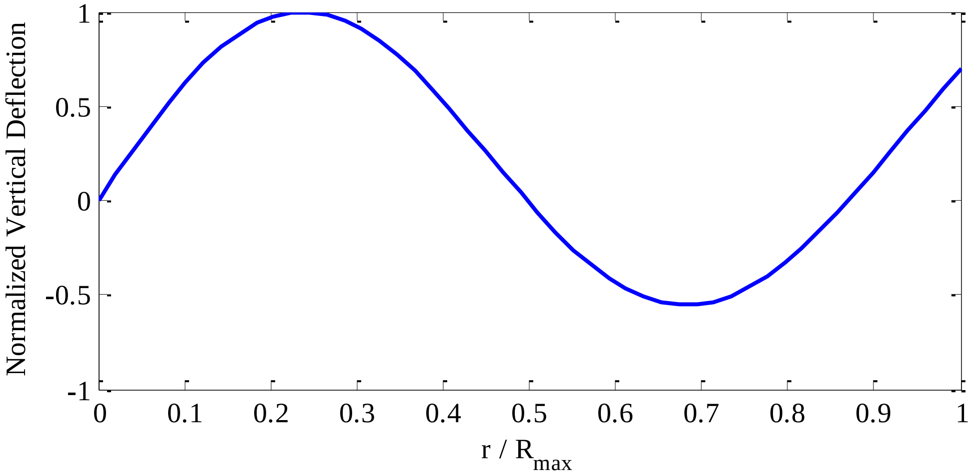

Figure 1.3. The radial magnitude, $A_{21}(r)$, of the B_{21} mode in Figure 1.2 is plotted here, showing the location of the peak deflection.

When this mode shape is combined with an orthogonal resonance mode, with a phase offset of 90°, the vertical deflection as a function of time can be described through superposition by Equation 1.2.

$$w(r,\theta,t) = A_{mn}(r)\cos(n\theta)\cos(\omega_{mn}t) + A_{mn}(r)\sin(n\theta)\sin(\omega_{mn}t) \tag{1.2}$$

In Equation 1.2, the component, sin($n\theta$), represents the orthogonal mode, which looks identical to the original mode, simply shifted by one quarter of a wavelength in space, while sin($\omega_{mn}t$) represents the 90° phase offset. The spatial shift means that anti-nodes of one mode shape are located along nodal lines of the orthogonal mode and vice versa. Two orthogonal modes of a ring are shown in Figure 1.4 displaying this offset.

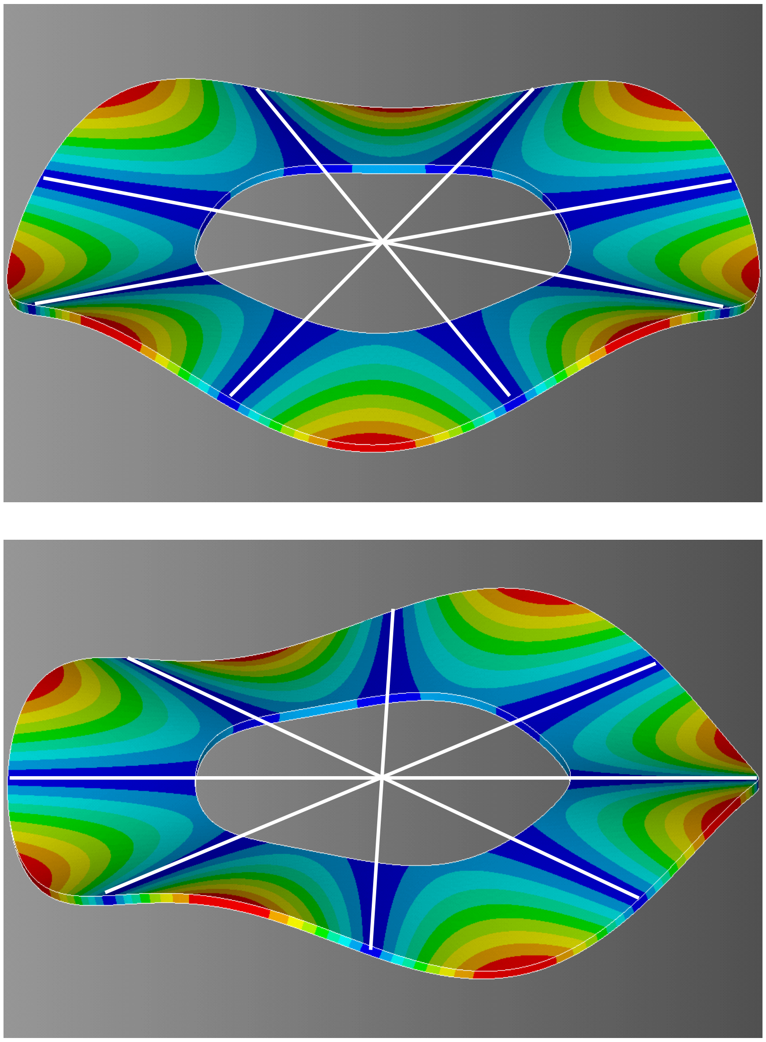

Figure 1.4. Two orthogonal modes showing the quarter-wavelength offset. If these modes are combined with two drive signals 90° out of phase, the resulting response will be a traveling wave of constant amplitude.

The sin(ωt) component in Equation 1.2 represents the 90° phase offset from cos(ωt). Through a trigonometric identity, Equation 1.2 can be simplified to the equation for a traveling wave in Equation 1.3.

$$w(r,\theta,t) = A_{mn}(r)\cos(n\theta - \omega_{mn}t) \tag{1.3}$$

This traveling wave can be illustrated by observing that w, at any angle θ, in a stationary reference frame will achieve the full range of amplitude $A_{mn}(r)$, because the quanitity ($n\theta - \omega_{mn}t$) reaches the full range of [0 to 2π]. This means that there is no nodal point within the disc. In a rotating reference frame, if $\theta = \omega_{mn}t/n + \theta_i$, the amplitude is constant, meaning that the wave of constant amplitude is traveling about the fixed disc. As the wave travels, the surface points of the stator move in elliptical orbits because the surface is offset from the neutral axis. The vertical component of this elliptical orbit arises from the out of plane motion of the wave, whereas the lateral component of the elliptical orbit comes from the varying angle of the neutral axis. Because the surface is offset from the neutral axis, the surface points move laterally when the neutral axis is angled. This elliptical orbit is shown in Figure 1.5.

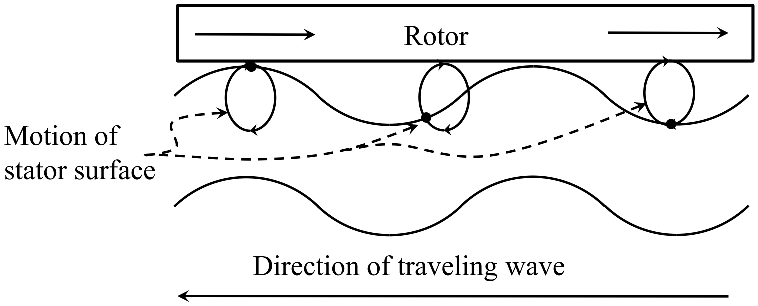

Figure 1.5. The elliptical orbit of the stator component is illustrated here, showing the effect of neutral axis tilt.

When the rotor comes into contact with the elliptically moving points on the stator surface, force is transmitted tangentially from the stator to the rotor through frictional contact. This frictional contact allows for large forces to be transmitted at low and usable speeds, however, this frictional contact makes accurately modeling TWUM extremely difficult. In the following two sections, these and other advantages and disadvantages of TWUM will be discussed.

1.1.1 Advantages

Advantages of TWUM described in the previous section include favorable energy density, high-torque low-speed operation, zero-power holding torque, and compactness. In this section, these advantages will be discussed and developed more, with comparison to various motor technologies, with a specific focus on small-scale mechanisms.

Energy density is a useful tool for comparing motor technologies, especially for small-scale mobile systems because of their limited payload capacity. Reducing the payload dedicated to the motor allows for more energy payload or more objective payload, allowing the devices and systems to operate longer, or provide more capabilities. Energy density scales favorably for ultrasonic motors compared to electromagnetic motors.

High-torque low-speed operation is an important advantage for this class of motor. Because most loads operate at low speeds, gear trains are often necessary to match the load speed to the motor speed at peak efficiency. These gears can be difficult to produce at small scales, and introduce size, complexity, loss due to friction, and failure mechanisms into the system. Ultrasonic motors create an inherent gear-down through the frictional coupling mechanism, allowing traveling wave that propagates through the stator at hundreds of kilohertz to create rotor motion on the order of tens of hertz.

Power and energy limitations are the most constraining characteristics in small-scale systems, and orders of magnitude improvement in energy storage capability in batteries is unlikely. For this reason, anything that can be accomplished with minimal- or zero-power consumption is very attractive. Ultrasonic motors exhibit a zero-power holding torque as a function of the normal load applied, meaning that with zero-power applied, the motor will resist rotation from external torque due to the frictional nature of the drive mechanism. This zero-power hold, along with excellent positional resolution, makes ultrasonic motors attractive for intermittent positioning applications.

Low power operation is another area where ultrasonic motors provide a specific advantage. Because piezoelectric actuation inherently requires low power, the motor can be much more efficient than other actuators at the millimeter scale. An example can be seen in small-scale MEMS armaments fuzing technology. The Naval Surface Warfare Center has developed a fuze that uses MEMS thermal actuators to move an explosive[4][5]. These actuators require high current (100 mA – 1 A draw, and thus high power for operation. This power requirement prevents fuzes with MEMS thermal actuators from being applied to small systems or for systems that cannot harvest energy from launch. With only a small amount of stored or harvested energy, TWUM could provide the same motion and force, enabling higher capabilities and smaller systems.

Finally, the high energy density, high-torque low-speed operation, and simple construction of the traveling wave ultrasonic motors can be fabricated in a compact form factor less than 1 millimeter thick. For example, the ultrasonic motor using cantilevered PZT beams in [6] is 2 mm in diameter and 300 µm thick, yet still provides 3.2 µNm of torque. The compact size is useful for small scale systems where space is placed at a premium.

1.1.2 Disadvantages

At the macro-scale, the two main challenges and limitations of TWUMs are durability and temperature sensitivity. Durability is a concern because the frictional nature of the drive mechanism could create wear in the stator and in the rotor. This wear could change performance over time, and eventually cause failure, especially if continuously operated for long durations. In recent years, macro-scale ultrasonic motors have demonstrated good resistance to wear, with a motor operating intermittently for 250 million revolutions with no performance degradation [7]. Temperature sensitivity has also been a well documented problem in ultrasonic motors[1]. Temperature can be changed by transient ambient conditions or by heat generation in the motor (either through friction or through hysteresis in the piezoelectric material). Because of the numerous sources of heat, temperature stability and sensitivity are important. This temperature variation can cause large problems because the macro-scale motors demonstrate non-linear softening resonance [8]. Temperature can change the resonance characteristics, which can have drastic implication for drive characteristics if the shift causes a catastrophic jump. To mitigate this effect, macro-scale ultrasonic motors are often operated away from the peak frequency to prevent this catastrophic jump. Resonance characteristics are also often monitored during operation and feedback control used to ensure optimal frequency input. At the mm-scale these thermal effect are expected to be mitigated somewhat by the increased surface area/volume ratio. Wear issues at the mm-scale are unknown, though thin film wear coatings are likely a solution to long term wear.

1.1.3 TWUM history

The traveling wave ultrasonic motor was originally invented by T. Sashida in 1982 while attempting to create a compact high-force actuator to mimic the human hand [9]. This motor became quickly commercialized by Canon for auto-focus in single lens reflex (SLR) cameras [10][11], and is still used today due to its excellent resolution and compact form factor. The motors were also commercialized for automotive applications

[12] and interior architecture applications where silent operation was desired [9]. Miniaturization efforts were performed to use the TWUM as a watch drive, however competing technologies, specifically quartz, have since replaced it. These miniaturization efforts resulted in a motor 10mm in diameter [1] which was used for a vibrating alarm on a wrist watch. Further miniaturization was attempted by Flynn using microfabrication techniques, however despite promising initial results this effort proved unsuccessful [13]. Reported results suggest that a traveling wave was not actually generated. This is evident because only uni-directional motion was observed despite switching the phase offset [14].

1.2 Motivation

Many of the previously stated beneficial characteristics of TWUMs would be particularly useful in a miniaturized system. In systems at the millimeter scale, appreciable forces at low speeds are incredibly difficult to create because resonance frequencies increase with decreasing size, while forces decrease greatly with decreasing size. Actuation technologies such as electrostatics and piezoelectrics are ideally operated at high frequency and have very limited motion. Electrostatic actuators are also very limited in the amount of force that can be generated. Electrothermal actuators can provide larger motion at slower speed, but consume significant power. TWUM uniquely address the void in the millimeter-scale actuator space for high force, large stroke, low speed, and low power actuation. Favorable energy density scaling and zero-power holding torque would also be beneficial for such millimeter-scale actuators. Finally the planar, compact structure of the TWUM makes this actuator amenable to microfabrication.

1.2.1 Manufacturing limitation for TWUM

Although the structure of the traditional TWUM is simple, it takes precise patterning of the device to properly excite the traveling wave. If the manufacture of the device is not performed precisely, the stator will not have matching orthogonal modes, preventing traveling wave excitation according to Equation 1.3. Current manufacturing techniques are limited in this capability, and cannot reliably produce patterned piezoelectric devices below the 1 cm scale. Microfabrication offers a solution to this problem by providing micrometer resolution for patterning devices. This high resolution allows for accurate patterning of electrodes and support components so that the resonance characteristics of the orthogonal modes match.

1.2.2 Batch production

Microfabrication also presents a unique capability for large scale manufacturing. As production volumes increase, the cost of producing each device drops rapidly. A large number of motors could be manufactured simultaneously in batches of silicon wafers. A 150 mm diameter wafer has over 300 ultrasonic stators, despite relatively sparse packing. For this reason, creating a motor that is constructed within this wafer-scale process is extremely beneficial. Such benefits would require large market demands, such as consumer electronics [15], in order to justify such batch fabrication, however recent successes of accelerometers, RF filters, and ink-jet printer heads suggest that if the demand exists, the cost of such a component can be greatly decreased.

1.2.3 Possible application areas

Many potential fields for using small-scale motors have been proposed over the years, some of which appear to be distant, while some provide a potential for more immediate implementation. The following topic areas for potential application will be discussed in detail: small robots, small low-power actuators, medical devices, and military applications.

1.2.3.1 Small robots

Flynn's work on small-scale ultrasonic motors grew out of a desire to create small-scale gnat-like robots which could be used for reconnaissance and small scale repair [16][17]. This remains a distant concept despite gains in microelectronics over the past 20 years. The problem is especially complex and challenging because of the limited energy available on such a platform. The control problems associated with platform like this are also incredibly complex, with current state-of-the-art platforms orders of magnitude larger and requiring vast amounts of sensor input, often from high resolution mounted cameras [18]. More realistic may be the use of small motors in miniature ground-mobile platforms for mobility, where more energy and sensor payload can be carried. These motors could also be used within a robotic platform [19] to or manipulate directional components, such as cameras or directional sensors.

1.2.3.2 Small low-power actuators

Several recent DARPA programs have targeted developing rotating platforms for a variety of applications. The first program, Information Tether Micro Automated Rotary

Stages, was initiated to develop rotating platforms that could be electrically connected to the anchored substrate, yet be free to rotate continuously. These stages could be used for optical information transmission among a network of these devices. The second recent DARPA program in small-scale rotating platforms was a gyroscope calibration program called Primary and Secondary Calibration on Active Layer. The program was designed to address challenges associated with long-term bias and scale-factor drift of positioning, navigation, and timing components. The rotating platform was proposed for in-situ calibration of these inertial sensors. These programs highlight the growing interest in micromotor technology, especially as the MEMS field matures. These low-power actuators could also be used to provide new capability in small systems. For example, if a motor can be used to steer a micro-lidar receiver, it would allow the system size and cost to be significantly reduced by eliminating the need for a high power laser and substituting a diode, while also potentially eliminating magnification components and amplifiers.

1.2.3.3 Medical devices

Rotating stages could also be useful in a number of biomedical applications. Not only could it be used for manipulating small tools, such as forceps, but it could also be used as a rotary platform for intravenous ultrasonic imaging. Currently intravenous ultrasound exists in two forms – a phased array and a rotating transducer. The rotating transducer has many benefits over the phased array approach, however it has limited ability to enter deep into the body because a relatively thick torsion rod needs to support the torque transmitted from a motor outside of the body[20]. Furthermore, wobble arises due to the length of the torsion rod, reducing image quality. By moving the motor to the catheter tip, better imaging can be performed deeper into the body.

1.2.3.4 Military applications

Several uses for a small rotating platform have been identified with military application as well. Fuzing is a field that is very sensitive to concerns of size, weight, and power, and this ultrasonic motor provides a small, light, low-power alternative to current fuzing components. To move arming mechanisms, MEMS fuzes use high-power thermal actuation[5][4] or rely on inertial energy from the spin of the round[21]. In some, cases, this abundance of energy is not available, so a new fuzing actuation mechanism must be developed. The ultrasonic motor offers a unique capability of rotation, as opposed to many linear MEMS mechanisms. Rotation provides continuous motion for large displacements. Compared to a linear mechanism, a rotary device is inherently unable to arm due to shock and can be utilized to create a drop-safe fuze design. This TWUM can also be used to prevent common-mode failure in dual MEMS safe and arm devices. Since the motor is also reversible, it can also re-safe command-arm fuzes, a feature that is not currently possible in small-scale fuzes.

1.3 Current State of the Art

The following section contains a survey of the current state-of-the-art in the field of small-scale ultrasonic motors. Current research and commercial efforts in small-scale ultrasonic motors are discussed.

1.3.1 Research

Research into small-scale ultrasonic motors has been going on for over 20 years. Initial work by Flynn et al. was foundational in the field of miniature ultrasonic motors [14]. Flynn fabricated ultrasonic stator membranes that could cause rotations on the order of 100 revolutions per minute. These stators did not operate as intended, as reversing the phase offset between the two input electrodes had no impact on the direction of rotation. Furthermore, rotation was observed even when only one signal was applied. It has been speculated that the membrane did not truly support a traveling wave, and the rotation was merely due to an unexpected standing wave excited in the membrane [2]. Muralt et al. also had early contributions in the form of a thin film vibrating motor [22]. This motor was designed with elastic fins to create rotation. The vertical deflection of the PZT film is transformed into lateral motion by angled fins that created uni-directional rotation upon standing wave excitation. Morita et al. demonstrated a number of tube-based ultrasonic motors [23][24]. Uchino et al. followed this work by demonstrating a bulk-actuated steel tube ultrasonic motor [25], culminating in a stator 1.6 mm in diameter and 4mm long [26]. This motor used the degenerate modes of a hollow cylindrical shaft to create motion. The rotor was spring loaded through the center of the shaft, creating preload and centering. More recently, Kaajakari et al. demonstrated a polysilicon motor driven with a bulk PZT slab [27][28], and Piratla et al. extended this work, reporting a polysilicon motor with an integrated control mechanism [29]. Unlike traditional ultrasonic motors, the rotor in this motor is propelled by air flow, so the stator and rotor are not in contact during operation. This type of motor can produce high speed rotation, but is inherently limited in torque production [30]. Tang et al. have created a small-scale standing wave ultrasonic motor that is driven wirelessly by replacing the traditional piezoelectric material with magnetostrictive material which is then actuated wirelessly by magnetic field [31], with a refined design presented in [32].

1.3.2 Commercial

Companies have also demonstrated small-scale ultrasonic motors with applications from watches to smart phones. Seiko created a 10mm diameter ultrasonic motor for watch drive [1], while ultrasonic motors have also been used for vibrating alarms in watches [33]. PCBmotor has performed promising miniaturization work by assembling bulk components on a PCB and using the circuit board material as the elastic material [34]. Although this manufacturing technique is inherently limited in miniaturization due to the same resolution problems faced in traditional motors, it does provide a low cost avenue for incorporating a TWUM into a system. New Scale Technologies has demonstrated rotary ultrasonic motors in a variety of shapes on the order of 10-100mm in characteristic dimension, while also creating unique linear ultrasonic motors as well [35].

1.4 Dissertation outline

Following this introduction section, the microfabrication process for the motor is described in Section 2, with a focus on stator fabrication and the new processes to enable manufacture of miniaturized TWUM. Sections 3 and 4 describe the design, modeling and characterization of disc stators and ring stator respectively. Section 5 describes the design, modeling, and characterization of the miniaturized TWUM. This section includes performance results of a prototype motor, with speeds exceeding 2000 RPM while consuming 4 mW of power at 10 V. Concluding remarks are contained in Section 6, including future works and potential applications, such as fuzing, medical imaging, micro-robotics, and sensor calibration.

2 Fabrication

This section presents information on the fabrication procedure for miniature traveling wave ultrasonic motors using microfabrication techniques. The process for creating traveling wave ultrasonic motors leveraged previous work in chemical solution deposited lead zirconate titanate (PZT) microelectromechanical system (MEMS) switches and actuators at the U.S. Army Research Laboratory [36].

2.1 Existing PiezoMEMS Processes

Fabrication under this established PiezoMEMS process can be split into 5 steps: actuator deposition, actuator patterning, interconnect metal deposition, reactive ion etching and etch passivation, and deep reactive ion etching and release. Each of these steps will be discussed in further detail below.

2.1.1 Actuator Deposition

Many materials could be used as the active material in an ultrasonic motor, however PZT offers a unique benefit in its large piezoelectric coefficients and coupling coefficients, while also being a well-studied, reliable material. Materials such as aluminum nitride would not be nearly as successful due to the smaller piezoelectric coefficient, which would limit out of plane deflection. With thin-film PZT chosen due to its excellent properties well suited for actuation, the deposition method must be chosen and justified. The most common deposition techniques for thin-film PZT include sputtering, and chemical solution deposition.

Sputtered PZT with excellent properties has been demonstrated with some success by Fujifilm [37], but sputtered PZT has proven difficult to reliably produce, with deposition rates and characteristics greatly influenced by the changing chamber and target conditions and generally have dielectric breakdown strength 50% lower than PZT deposited by chemical solution depsotion (CSD). CSD, however, allows control of stoichiometry and produces dense thin films at a fast rate. The main drawbacks of chemical solution deposition include residual film stress, defects, and sensitivity to the annealing process. Residual stress and edge beading limits the thickness of PZT deposited by CSD techniques to between 1 and 2 µm. Defects are a common problem in manually deposited films, however recent attempts at automating the deposition process has reduced defect density considerably [38]. Finally, annealing conditions are extremely important in determining crystallographic orientation and have recently achieved <001> crystallographic texture in excess of 95% [39].

For chemical-solution deposited PZT films to demonstrate the highest piezoelectric properties, the composition should be near the morphotropic phase boundary (52% Zr, 48% Ti), and the crystals should be oriented in the <001> direction. Stoichiometry determines the composition, while the underlying layers and annealing conditions determine the crystallographic orientation. Starting with a (100) silicon substrate, a thermal SiO_2 layer is grown with a thickness of 3000 Å. To properly control the texture in the PZT, the first layer of the metal-PZT-metal actuator stack is approximately 300 Å of titanium sputtered onto the insulating thermal silicon dioxide. This titanium is then fully oxidized into a rutile structure to create a template for the next layer, platinum. A 1000 Å thick layer of platinum is then sputtered on the titanium dioxide at 500 °C, which functions as a growth template for the platinum. This method has been shown to create highly <111> oriented platinum, which in turn is a good template for lead titanate seed layer [39][40]. This dense platinum film also prevents lead diffusion through the bottom electrode. Atop the Pt, a 17 nm thick layer of lead titanate (30% Pb excess) is spin-deposited and crystallized. This lead titanate acts as a seed layer to promote <001> growth of oriented PZT, desired for its higher piezoelectric coefficient compared to <111> oriented PZT [41]. The PZT solution uses a 2-methoxyethanol solvent and is spin-deposited onto the wafer and pyrolized to remove the organic solvents. Every two layers, the wafer is annealed at 700°C. When the desired thickness is achieved, the top platinum (1000 Å) is sputter deposited on top of the PZT at 500 °C. This process is described in greater detail in [39].

2.1.2 Actuator patterning

With the actuator stack deposition complete, the films must be patterned to define the active device areas. Micrometer alignment and vertical sidewalls of these patterns are critical to maintain the symmetry necessary to generate the traveling wave. The patterning is accomplished by argon ion-milling, in a 4wave 4W-PSIBE Ion Beam Etch System, which physically etches the material. Ion-milling is desirable because a secondary ion mass spectrometry (SIMS) end point detector allows for automatic end point detection when the leading or trailing edge of the platinum peak is detected. Furthermore, ion-milling of the PZT produces nearly vertical sidewalls, preventing the undercut that results from wet etching.

Three argon ion-mill steps are used to fully pattern the actuator stack shown in Figure 2.1 (b)-(d). In the first step, the top platinum is etched to pattern the top electrode of the actuator, Figure 2.1 (b). Because the top platinum is only 100 nm thick, the etch is run at a lower power, 160 W, in order to limit over-etch into the PZT. Endpoint is determined when the platinum trace falls below the threshold level of 1.4×10^4 counts per second. The second step is removing the remaining PZT and bottom platinum from all of the areas that do not require it, Figure 2.1 (c). In this step, a high power, 455 W, timed etch is used to etch through the majority of the thick PZT layer. A lower power is then used to finish the etch, with endpoint detection occurring when the platinum signal (from the bottom electrode) peaks and then drops 70% of the running average peak response. For the final step, a small portion of the PZT is removed, allowing access to the bottom platinum electrode, Figure 2.1 (d). To accomplish this, another high power etch is used to remove the majority of the PZT and a lower power etch is used to finish the etch with endpoint determined when the platinum signal, from the bottom electrode, rises above the threshold level of 1.4×10^3 counts per second. This prevents the etch from progressing through the bottom platinum, however it leaves a thin layer of PZT in some areas of the wafer. To remove this thin layer of PZT, a very short wet etch (1:240:480 $HF:HCl:H_2O$ by volume) is used to remove any residual PZT. This step allows connection to the bottom platinum electrode, which extends below the PZT layers.

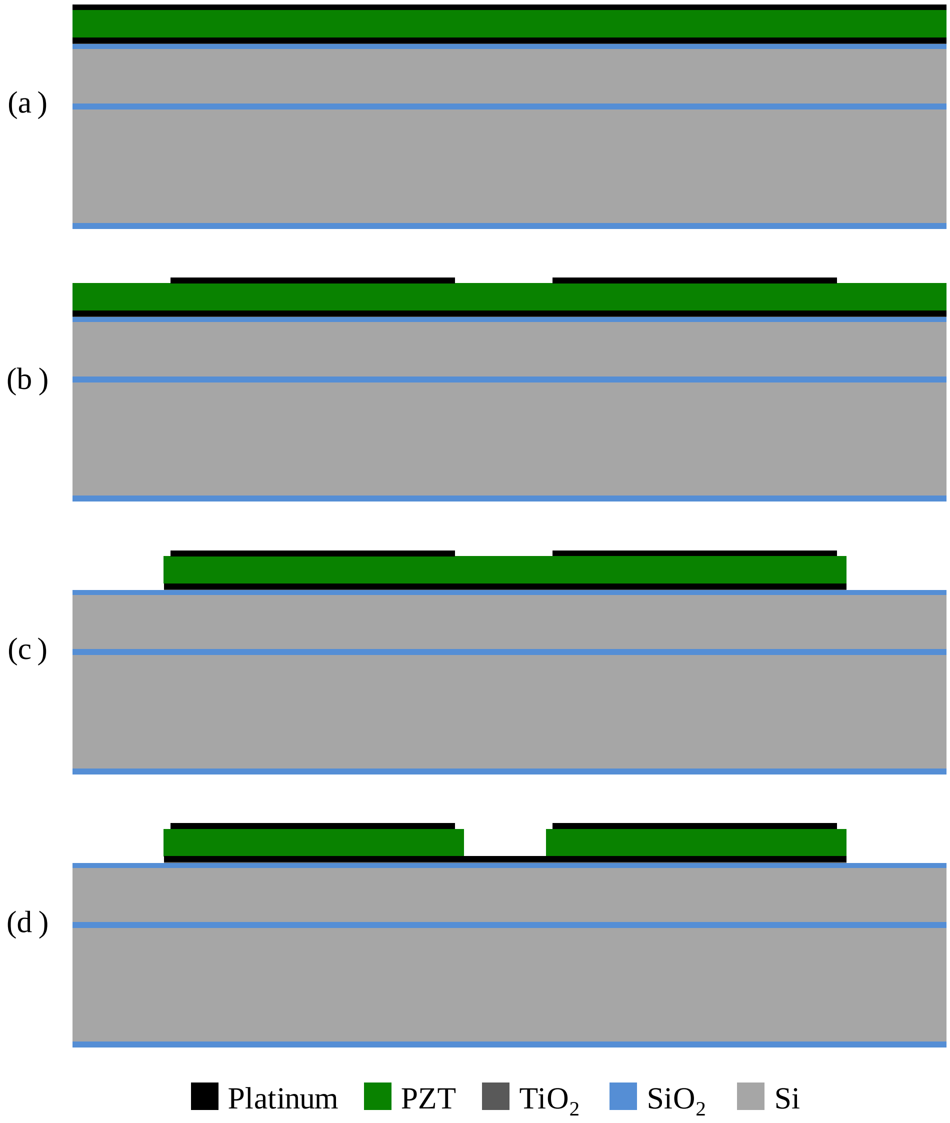

Figure 2.1. Actuator patterning steps. (a) Deposited unpatterned actuator stack (b) patterning top platinum layer via Ar ion milling, (c) patterning excess PZT and bottom platinum via Ar ion mill, (d) pattern via access to bottom platinum using Ar ion mill plus a short wet etch.

In each of these ion-milling steps, after the endpoint is detected, a short over-etch is performed followed by a 50s etch at 50 degrees to clean up the sidewalls. After each etch is complete the wafers are exposed to an oxygen plasma to remove the photoresist.

During the ion milling step, some material can be re-deposited on the sidewall of the photoresist. This residual material is removed using ultrasonication in isopropyl alcohol after the oxygen plasma removal of photoresist. Finally, the wafer is annealed in an oxygen environment at 500°C for 60 seconds to drive out defects caused during actuator patterning.

2.1.3 Interconnect Metal Deposition

Once the active PZT areas have been defined, electrical connections and gold bond pads must be deposited as shown in Figure 2.2. To demarcate the areas where gold should be deposited, a 2 μm thick layer of AZ5214 photoresist is spun onto the wafer. AZ5214 is a positive tone photoresist, however, if baked and flood exposed after the patterned exposure, the exposure pattern is reversed – resulting in a negative tone masking layer that has a slightly re-entrant profile, which encourages the liftoff process [42]. Once the photoresist pattern is defined, a 20 nm thick layer of chrome and a 20 nm thick layer of platinum are evaporated using an electron beam evaporator. These layers act as an adhesion layer for the following 730 nm of gold, Figure 2.2 (b). After the evaporation is complete, the wafers are soaked in acetone to dissolve the photoresist liftoff mask. To decrease the liftoff time, dummy features are placed in the field to reduce the undercut length. After the liftoff process is complete, a short ultrasonication is performed to remove small particles. After ultrasonication and rinsing, the wafer is exposed to a low power (200 W) oxygen plasma for five minutes to remove any remaining organic contaminants on the wafer. The wafer is annealed in an oxygen environment at 500°C for two minutes, or until there is no pinching in the hysteresis loops, indicating that all hydrogen has been driven out of the film.

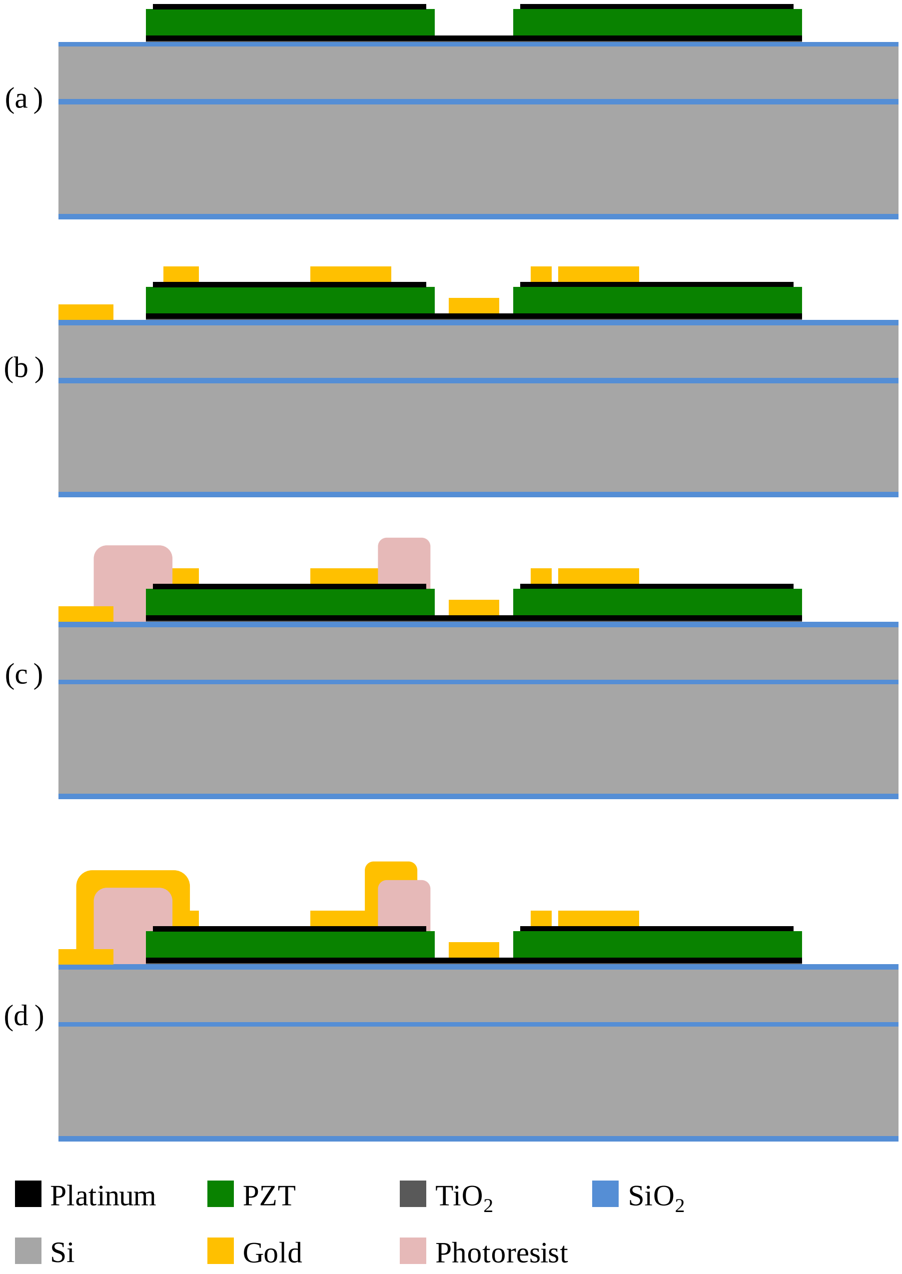

Figure 2.2. Interconnect metal deposition process. (a) Device cross-section after actuator patterning steps, (b) evaporation and liftoff of Cr/Pt/Au, (c) photoresist deposition and high temperature baking to enable electrical cross-overs, (d) gold evaporation and liftoff.

Another important function for the metal interconnects is bridging from the substrate to the top electrode. This is complicated by the fact that there needs to be an insulating layer between the electrical lead to the top electrode and the bottom electrode sidewall. To accomplish this, a sacrificial photoresist layer is deposited, patterned, and baked at 200 °C to create a rounded edge that will resist acetone during liftoff, Figure 2.2 (c). A thick liftoff mask is then deposited and patterned. Four consecutive layers of 500 nm of gold are deposited on the wafer to bridge between the top electrode surface and gold traces on the field oxide, Figure 2.2 (d). After the evaporation, acetone liftoff is performed followed by a short ultrasonication. This sacrificial resist/gold bridge process can also be used to create crossovers in the electrical leads.

2.1.4 Reactive Ion Etching and Etch Passivation

Once these steps are complete, the final device structure can be patterned and passivated as shown in Figure 2.3. To remove the silicon dioxide, which was exposed when the actuator stack was cleared from the field, a reactive ion etch (RIE) is performed, Figure 2.3 (b). This etch selectively removes the silicon dioxide in the exposed areas thereby opening access to the device layer silicon for etching, described in the next section.

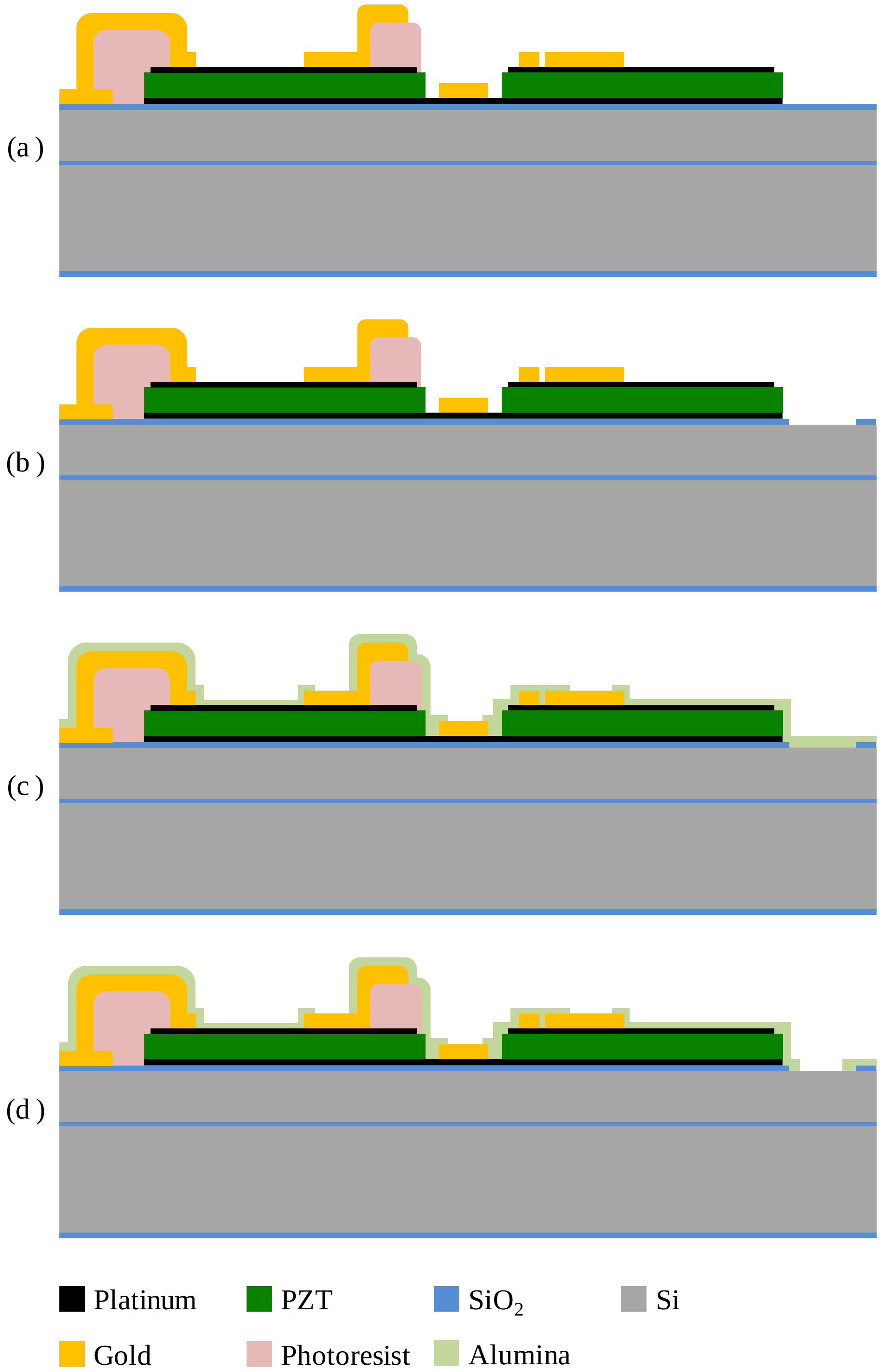

Figure 2.3. Reactive ion etching and passivation. (a) Device cross-section after interconnect metal deposition and patterning, (b) Reactive ion etch (RIE) of SiO_2 to expose silicon, (c) conformal alumina coating using atomic layer deposition, (d) alumina patterning via RIE exposing silicon surface.

As shown in Figure 2.3 (c), the next step is a conformal coating of alumina, Al_2O_3, accomplished using atomic layer deposition at 200 °C. A protective alumina layer is an important part of the fabrication process, serving multiple functions. The alumina protects the PZT from processing environments that could introduce hydrogen into the crystal lattice, changing the piezoelectric characteristics of the material and introducing more hysteretic loss. This hydrogen can be removed by performing high temperature anneals, however subsequent metal depositions limit the temperature (and thus the effectiveness) of these annealing steps. By encasing the PZT in the conformal alumina protective coating, the post-annealing properties are maintained, despite further processing that would normally be harmful. The alumina also serves an important purpose at the end of the process. Devices built on silicon-on-insulator (SOI) wafers use the thin device layer atop the insulating buried silicon dioxide as a structural layer. To release the device, the handle silicon under the device must be removed. This is commonly done using xenon difluoride (XeF_2), which is a gaseous isotropic silicon etchant. In order to properly release the device, however, the sidewall of the device layer must be protected. Conformal atomic layer deposited alumina has been used to protect the sidewall of a device Si layer from XeF_2 etch without pinholes [43]. A similar technique is used in the ultrasonic stator fabrication process except the alumina is used to protect the silicon dioxide on the wafer surface, while allowing removal of the buried silicon dioxide using a vapor hydrofluoric acid release.

The alumina is patterned using a reactive ion etch, Figure 2.3 (d). This pattern is offset by 5 μm from the edge of the silicon dioxide etch because the alumina must protect the silicon dioxide layer during the final release step. If the passivation layer fails and the release etch removes this top silicon dioxide layer, the actuator stack will partially delaminate from the silicon structure and will no longer be useful as a resonant stator.

2.1.5 Deep Reactive Ion Etching and Release

With the top films patterned and passivated, the stator structure is now formed and the device released, as shown in Figure 2.4. To define the stator structure, the device layer silicon must now be patterned. The silicon that is exposed after the alumina etch can be etched using a deep RIE (or DRIE), Figure 2.4 (b). This DRIE anisotropically removes the exposed silicon, stopping on the buried oxide layer. Once the front side of the device is patterned, defining the structure of the stator component, deep holes are etched using DRIE in the backside of the wafer, Figure 2.4 (c). These holes allow for the release of the stator structure using vapor hydrofluoric acid (HF) as described in Section 2.2.1. The remaining handle wafer silicon forms a honeycomb-like structure which is used to mechanically support the center anchor of the stator component. Finally, the buried silicon dioxide layer is removed by vapor HF, Figure 2.4 (d).

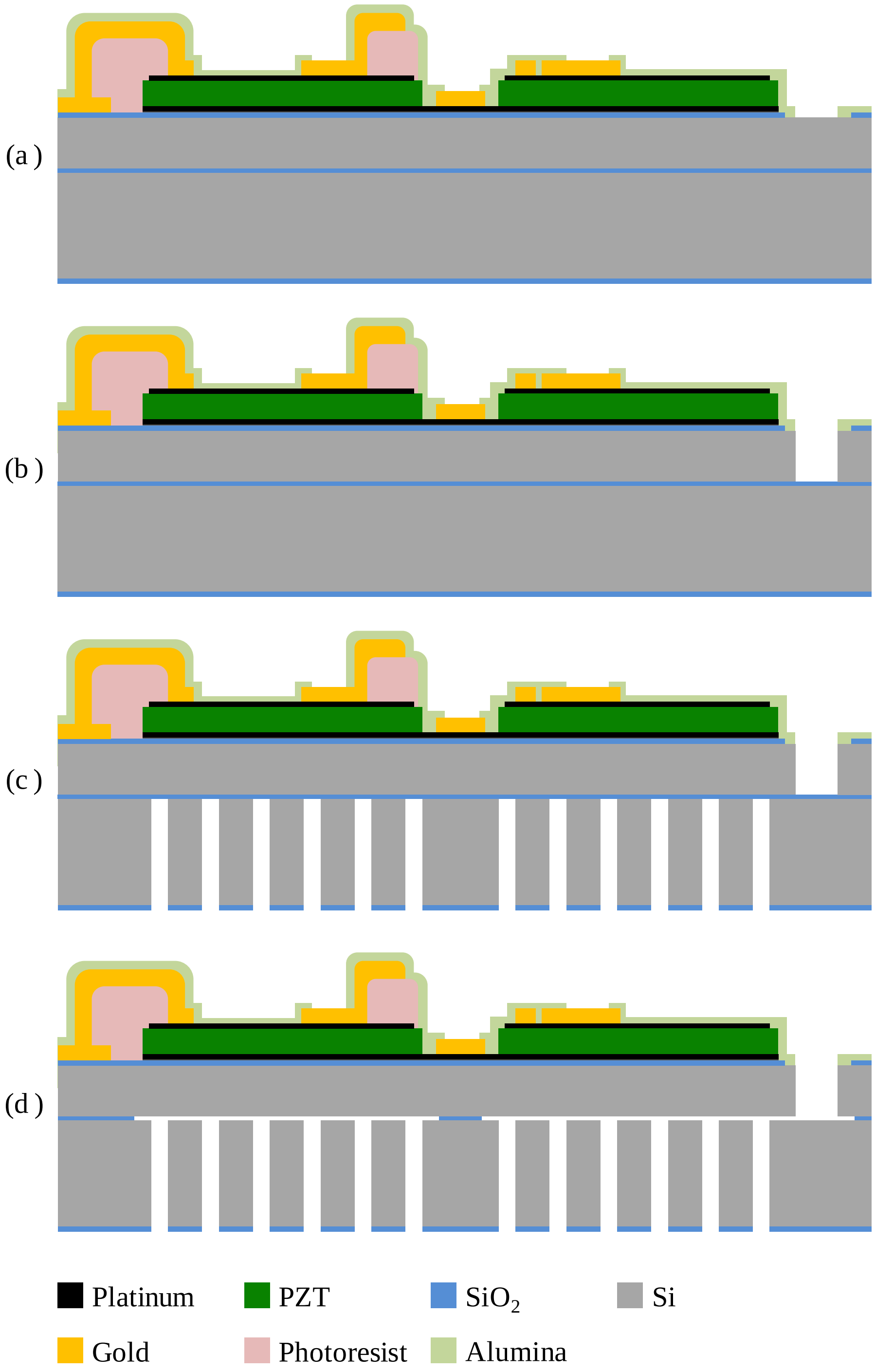

Figure 2.4. Deep reactive ion etch and release. (a) Device cross-section after RIE and passivation, (b) Deep reactive ion etch of device layer silicon defining the stator structure, (c) Deep reactive ion etching of handle wafer to expose buried SiO_2, (d) Vapor HF etch of SiO_2, releasing the device.

The entire fabrication process is summarized in Figure 2.5, displaying the five steps above: Actuator deposition, Actuator patterning, Interconnect metal deposition, RIE & passivation, and DRIE & release.

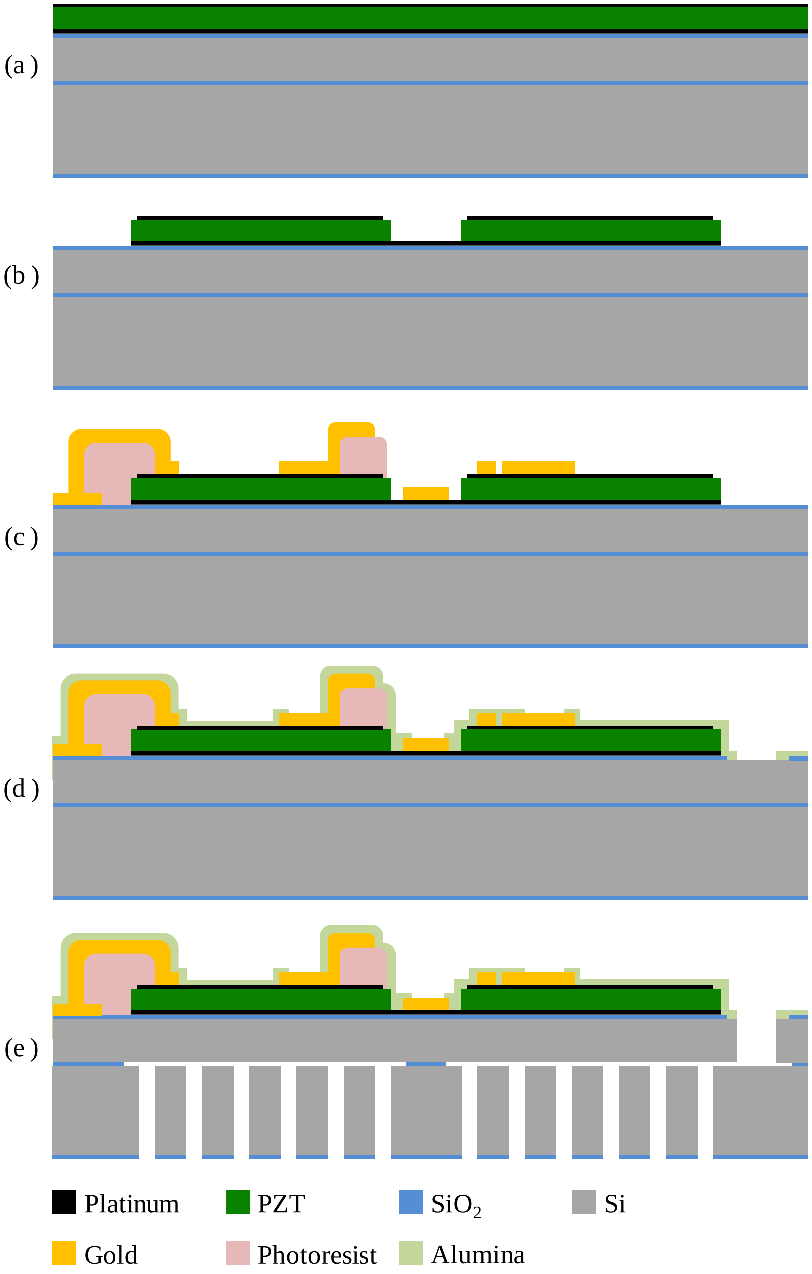

Figure 2.5. Stator Fabrication Process: (a) Actuator deposition, (b) Actuator patterning, (c) Interconnect metal deposition, (d) RIE & passivation, and (e) DRIE & release.

Once the stator fabrication is complete, preparation for electrical characterization and assembly into a motor is accomplished. First, the stator is placed in a dual inline package, a rotor is manually placed on the stator, and the device is wirebonded to the package. The completed motor is then ready for experimental evaluation.

2.2 Developed Processes

Traveling wave ultrasonic motors are significantly different in structure from the switches and actuators reported in [44] and [45]. In order to create the stator component of the ultrasonic motor, processes needed to be developed to address challenges in the fabrication of miniature traveling wave ultrasonic motors. These processes include: a timed backside vapor hydrofluoric (HF) release, a DRIE footing release, and deep trench refill.

2.2.1 Timed Backside Vapor HF Release

From the outset it was clear that traditional microfabrication release methods would be insufficient for traveling wave motors. The center of the disc stators needs to be supported mechanically by the handle wafer, so the handle wafer silicon could not just be removed. The stator component also needed to be thick, and preferably made out of a low mechanical-loss material such as silicon, so a silicon-on-insulator wafer was an obvious choice. Removing underlying material using an isotropic silicon etch, such as XeF_2, would be impossible with lateral undercut dimensions on the order of 1 mm as illustrated in Figure 2.6. An isotropic silicon etch would also take far too long, it would be difficult to protect the sidewall, and would be difficult or impossible to monitor undercut.

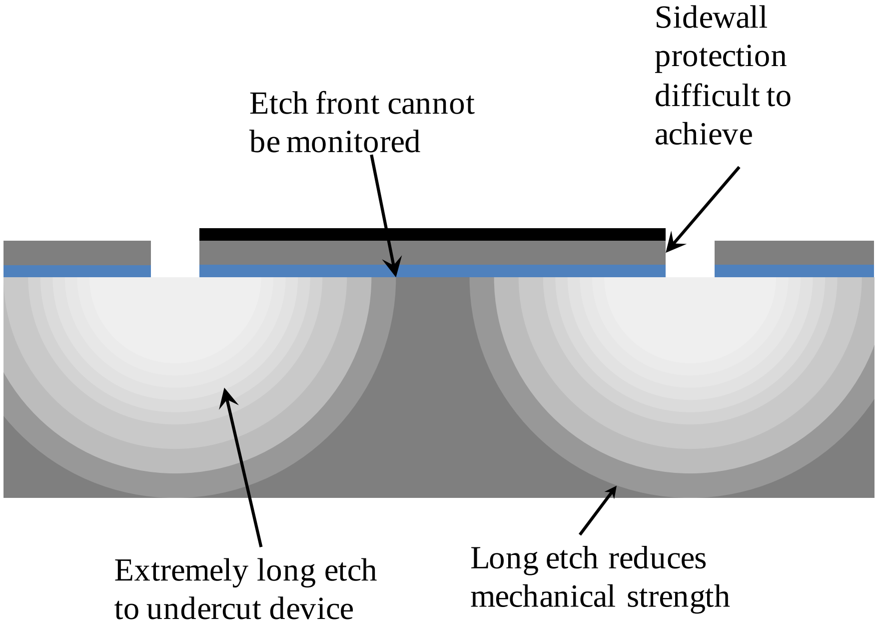

Figure 2.6. Schematic illustration of how a XeF_2 release cannot be used to release stators due to an excessively long etch time, sidewall defects, reduced substrate strength, and etch fronts that cannot be monitored.

Top-side Vapor HF release is often used to release SOI devices and was also considered. Accelerometers, which require release of large-area proof masses, are often fabricated using this technique. These large proof-masses, released using vapor HF, require etch holes that reduce the undercut length significantly as shown in Figure 2.7.

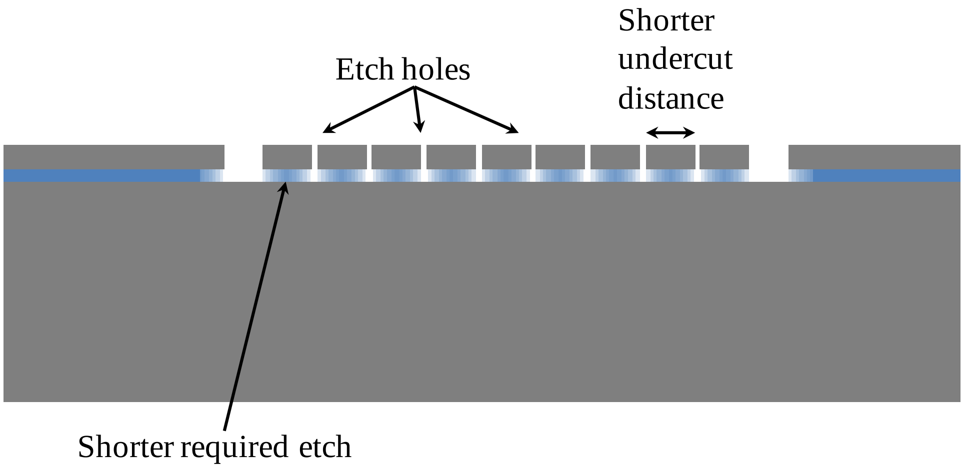

Figure 2.7. Schematic illustration of a vapor HF etch release with periodic etch holes used to release large area proof masses in MEMS accelerometers.

Although possible, etch holes in the ultrasonic motor stator were deemed undesirable because the hole would extend through the stator component. This stator structure depends greatly on the three-dimensional, high-order resonance modes of the structure, unlike accelerometers that use the released structure as a simple mass. Introducing holes throughout the stator component would distort these high-order resonance mode shapes. Furthermore, etch holes would need to extend through the PZT stack as well. Design and fabrication limitations would require an offset of 11 μm around each release hole, drastically reducing the active area, and possibly skewing the stator dynamics. Furthermore, the numerous etch holes would greatly increase the possibility that the protection barrier would fail and the underlying device layer oxide would be etched, delaminating the PZT stack from the silicon and rendering the device useless. These considerations are illustrated in Figure 2.8 for clarity.

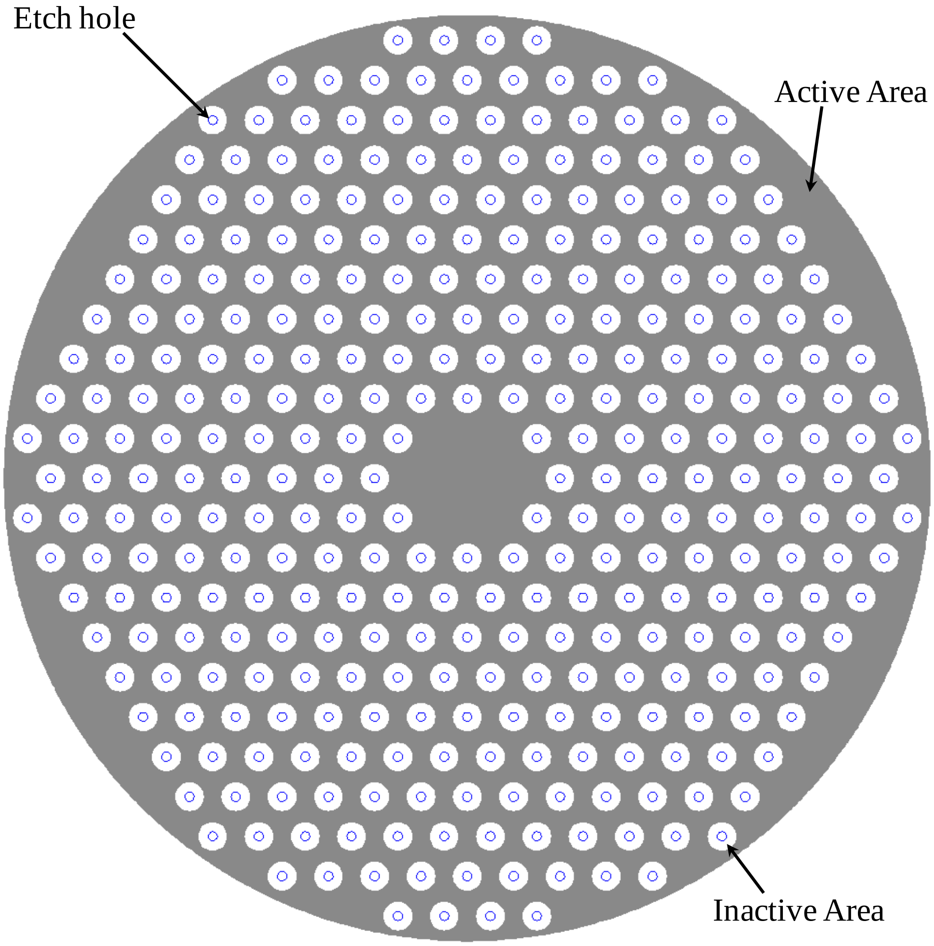

Figure 2.8. Top-side etch holes reduce active area significantly. In this figure, 5 µm-radius etch holes separated by 50 µm reduced active area, shown in gray, by 33%. The etch holes and inactive area also affect the resonance characteristics of the device.

Because these common microfabrication release methods are inadequate for these traveling wave ultrasonic motors, a new release method was used to undercut the device, while leaving it supported at the center. This method exploits the advantage of etch holes to reduce the release etch time. By etching the holes from the back of the wafer, however, we avoid the problems associated with traditional vapor HF release. These holes are etched so that the underlying structure of the handle wafer can still support the center of the stator, but allows the buried oxide to be etched. The through-holes etched from the backside of the wafer prevent monitoring the etch front using infrared microscopy, as done in traditional vapor-HF release. The PZT stator blocks the light and the intensity difference between the holes and the handle wafer support wash out changes due to the HF etch near the perimeter. A finished etch can be observed by testing the device using laser Doppler vibrometry, or by looking for a slight change in appearance which arises from the stator curving due to residual stress after it has been released from the handle wafer, as shown in Figure 2.9.

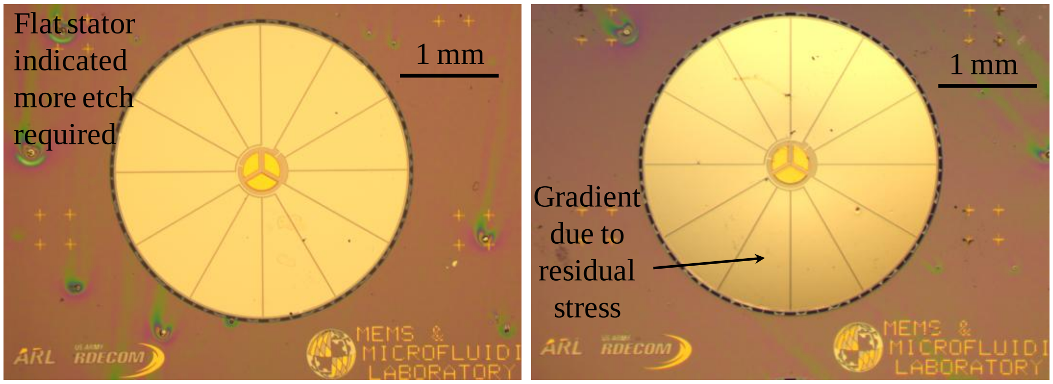

Unreleased

Released

Figure 2.9. Visible curvature related to residual stress deformation upon release suggests full release.

2.2.2 DRIE Footing Release

Although the timed vapor backside HF release was successful, problems with failure of the alumina protective layer led to a new method to release device, or at minimum, shorten the HF release. This release method exploits the fact that when a DRIE reaches a buried insulating layer, this insulator begins charging and the charge deflects the ions into the sidewall of the structure. These deflected ions create small outcrops in a process called footing. In most devices, footing is undesirable because it reduces the mechanical integrity of components and changes the component characteristics, illustrated in Figure 2.10.

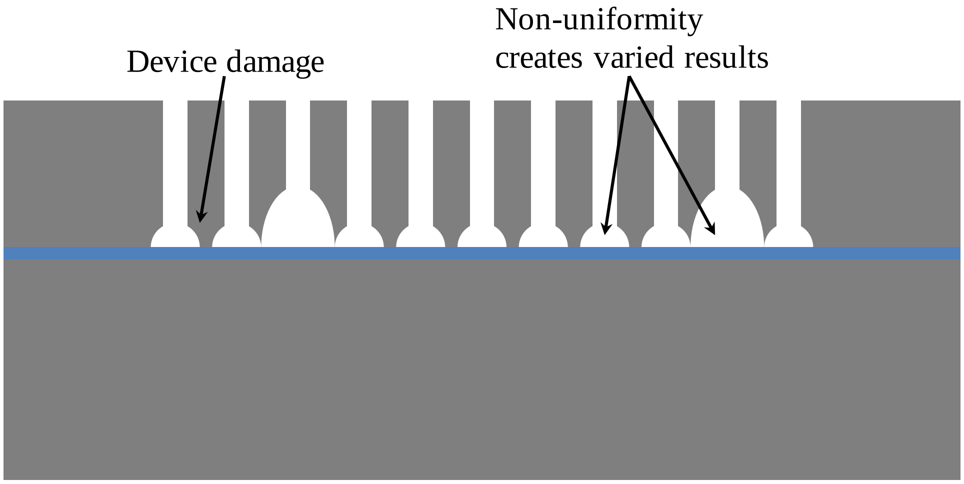

Figure 2.10. Schematic illustration of DRIE footing causing damage to the device silicon layer, altering device properties.

In the release of the ultrasonic motor stators, however, the mechanical characteristics of the handle wafer are unimportant (and also dominated by the bulk). For this reason, footing can be used to actually undercut the device. This is illustrated in Figure 2.11.

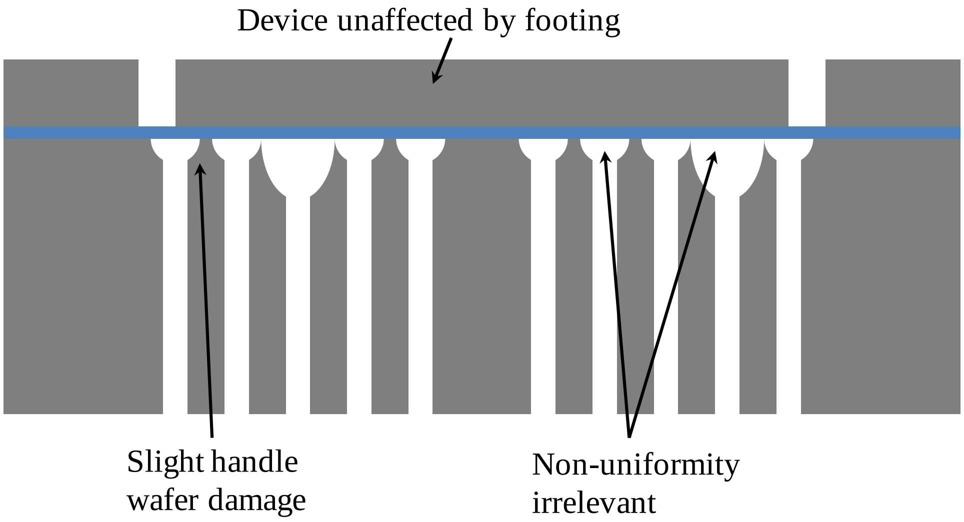

Figure 2.11. Schematic illustration of using a footing release, which is not affected by the normal drawbacks of DRIE footing.

If the device does not completely undercut due to footing, the shorter lateral undercut afforded by the partial etch allows for shorter vapor HF times. The shortened vapor HF etch helps mitigate the failures seen in the alumina protective layer and the resulting undercut of the silicon dioxide device layer.

The most significant challenge associated with this process include the fact that the DRIE etch rate varies by feature size and across a wafer. Because the etch rate varies and the handle wafer is very thick (400-650μm for 100-150mm diameter wafers), some parts will be undercut before the buried oxide is even reached under other parts. To mitigate the feature size problem, there can be only one feature size across the design. Because of the repeated pattern of the etch holes, this is easily achieved. The more difficult challenge is the cross-wafer etch non-uniformity. If the tool and recipe are properly tuned, the non-uniformity will be inconsequential given the severe over-etch that occurs during the footing process. Once the buried oxide has been reached across the wafer, the etch begins to cause footing, and thus release the silicon device layer and the buried oxide. The backside etch was the final step in the original process and devices released inside of the etch chamber would stick to the wafer chuck. In contrast, if the backside etch is performed first, the frontside etch will release the devices without damaging the wafer or the wafer chuck.

2.2.3 Deep Trench Refill

The final developed process is a photoresist refill of deep trenches. Refilling trenches is necessary to provide a smooth continuous surface for subsequent processing. In the case of the ultrasonic motors, a smooth surface would be required to create a surface for rotor patterning (for example, copper electroplated rotors discussed in Section 6.2.6). In the PiezoMEMS resonator process, photoresist was deposited, patterned, and reflowed to create a smooth surface for gold contacts. The ultrasonic stator process complicates this because the trenches are an order of magnitude deeper, preventing proper spin and patterning.

A study of the photoresist deposition, patterning, and reflowing in these deep trenches was performed. Trenches of varied width, from 16 µm to 32 µm, were etched into a test wafer 27 µm deep. A 12 µm thick layer of photoresist was spin-coated onto the wafer. Inset plugs of photoresist were then patterned and developed in the trenches at insets from 3 µm to 6 µm. After development, the wafer was heated to reflow the photoresist. Temperatures from 125 °C to 150 °C and times from 30 s to 300s were tested to determine optimal reflow conditions. A repeatable process was identified using straight trenches of varying widths and photoresist patterns of varying widths. When applied to devices, however, it was found that geometry effects dominate the reflow properties, creating excessively large bulges and pits that would prevent future processing as shown in Figure 2.12.

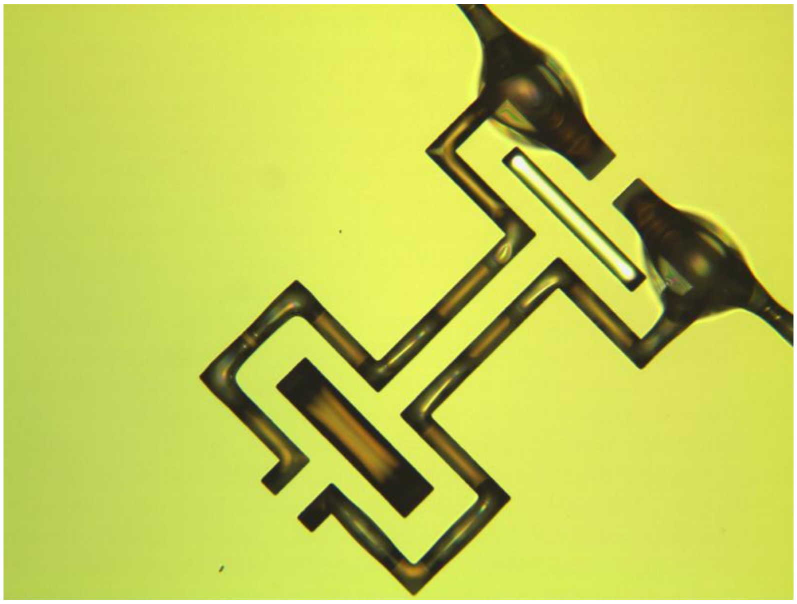

Figure 2.12. Large photoresist bulges during reflow prevent future processing.

In order to understand if the source of the bulges and pits was in the initial spin-deposition step, profilometry traces were taken to determine the surface shape. These traces showed a smooth surface with only ~1-2 μm of variation in height across the trenches. Photoresist patterning also showed consistent photoresist heights. During reflow, the resist formed large bulges and pits, likely due to surface tension and volume effects. The smooth surface after spinning and patterning suggested that a possible solution could be obtained by eliminating the photoresist reflow. In the reflow process, the target of the photoresist plug is coincident with the DRIE trenches. These trenches can therefore be exploited as a patterning mechanism.

To accomplish the modified trench filling, an underexposure and overdevelopment technique was used [46]. In this technique, a positive-tone photoresist is spun onto the wafer using a slow spin or a short spin to create a very thick layer of photoresist. This thick photoresist fills the trenches and creates a smooth surface, with only slight variation in surface profile. Once this smooth top surface is achieved, the wafer is then flood exposed without a mask. The exposure time should be lower than would be necessary to pattern a film of that thickness. The photoresist exposure process breaks down the photoresist exposed to ultra-violet (UV) light. As the resist at the surface is broken down, more UV is transmitted through, so the exposure occurs in a progressive manner, meaning that there is a photoresist exposure gradient from the top surface down, as illustrated in Figure 2.13.

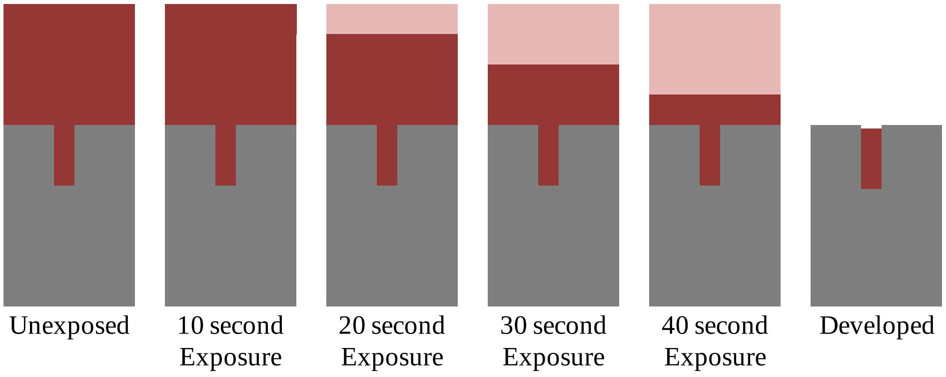

Figure 2.13. Progressive exposure in photoresist allows underdeveloped resist to be slowly etched away in dark erosion.

The exposed photoresist is removed readily in developer, while the underexposed photoresist is slowly removed, effectively in dark erosion. Because dark erosion progresses slowly, the surface of the wafer can be monitored optically to determine if the photoresist has been fully developed. For this specific application, AZ9245 photoresist was spun at 850 RPM for 40 seconds to create a 12 μm thick photoresist layer, with the photoresist filling the trenches. Various exposure times at 20 mW/cm^2 were tested and the step height was measured using stylus profilometry. These results are shown in Table 2-1.

Table 2-1. Results of underexposure overdevelop trench fill test

Exposure Time [s]	Step Height [μm]
50	15
47	12
43	10
40	8
35	6
30	5
25	3
20	Underdeveloped after 30 min.

Profilometry traces taken after a 25 second exposure and development showed an offset of 2-3 μm. This offset is 1 μm more than the variation as spun because the resist was overdeveloped to ensure the field is fully cleared of photoresist.

3 Disc Stator Design and Characterization

This chapter discusses the active component of the center-fixed disc traveling wave ultrasonic motor. Included within are two main sections: disc-stator design, and disc-stator characterization. Some of this information was presented in [47] and [48].

3.1 Disc Stator Design

3.1.1 Finite Element Analysis

Traveling wave motors operate through a set of complex electromechanical phenomena, requiring an effective model to guide the design process. In order to predict the response of the ultrasonic motor stators, ANSYS Finite Element Analysis (FEA) modal analysis was performed resulting in mode shapes and frequencies an example of which is shown in Figure 3.1.

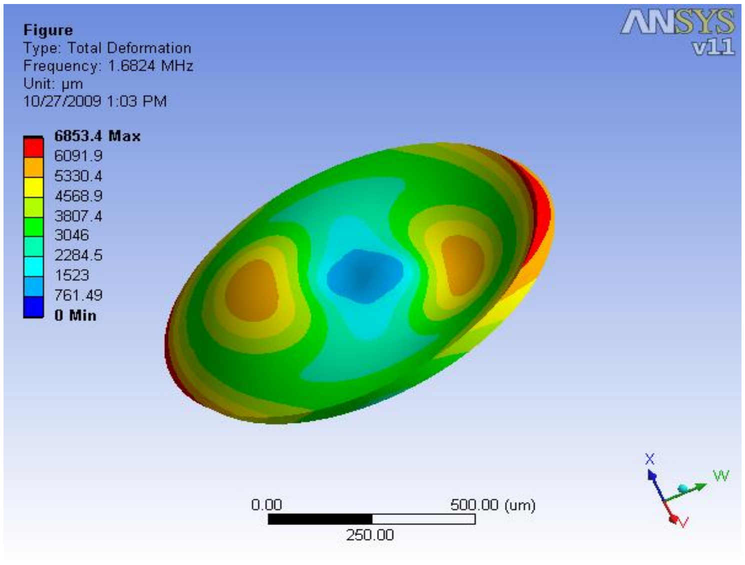

Figure 3.1. Sample FEA of a silicon disc displaying a high order mode shape.

An ANSYS script file was written to parameterize the model creation and aid in the design of the stators. The geometry for all cases shown contain a center anchor that is constrained in all degrees of freedom, while the disc is free in all other boundaries. Data from modal analysis on three silicon-only discs, sized 1 mm in diameter with a 200 µm diameter anchor, 2 mm in diameter with a 500 µm diameter anchor, and 3 mm in diameter with a 500 µm diameter anchor, is shown in Figure 3.2, Figure 3.3, and Figure 3.4 respectively. Modes extracted were the B_{02}-B_{09} modes and B_{11}-B_{15} modes, while all higher order modes were ignored because displacements would be too small to allow for proper motor operation. The first subscript refers to the number of nodal circles, while the second subscript refers to the number of nodal diameters. Amplitudes of motion in this analysis are normalized over the mass matrix so only mode shapes were extracted.

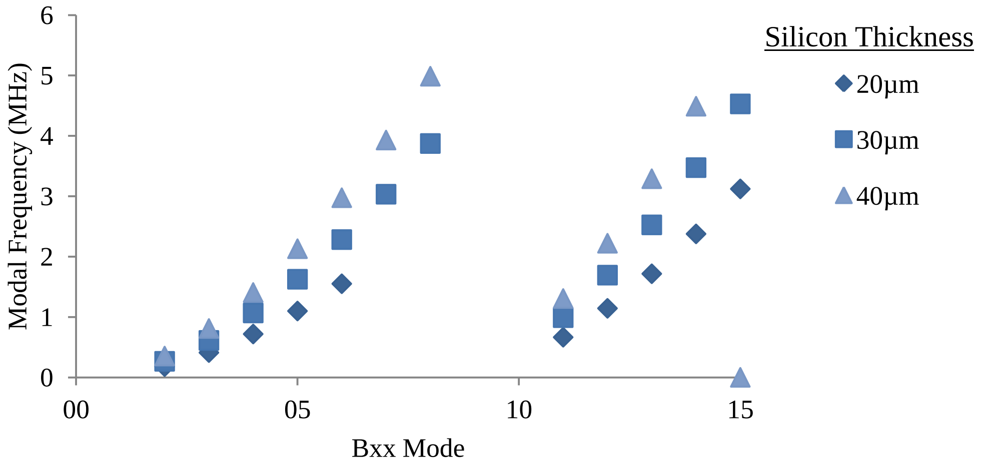

Figure 3.2. Modal analysis results from a 1 mm diameter Si stator disc with a 200 µm diameter anchor.

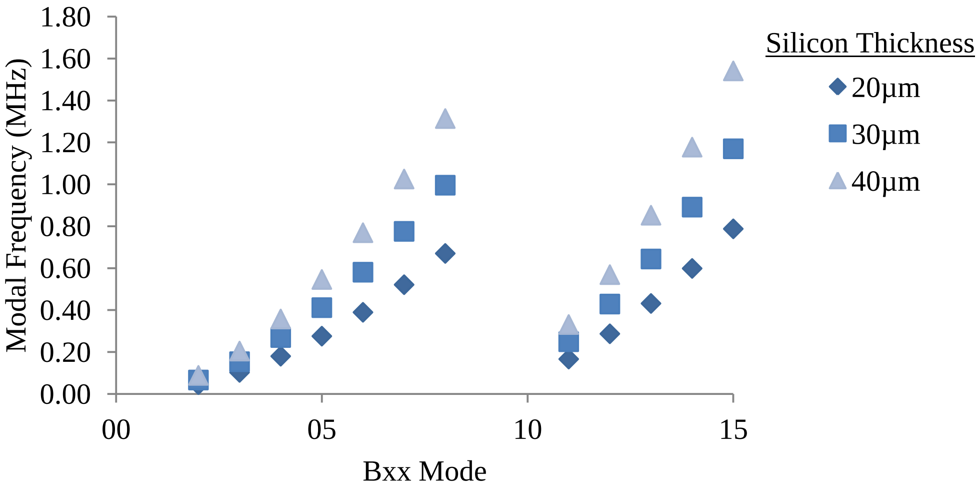

Figure 3.3. Modal analysis results from a 2 mm diameter Si stator disc with a 500 μm diameter anchor.

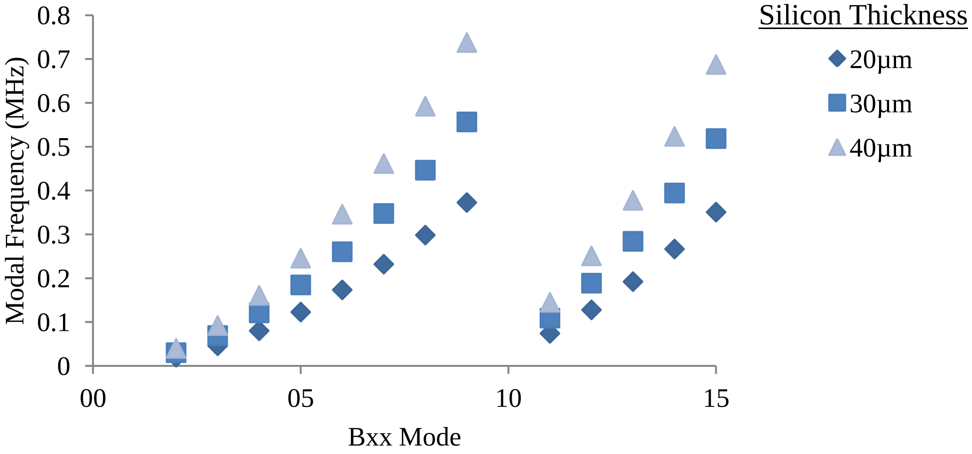

Figure 3.4. Modal analysis results from a 3 mm diameter Si stator disc with a 500 μm diameter anchor.

Based on the ANSYS analysis, 20 μm and 30 μm thick SOI device layers were chosen for initial stator fabrication to ensure successful device characterization. These thicknesses were chosen because the Polytec laser Doppler vibrometer (LDV) used for stator deflection characterization has an upper frequency limitation of 2MHz for single point measurement, and a 1 MHz limitation for 2-D scanning measurements. For example, the predicted response for the 1 mm diameter devices was greater than the limits on the available LDV for modes above the B_{04} and B_{11} modes. The estimated modes excluded contributions from the PZT, Pt, and silicon dioxide layers. These combined layers are thin, on the order of 1-3 µm, making proper meshing difficult. Since they only moderately affect the resonance frequency, they were neglected in this analysis. The relative scaling between modal frequency and stator diameter can be estimated by Equation 3.1.

$$\frac{f_b}{f_a} = \left(\frac{D_a}{D_b}\right)^2 \tag{3.1}$$

Here, f_a is a resonance frequency (associated with a specific mode) of a stator of diameter D_a and f_b is the resonance frequency of the same mode in a stator of diameter D_b with all other parameters remaining the same. This relationship can be derived from analytical resonance formulas for free discs [49] and was validated for the center-fixed disc under investigation using multiple FEA iterations. Comparing this relationship with all FEA predictions for devices using the same anchor size, the scaling frequency versus diameter is found to be within 2% of the model, as shown in Figure 3.5. This error is primarily from stiffening as the anchor becomes larger relative to the disc. Equation 3.1 can also be used to quickly predict the frequencies of sub mm-scale stators as well. For instance, the model predicts a 500µm diameter stator 20µm thick would operate at 7.2MHz.

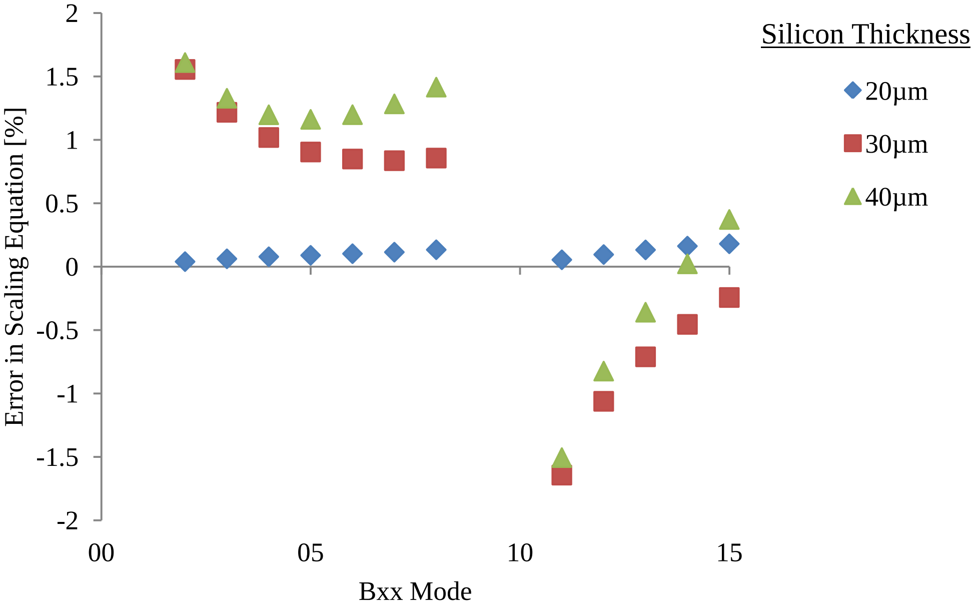

Figure 3.5. Error in using the simple scaling model due to stiffening of the disc structure from the anchored center post.

From the FEA simulations and fundamental TWUM operation, the primary modes of interest were the B_{03}, B_{04}, B_{13} and B_{14} modes consisting of 0 and 1 nodal circle and 3 and 4 nodal diameters, respectively. Figure 3.6 and Figure 3.7 show FEA simulations of the B_{04} and B_{13} mode shapes. These modes are desirable as they ensure rotor stability by maintaining at least three contact points of the stator to rotor, maximize vertical displacement compared to higher order modes, and minimize the required number of actuation regions. While various vibration modes are under consideration for future TWUM, the B_{13} mode, consisting of 1 nodal circle and 3 nodal diameters, were explored first. For this case the stator is patterned with 12 conductive regions grouped into four sets of 3 alternating electrodes.

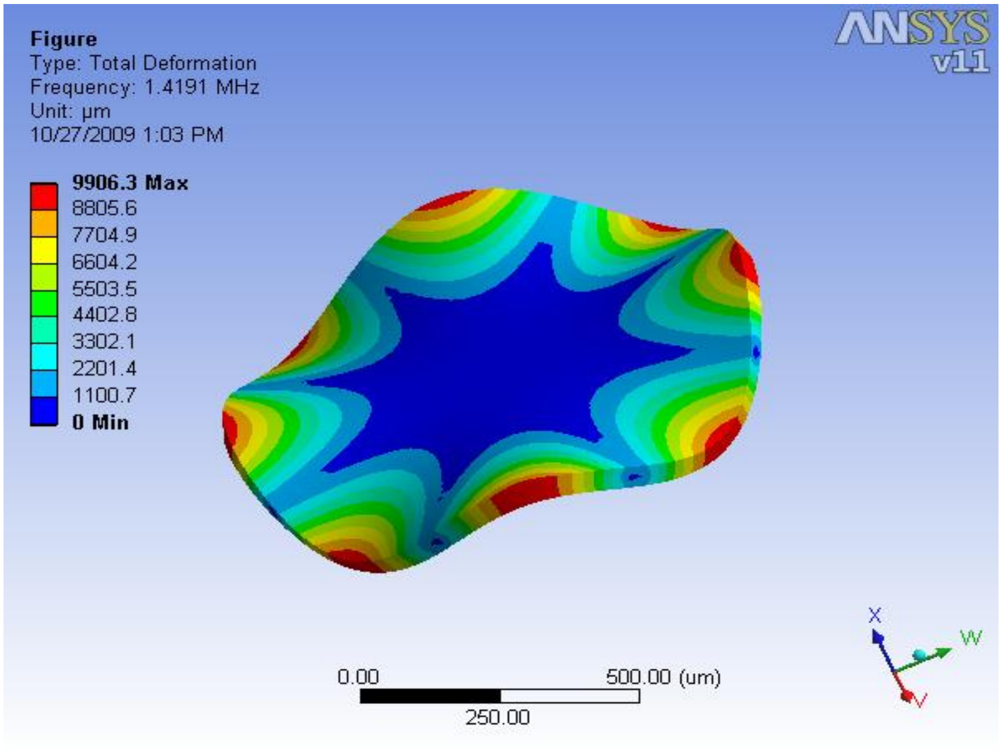

Figure 3.6. B_{04} mode simulated using ANSYS finite element analysis software.

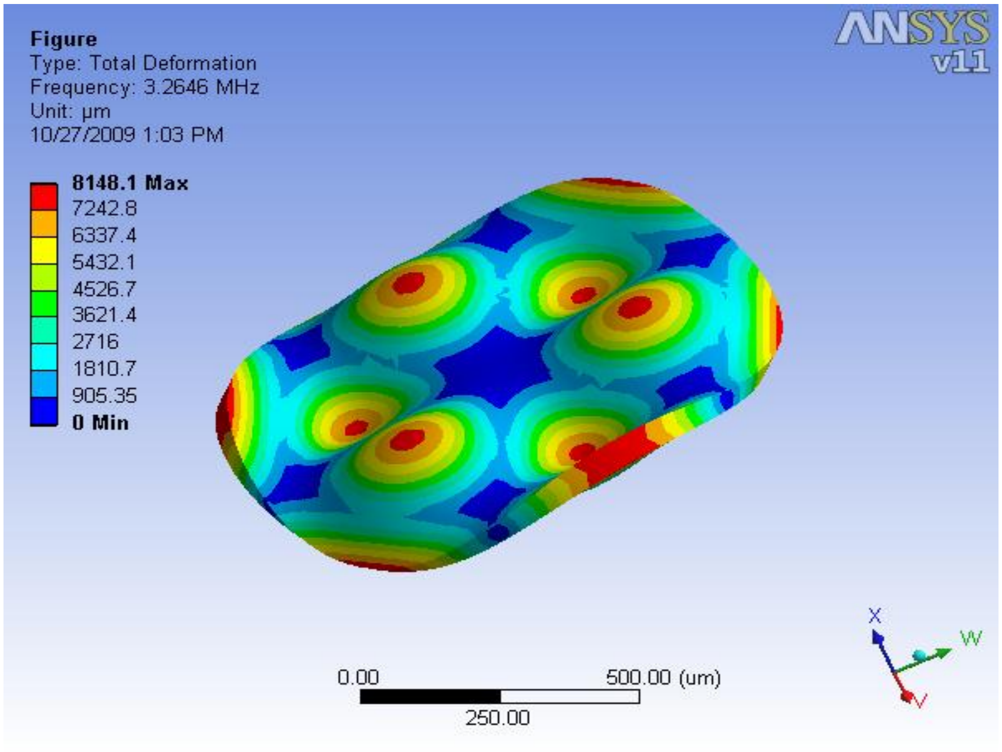

Figure 3.7. B_{13} mode simulated using ANSYS finite element analysis software.

The mesh used tetragonal element with element sizes of 6μm. Table 3-1 describes the parameters used for simulation. Silicon dioxide, platinum, and PZT layers were shown to have a very small effect on the modal solution. Furthermore, these thin layers relative to the Si device layer greatly complicated the meshing process as it is preferred to have multiple elements spanning the layer thickness. As a result, PZT, Pt, and SiO_2 were neglected in this analysis.

Table 3-1: Simulation parameters used in ANSYS modal analysis of discs

Quantity	Simulation Value
Silicon Young’s modulus	170 GPa [50]
Silicon density	2330 kg/m^3
Silicon Poisson’s ratio	0.064 [50]
disc thickness	30 μm
disc diameter	3 mm
anchor thickness	2 μm
anchor diameter	500 μm

3.1.2 Macro-scale motor template

To design the disc stator, macro-scale motors were used as a template. In these macro-scale motors, there are two potential configurations. In both of these configurations, there are four sets of electrodes: +sine, +cosine, -sine, and -cosine. The sine and cosine electrodes are offset in space by a quarter-wavelength, enabling the traveling wave generation as described in Section 1.1. The first configuration separates the sine components and cosine components [51]. This is illustrated in Figure 3.8.

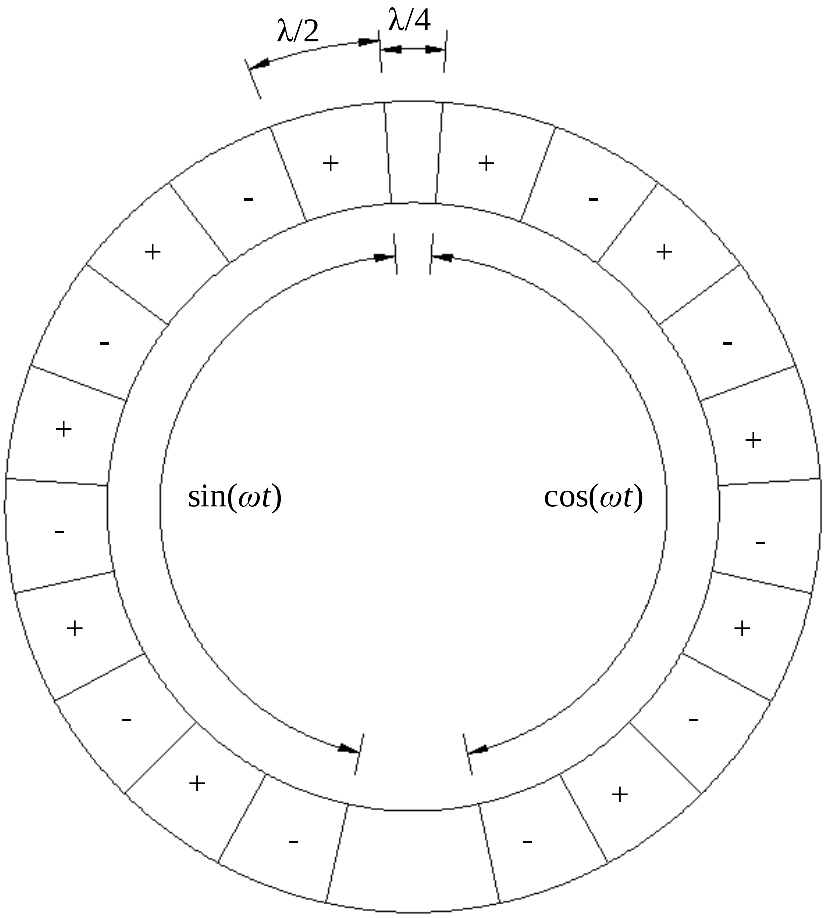

Figure 3.8. TWUM electrode configuration splitting the cosine and sine components as originally developed by Sashida.

This configuration is very common in macro-scale motors because it is very simple to manufacture and electrically connect. The piezoelectric ring is poled in alternating sections using a specialized device applying alternating electric fields to each of the designed segments. This allows the poling to be performed in one step. After these sections are poled, two continuous electrodes are used to drive the stator. One electrode carries a sine wave, and the other carries a cosine wave. The alternating polarization creates the positive and negative orientation of the sinusoids. There are small portions of the stator which are inactive in this configuration, however as the number of nodal lines increases, these sections become smaller.

Despite these benefits, this configuration could not be used for thin-film PZT TWUM because the optimal operating voltages are well above the coercive voltage. Operating thin film PZT using bipolar signals above the coercive voltage results in hysteretic loss and degrades the PZT. As a result, the polarization configuration which was used to create alternating sections in bulk ceramic motors cannot be used for thin-film devices. Because of these limitations, a different configuration must be used to create a traveling wave stator using thin film PZT [52]. This configuration is shown in Figure 3.9.

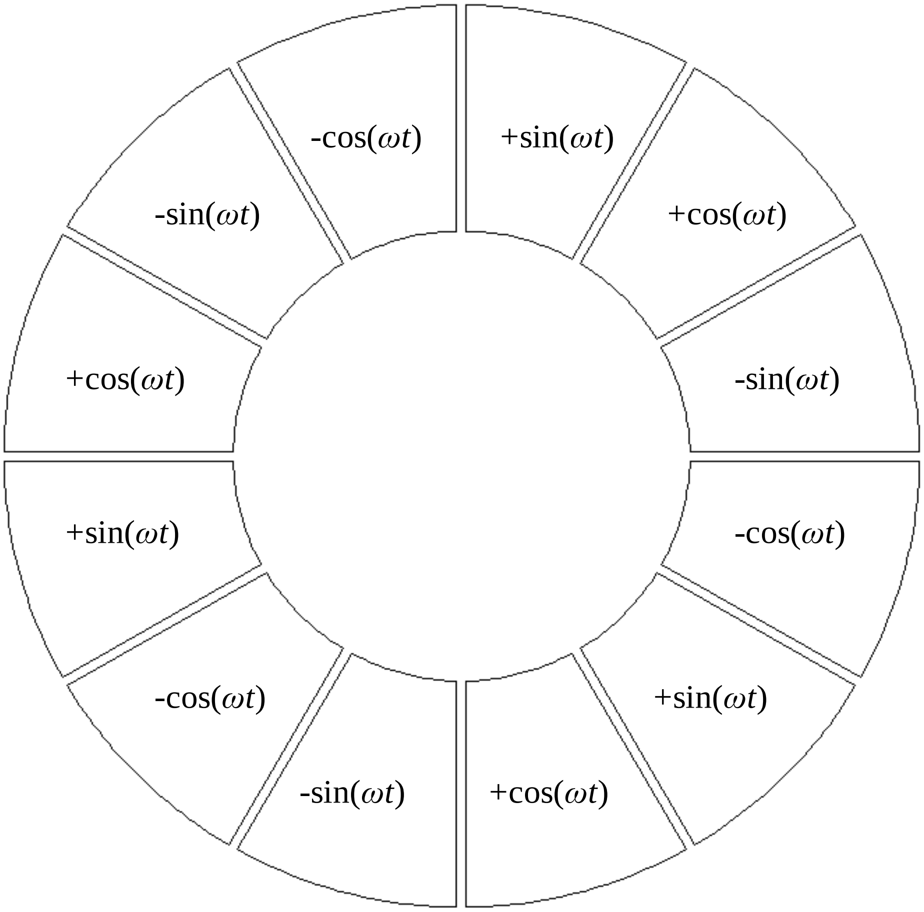

Figure 3.9. TWUM electrode configuration for thin film PZT devices using alternating cosine and sine electrodes.

In this configuration, the quarter-wavelength offset in space between sine and cosine is more apparent. The number of nodal diameters determines the number of sections. Each section is then split into four subsections: +sine, +cosine, -sine, and -cosine. Using unipolar operation, all of these signals carry a DC offset such that the voltages run from 0-V_p, where V_p is the peak actuation voltage.

A major drawback of this configuration is that the wiring is very complicated. Because four signals are interwoven, there is no simple way to connect each electrode to its associated partners (e.g. +sine with +sine, etc.). Connections can be run at the center for one set and at the perimeter for another set, but there is no path for the final two sets to be connected without crossing over a connection. Because of this, crossovers were included in the process to allow for the segments to connect with overlapping traces. A micrograph of these crossovers is shown in Figure 3.10.

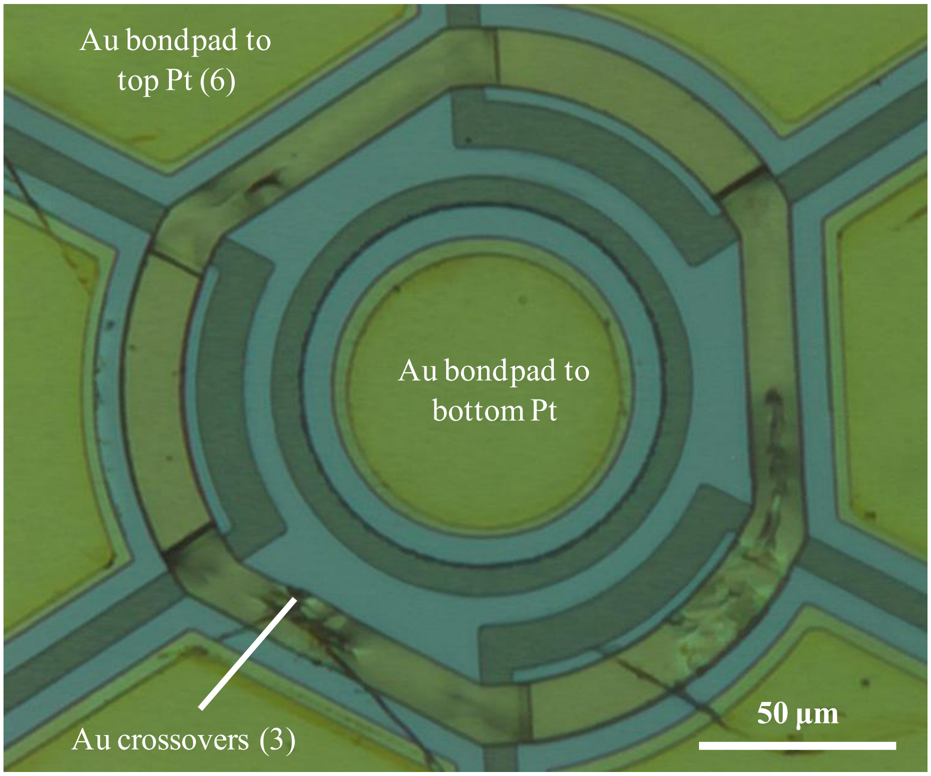

Figure 3.10. Optical micrograph illustrating the electrical crossovers included in a disc stator to allow for segments to be connected.

In this configuration, negative sine excites the same standing wave as positive sine, creating larger deflections from the two superimposed waves. The same is true of positive cosine and negative cosine. Because of this fact, a traveling wave can be excited in the stator using only two signals, rather than all four. One disadvantage of this approach is a reduction in the traveling wave amplitude. On the other hand, the complicated crossovers structures are no longer necessary as shown in Figure 3.11. This design contains inactive sections, shown in white in the figure. Since these sections do not contribute to the resonance excitation, the maximum potential excitation is reduced.

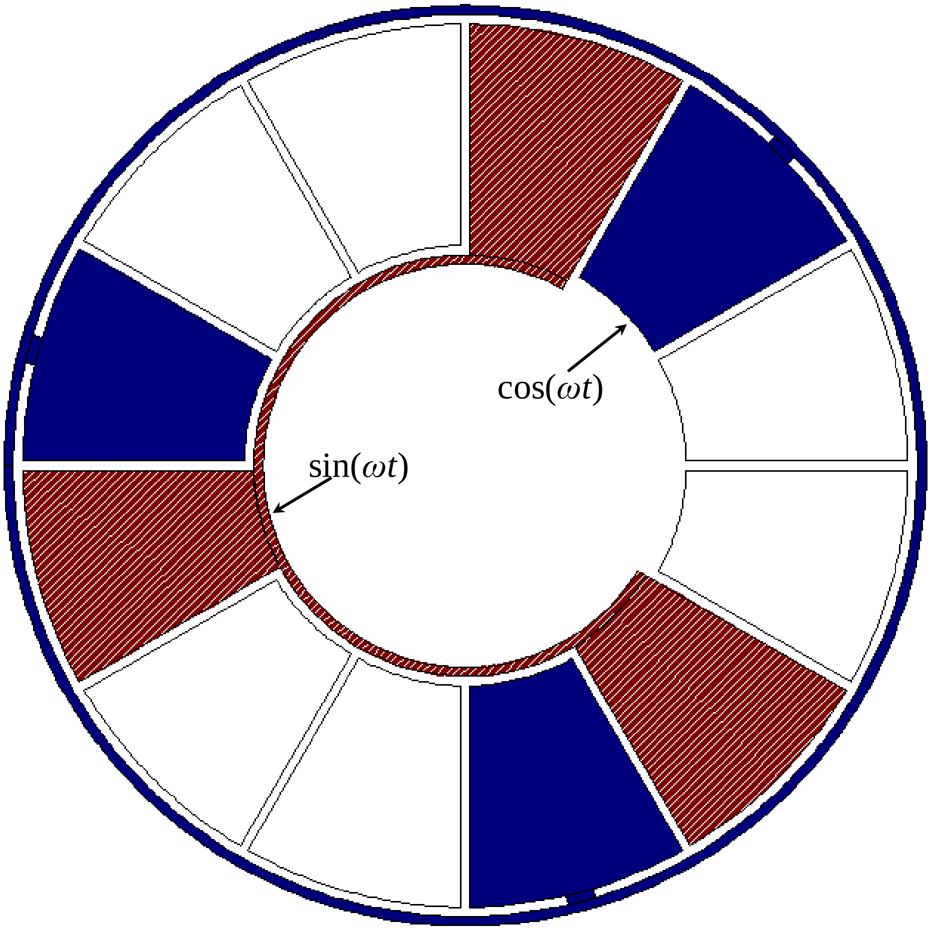

Figure 3.11. Design of the modified alternating electrode design, highlighting the simple connections without requiring crossover structures.

3.1.2.1 Modes examined

With the design guidelines outlined above, design choices remain regarding the number of nodal diameters and nodal circles. The modes examined using finite element analysis included modes with zero nodal circles and one nodal circle. Each mode in these families is then defined by the number of nodal diameters that exist in the mode shape. Low order modes are desirable because higher order modes occur at higher frequencies, and the high frequency nature of these modes limits the out of plane displacement. Furthermore, higher order modes result in lower active area because the area separating the larger number of electrodes increases as the mode order increases, as shown in Figure 3.12.

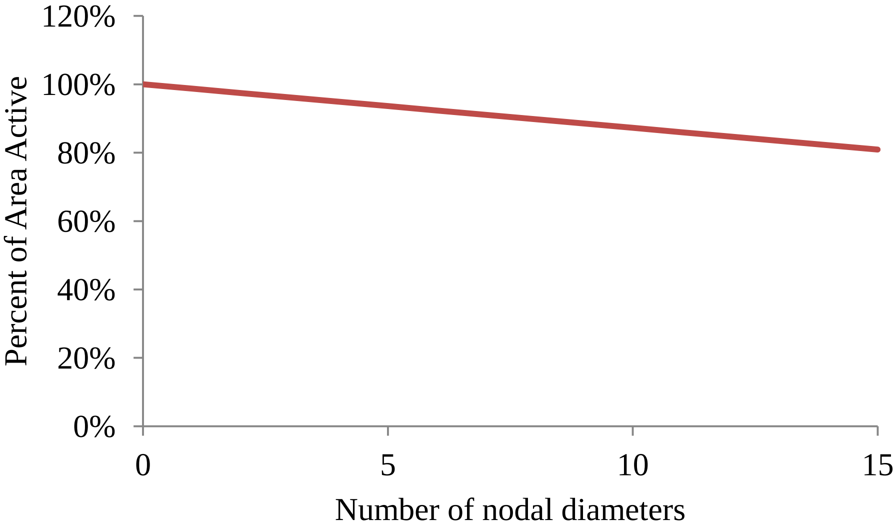

Figure 3.12. Inactive area between electrodes, increasing as mode number increases

Modes with less than three nodal diameters were not of interest because the number of nodal diameters is also the number of anti-nodal peaks. If there are fewer than three peaks which travel about the stator, then the rotor would not be stably supported. By using a higher order mode, the rotor can always be supported by three or more points of contact. For these reasons, stators were designed for resonance excitation with three nodal diameters.

Two factors then separate the choice between the B_{03} mode and the B_{13} mode. The B_{03} mode, having no nodal circles, occurs at a much lower frequency, but can accordingly achieve higher out-of-plane deflections. Because high-frequency operation and large out-of-plane deflections are both important for motor performance, there is an inherent trade-off between the B_{03} and B_{13} modes. For the present stators manufactured using the described method, the deflection was limited by the buried oxide thickness, and this maximum allowable deflection was achievable using the B_{13} mode, so the higher frequency actuation allowed for better motor performance. Another minor advantage of using the B_{13} mode over the B_{03} mode is that a small portion of the peak motion in the B_{03} mode is directed perpendicular to the rotor motion (towards the center of rotation). All of this motion and the associated frictional energy is wasted during operation, resulting in less efficient drive. This is highlighted in Figure 3.13.

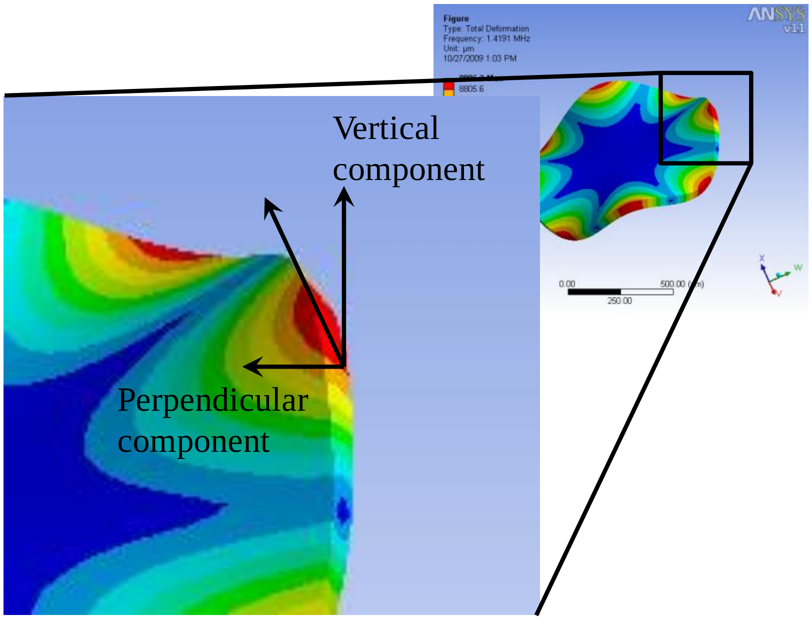

Figure 3.13. ANSYS simulation of the B_{03} mode highlighting a portion of stator motion is perpendicular to rotor travel, resulting in lost energy.

3.1.3 Single Source Drive

A unique design for traveling wave ultrasonic motor operation is described in [53], where the natural phase offset due to resonance is exploited to create the phase mismatch between the offset electrodes. In traditional TWUM, the phase offset is created by two separate sources, thus requiring duplicate components to generate the phase-offset signals. By slightly distorting the disc or ring as shown in Figure 3.14, a designer can introduce a frequency shift in one mode, causing the degenerate modes to split in frequency.

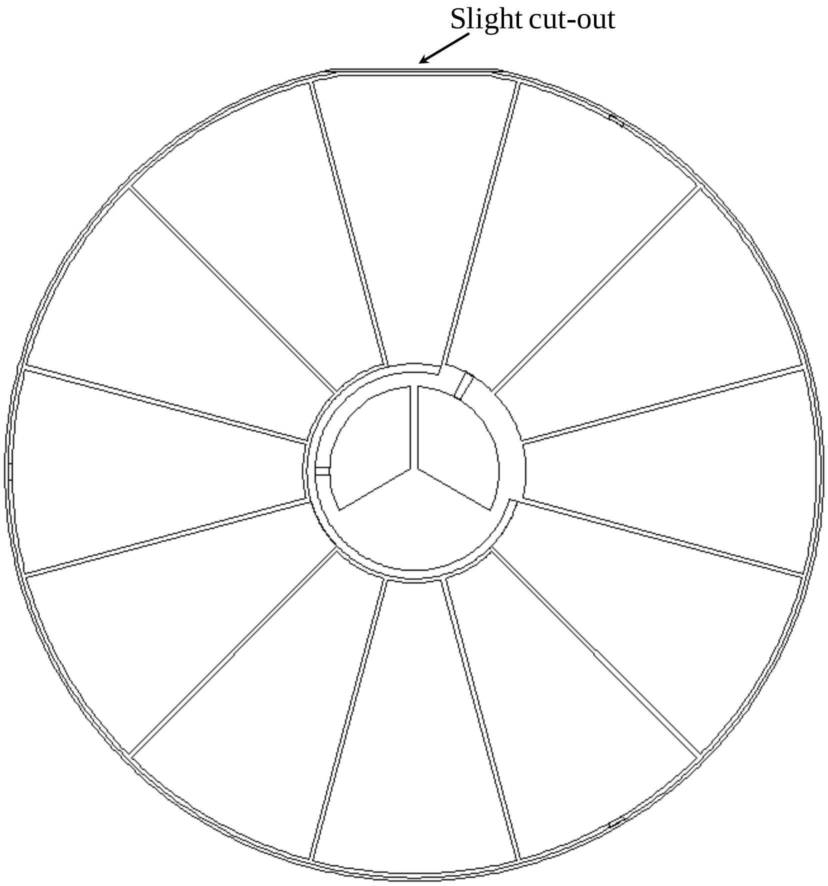

Figure 3.14. Schematic illustration of a distorted disc creating a natural frequency offset between degenerate modes.

Because the phase response of a system shifts dramatically near the resonance frequency, this designed frequency split can be used to create a phase offset if the modes are actuated at the same frequency. A sample simulated frequency response plot is shown in Figure 3.15, highlighting the phase offset that can be achieved by exploiting designed frequency split. This phenomenon was observed experimentally when a stator with slight fabrication asymmetries was actuated with two signals with zero phase offset. In this configuration, rotation of a test rotor was observed, suggesting that the fabrication asymmetries created a natural phase shift in the stator response. This result is described in more detail in Section 5.3.

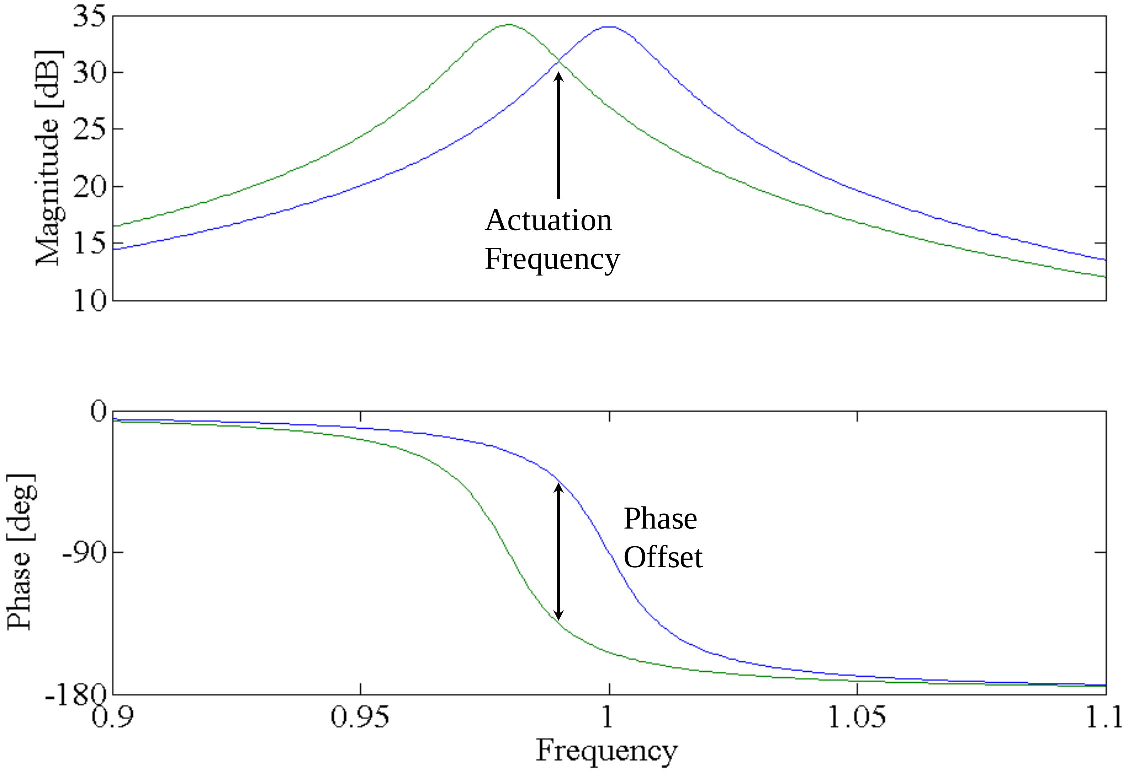

Figure 3.15. Simulated frequency response plot for the distorted disc in Figure 3.14 showing the phase offset from frequency offset.

3.2 Disc Stator Characterization

This section will detail the characterization methods and results for the disc stator. Included within is an exhibition of a traveling wave in a stator (measured using a Polytec MSV laser Doppler vibrometer), discussion of standing wave characterization, and analysis of nodal line control and nonlinear effects. Asymmetric anchor conditions that distort the resonance characteristics of the disc are also presented.

3.2.1 Traveling Wave and Frequency Characterization

A controlled traveling wave was induced in the fabricated stators using two input sinusoid waveforms, 90° out of phase. Figure 3.16 illustrates the traveling wave using phase-stepped LDV data. Because of the stator surface deforms at the driven frequency, measurements can be taken at each point on the stator surface over a span of minutes. These measurements can be combined by using the phase of the drive signal as a reference to match the measurements at each point. This results in a surface plot that changes according to the input phase of the drive signal. This representation illustrates the deformation of the stator over a single cycle of the input signal, equivalent to 4 μs, resulting in the wave progressing approximately 120° around the disc.

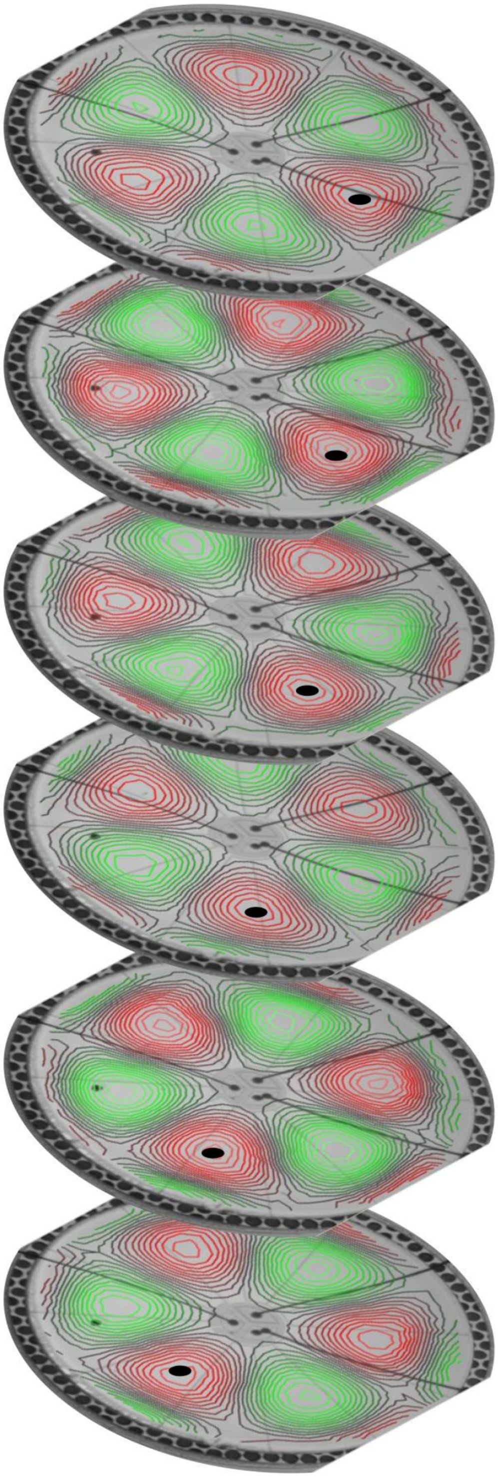

Figure 3.16. A traveling wave is visualized using phase-stepped LDV data representing 120° of spatial wave travel in the stator over 4μs (i.e. one cycle of the input sinusoid). The black marker helps to track the anti-node as it travels about the disc.

The traveling waves were generated by exciting standing waves in phase and apart in space according to the identity in Equation 3.2.

$$\cos(n\theta)\cos(\omega t) + \sin(n\theta)\cos(\omega t) = \cos(n\theta - \omega t) \tag{3.2}$$

To characterize the standing waves, sinusoid input waveforms were applied at the predicted resonance frequency to excite the resonance mode shapes within the stators. LDV was then used to determine the shape of the mode present. The experimentally measured resonance mode shapes for the B_{04} and B_{13} modes, shown in Figure 3.17 and Figure 3.18, match the mode shapes determined by FEA in Figure 3.6 and Figure 3.7.

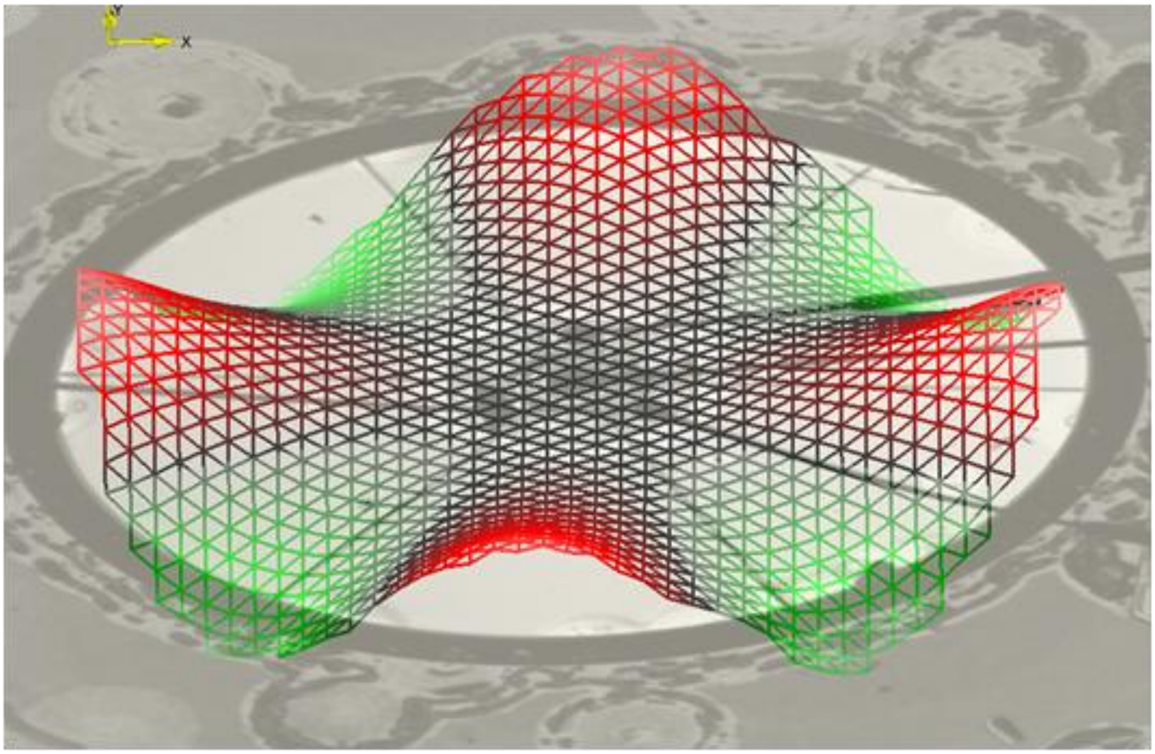

Figure 3.17. LDV data showing the mode shape matching the simulated B_{04} mode shape in Figure 3.6. The B_{04} mode occurs in this disc at 109 kHz.

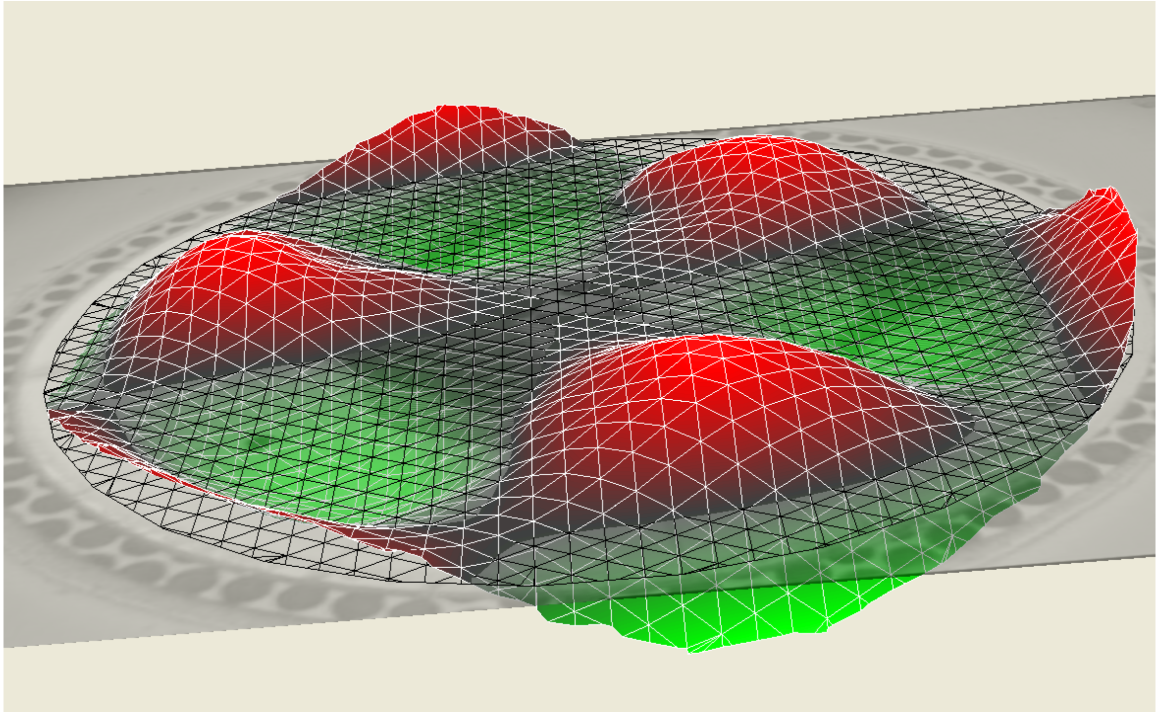

Figure 3.18. LDV data showing the mode shape matching the simulated B_{13} mode shape in Figure 3.7. The B_{13} mode in this disc occurs at 252 kHz.

Experimental determination of the resonance frequencies was performed by inputting 0 to 10 V white noise signal, using a waveform generator, and measuring the response using a Polytec MSV LDV. A Fourier transform was performed on this data to determine the frequencies of greatest amplitude. These frequencies were then isolated and examined to determine the mode shape present at each resonance frequency. Figure 3.19 shows the z-axis frequency response of a single point, near 800 μm from the center of a 3 mm diameter disc up to 1 MHz, created using a white noise input signal. The frequency plot in Figure 3.19 illustrates a number of resonance modes that may be excited in the stator. In contrast, with a sinusoid input at the B_{13} resonance frequency, no other significant peaks were observed in the frequency response of the stators.

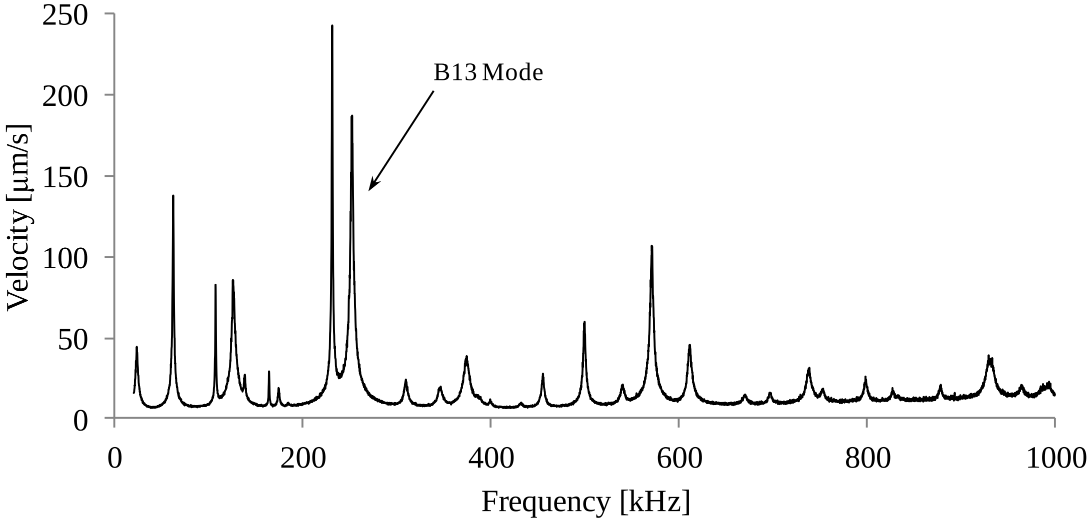

Figure 3.19. Total frequency response measured using laser Doppler vibrometry at a single point on the stator under 0-10V white noise excitation. The B_{13} mode is highlighted here around 250 kHz.

The desired B_{13} mode was further characterized for the effects of frequency and voltage on the deflection of the surface. Sinusoids of single frequencies were input to a single electrode on the stator and the maximum displacement was determined with the LDV by scanning across the entire disc and determining the largest deflection. The results of this characterization are shown in Figure 3.20 for a 2.5 mm disc. From this plot it is clear that frequency and voltage both significantly affect the response. Here electrode A and B represent adjacent electrodes on the same device, illustrated in Figure 3.11 as $\sin(\omega t)$ and $\cos(\omega t)$ respectively.

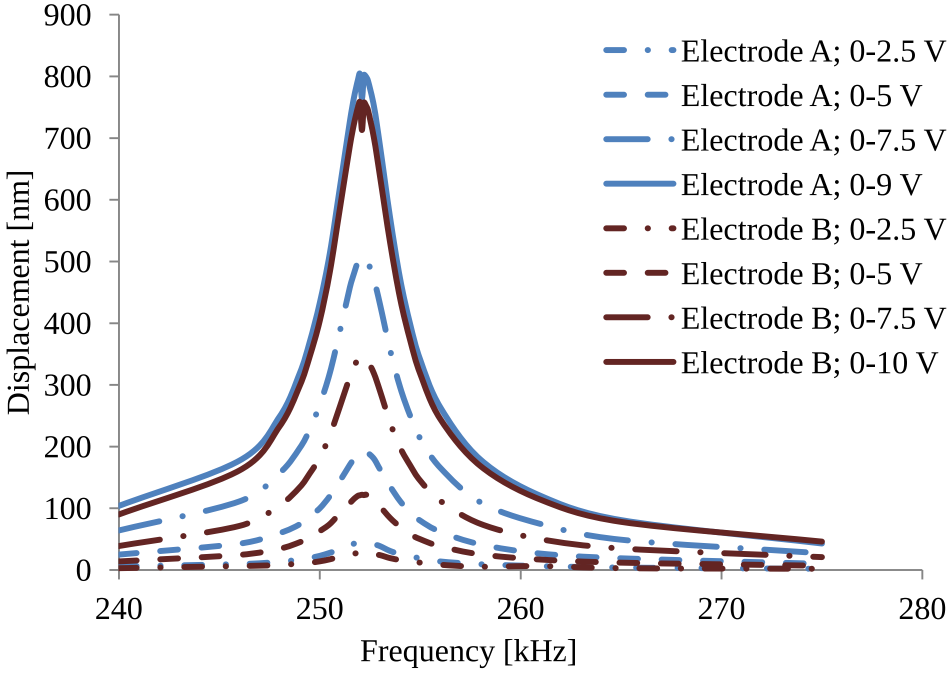

Figure 3.20. The frequency response of a 2.5 mm diameter disc stator comprised of 30 µm device Si layer illustrating the effect of voltage on displacement of the B_{13} mode over a narrow frequency range. Electrode A was only driven to 9 V because contact with the underlying substrate occurred at higher voltages.

Beyond the simple qualitative conclusion that voltage and frequency affect amplitude, one can note specifics about the system. First, it is an easy extrapolation to approximate the mechanical Q-factor as below Equation 3.3.

$$Q = \frac{f_p}{\Delta f} \tag{3.3}$$

Here, f_p is the peak frequency and Δf is the bandwidth, defined as the difference between the upper and lower frequency where the response reaches half of the maximum amplitude. Performing these calculations for each of the electrodes and voltages gives the mechanical Q-factors as recorded in Table 3-2.

Table 3-2. Calculated Q-factor in discs driven at various voltages

Condition	Q-factor
Electrode A; 0-1 V	93.9
Electrode A; 0-2.5 V	93.4
Electrode A; 0-5 V	93.8
Electrode A; 0-7.5 V	93.4
Electrode A; 0-9 V	91.4
Electrode B; 0-1 V	95.5
Electrode B; 0-2.5 V	97.6
Electrode B; 0-5 V	95.9
Electrode B; 0-7.5 V	94.6
Electrode B; 0-10 V	92.9

From this we can see that for the 3mm diameter stator all conditions display a Q-factor near 95. For Q-factors larger than 10, the damping coefficient, ζ, can be approximated as 1 / 2Q. Under this approximation, the evidence suggests that damping in the stator system is not related to displacement magnitude. It can be determined from this that squeeze film damping, which is highly related to vibration amplitude, is not active in the analyzed stator system [54].

Another important factor in characterizing the standing waves generated is the location of the nodal lines of the standing waves. In a disc, there are infinite lines of symmetry, resulting in infinite potential locations for nodal lines. In reality, the nodal lines are fixed by small imperfections that preferentially locate the nodal lines to a specific position. This preferential location is generally random, however by exciting electrodes shaped to excite the mode shape, one can overcome the small imperfections in the disc and control the nodal line location by design. Specifically, the anti-nodes of the standing waves align with the center of the shaped electrode. Figure 3.21 shows the laser Doppler vibrometer measurements for electrode A in (a) and electrode B in (b) illustrating the control of nodal line location. This nodal line control allows for the generation of standing waves offset in space by a quarter-wavelength.

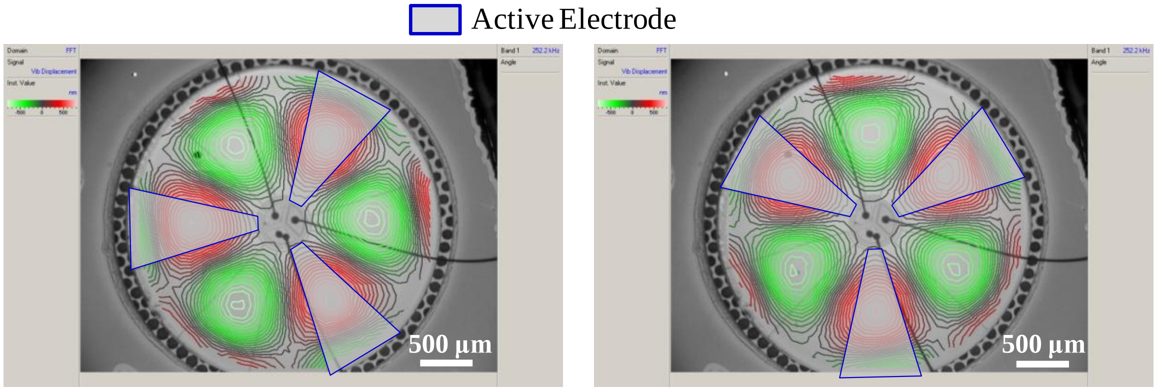

(a) (b)

Figure 3.21. Laser Doppler vibrometer measurements for electrode A (a) and electrode B (b), showing the control of nodal line location.

3.2.2 Nonlinear Deflection Characteristics

Another point that can be made from the data is that the relationship between voltage and maximum displacement is nonlinear in nature, as shown in Figure 3.22. The nonlinearity is quite strong, accounting for over 60% of the calculated displacement at only 5 V peak actuation.

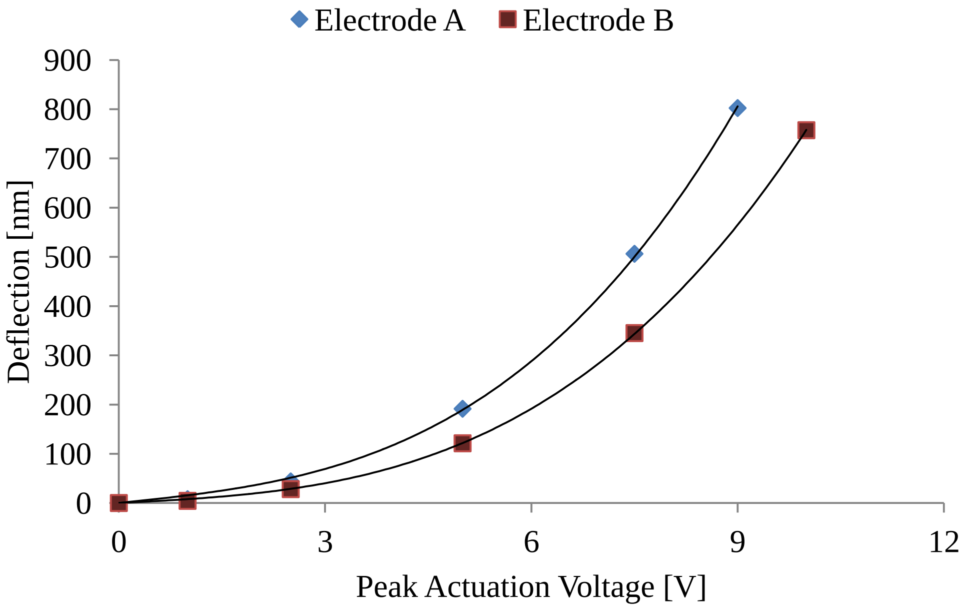

Figure 3.22. Nonlinear increase in deflection under changing peak voltage is due to voltage sensitive piezoelectric properties.

It was expected that vertical deflection would be directly proportional to the peak-to-peak actuation voltage, however the nonlinearity present in the response suggests that something else is acting on the system. This nonlinearity comes from the fact that as the peak actuation voltage is increased, the DC bias voltage is also increasing (e.g. 0 to 4 V has a DC bias of 2 V, while 0 to 8 V has a DC bias of 4 V). This DC bias changes piezoelectric response of the PZT film as described in [55]. The peak e_{31} occurs at the coercive voltage, meaning that when the DC bias reaches the coercive voltage, the response will increase less rapidly. In the experimental stator system, the 10 V peak voltage (associated with a 5V DC bias) coincidentally aligned with the coercive voltage, also near 5 V. This led to the nonlinear trend observed in Figure 3.22. To support this claim, deflection data was taken with a constant 2 V peak-to-peak signal with varying DC bias, and is presented in Figure 3.23. This effect of DC bias on piezoelectric properties is important for design of thin film TWUM devices as well, as other piezoelectric devices that rely on constant bias superimposed on a sinusoidal waveform.

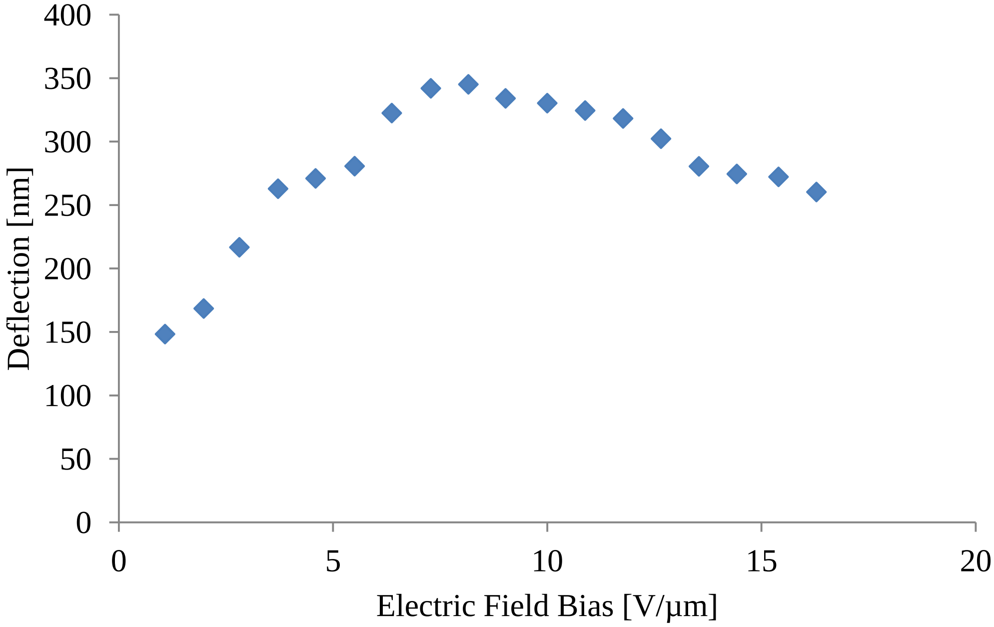

Figure 3.23. Stator deflection measurements from constant peak-to-peak voltage and varying DC bias shows a similar trend as seen in [55], suggesting that the nonlinearity observed in Figure 3.22 derives from a changing e_{31} with bias voltage.

3.2.3 Anchor Effects

Stators 1 mm in diameter did not operate as designed due to mode mismatch. Specifically, the orthogonal modes occur at different frequencies. This prevents the creation of the traveling wave because the identity requires two standing waves at the same frequency. Furthermore, the anti-nodes of the mode shape are not localized to the active electrode as described in Section 3.2.1, but instead the anti-nodes are set somewhere between the active electrodes. The simplest explanation is that there is a component in the system which is changing the modal stiffness or mass so that the resonance frequencies shift and the nodal lines are fixed by this component rather than the active electrodes.

To identify this component, it is important to note a number of factors. First, all 1 mm diameter stators showed similar frequency offset and similar nodal line locations. This systematic consistency suggests that the problem is likely not random and also not material defect related. Therefore it is essential to examine the design of the stator to identify possible sources of this problem. Second, the modal shift is present only for small diameter devices, whereas larger diameter devices show no problems. Finite element simulations during the design phase showed that smaller devices are more affected by the anchor condition than larger devices. Finally, upon examining the design, the backside release holes, shown in Figure 3.24, are varied in size and shape near the anchor portion so as to create a circular anchor, which would prevent any mode mismatch.

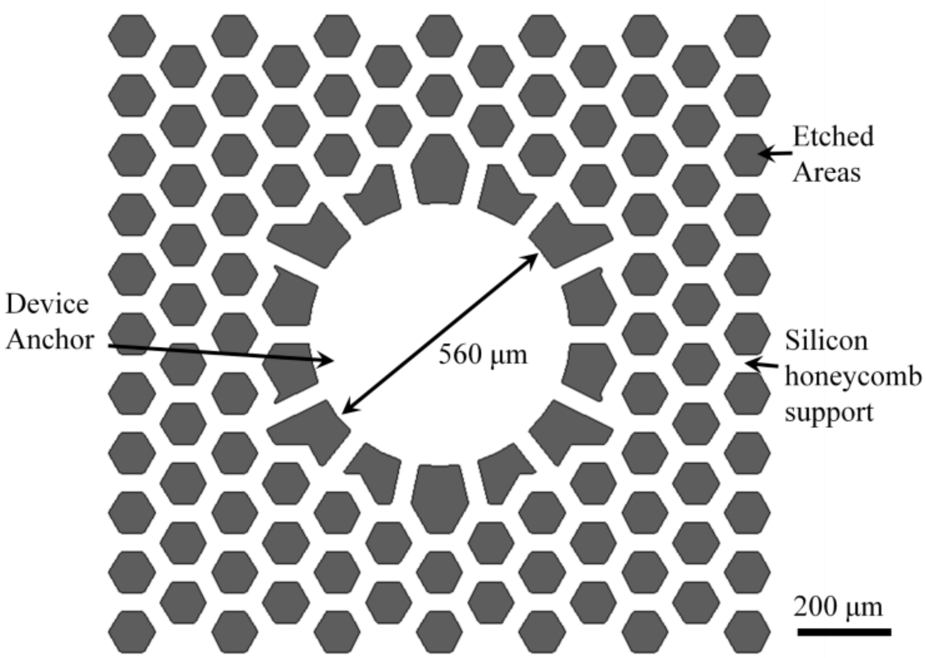

Figure 3.24. Illustration showing the photolithographic pattern used to etch the handle wafer for vapor HF release. Note the holes of various sizes at the center.

The large holes align to the anti-nodes of the experimentally observed lower frequency modes suggesting that the larger holes reduced the stiffness for deflections coincident with these holes, thus dropping the resonance frequency for that mode. These observations lead to the next question – how does the size of the hole affect the stiffness of the structure? To remind the reader, the holes are etched through the approximately 500 µm thick handle wafer to open the buried oxide to a vapor HF etch, while maintaining the structural integrity of the handle wafer silicon. It is suggested that a larger volume of the etch gas is delivered through the large etch holes, and thus the etch front progresses faster in the vicinity. The faster etch rate would leave a hexagonal anchor which would create the modal mismatch observed experimentally. This argument is illustrated in Figure 3.25.

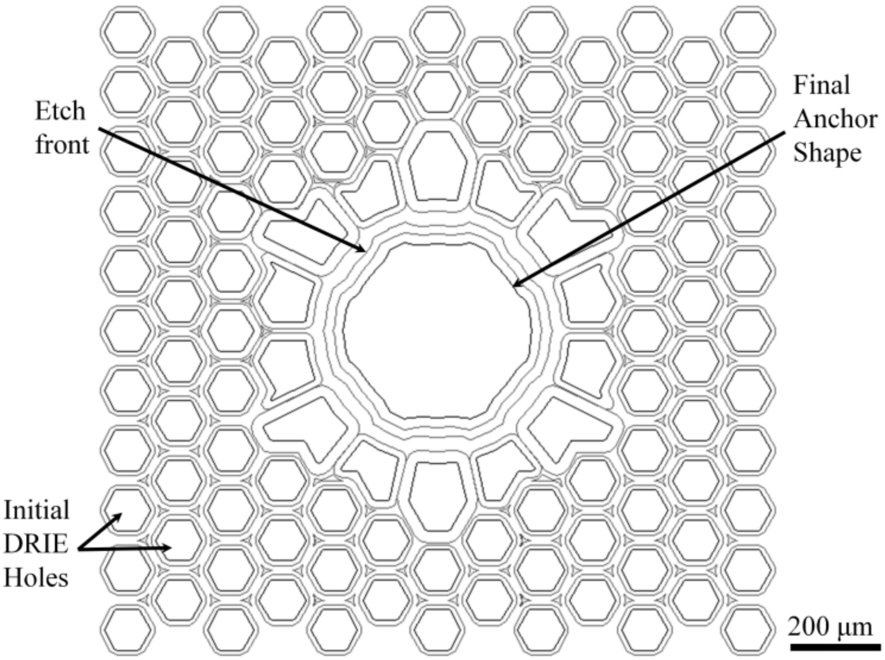

Figure 3.25. Illustration of the simulated etch front progression (gray lines) showing the asymmetric etching leading to a non-circular anchor.

The buried oxide etch-front, usually visible using infrared imaging, cannot be observed in this case because the through wafer holes prevent sufficient contrast to observe the etch-front. Although the buried oxide etch-front is not easily observable, the argument that asymmetric etching of the buried oxide creates modal mismatch seems to hold weight as a likely explanation. Assuming this is the problem, Figure 3.26 shows a possible design solution which uses holes that are all approximately the same area, allowing the etch front to progress at the same rate.

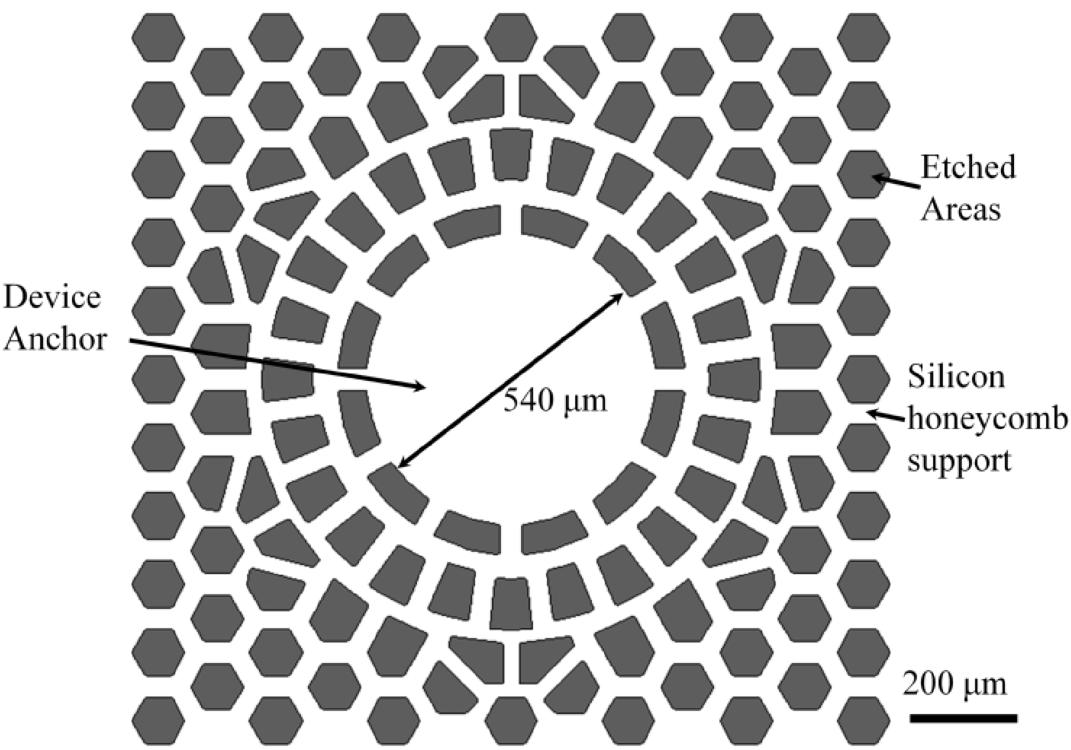

Figure 3.26. Illustration of a new etch hole design to alleviate problems with uneven etching during vapor HF release due to size of etch hole.

The resulting etch progression and anchor condition are shown in Figure 3.27. Furthermore, any etching asymmetries caused by the twelve holes near the anchor will be matched by the twelve regions of excitation, thus eliminating mode mismatch problems that were observed under the previous design.

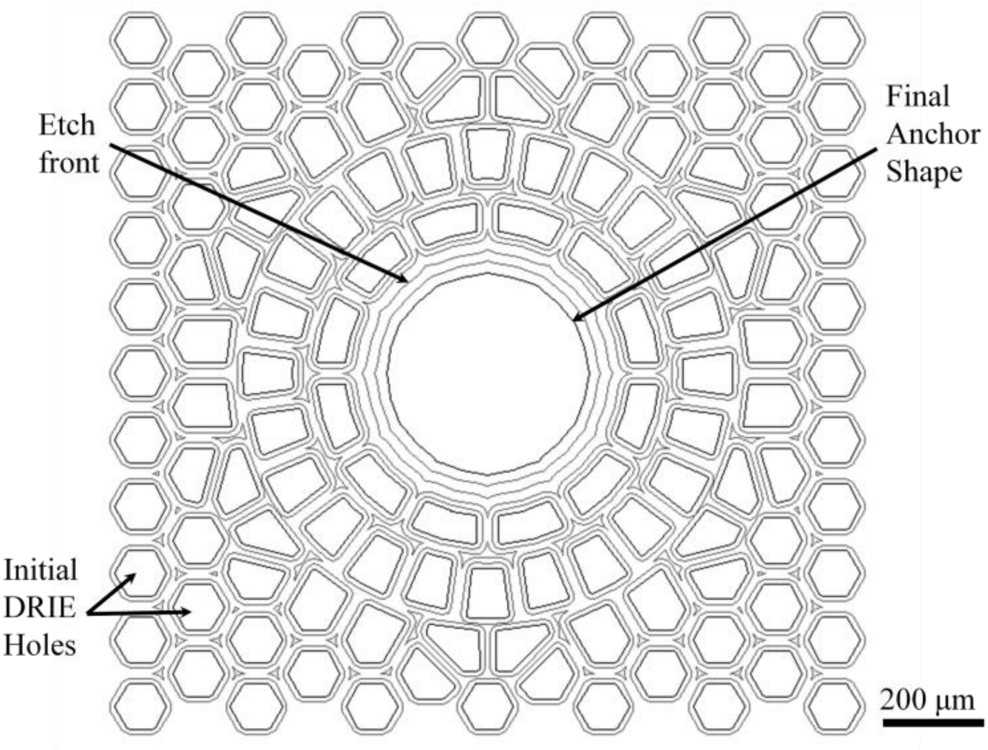

Figure 3.27. Illustration of the simulated etch front progression (gray lines) showing a significantly more symmetric center anchor, which should allow for smaller devices to function without mode-splitting.

This design problem emphasizes that these motors can be quite sensitive to boundary conditions. Because of this sensitivity to boundary conditions, the design of the motor must be done carefully, ensuring that modal mismatches are avoided or mitigated whenever possible.

3.3 Summary

This chapter outlines the design and characterization of disc stators for traveling wave ultrasonic motors. These stators were designed using finite element analysis and macro-scale motor design templates. Stators 1-3 mm in diameter and 20-30 μm thick were fabricated and were characterized using laser Doppler vibrometry, demonstrating out-of-plane deflections on the order of 1 μm and quality factors of 95 in air. Frequencies from 50-600 kHz were investigated depending on mode shape and device geometry. Traveling waves were demonstrated and characterized using laser Doppler vibrometry. These traveling wave ultrasonic stators are the key enabling development for a thin-film miniature TWUM. These results are summarized in Table 3-3.

Table 3-3. Summary of stator geometry and performance specifications

Parameter	Value
Stator diameter	1 - 3 mm
Stator thickness	20 - 30 μm
Actuation frequency	50 - 600 kHz
Deflection	0 - 1 μm
Quality Factor	95

4 Ring Stator Design and Characterization

The disc stator described in the previous section has an important place in the micro-fabricated ultrasonic motor landscape, however there are some advantages offered by ring stators that make this stator configuration attractive. These benefits and the work to design, test, and demonstrate these ring stators is contained within this chapter.

4.1 Integration Benefits

As mentioned above, ring stators hold advantages over disc stators. The two benefits highlighted here will be the location of electrical contacts, and a hollow center configuration. Both of these advantages offer an expanded range for new mechanisms, design integration, and simplified implementation. Each will be discussed separately below.

4.1.1 Electrical Contact Location

In microelectromechanical systems, packaging and integration are some of the most complicated, and often least appreciated, factors in research. The electrical contact location of the ring stator addresses the interconnect challenges with the disc stator. In the center-fixed disc TWUM configuration described in the previous chapter, the contact pads of the stator are located at the center of the disc, co-located with the common nodal point and the device anchor. In isolation, this configuration is ideal for a traveling wave ultrasonic stator because the contact pads and the anchor are located where there is very little motion (at the common nodal point), meaning that the anchor and electrical contacts (and associated bond wires) have very little effect on the stator dynamics. Furthermore, the anchor located at the nodal point allows for little energy to be lost through the anchor to the substrate. This low energy loss results in a high quality factor, which produces larger deflections during resonance operation. Again, this center-fixed disc configuration is ideal for traveling wave ultrasonic stators taken in isolation, however when considering the stator within the larger context of a motor and system, it becomes apparent that the center-fixed disc has significant drawbacks. The chief difficulty is that the wires which bring signal to the stator must be brought through the center of the rotor (unless there is significant advancement in through-wafer via technology). Labor intensive, meticulous, manual wirebonding can be used to contact the stator, however, large wire loops are required so that the wire does not restrain rotor motion. This through-rotor wirebonding requirement limits the types of rotors which can be used, preventing components from being placed at the rotor center and eliminating use of disc-shaped rotors.

Ring stators offer an alternative to interconnect challenges in the disc stator. The integration and packaging problem is taken as the chief concern, with creative design employed to address functionality drawbacks. In this ring stator configuration, the electrical contacts are located at the edge of the device die, allowing easy wiring, and simplifying the rotor integration process. With the electrical contacts located outside the frame of the stator, it is possible to have a continuous rotary platform, allowing a component to be located at the center of the rotor. Furthermore, a variety of components can now easily interface with the stator surface, for example, a micro-ball bearing rotating stage [56]. These benefits are illustrated in Figure 4.1.

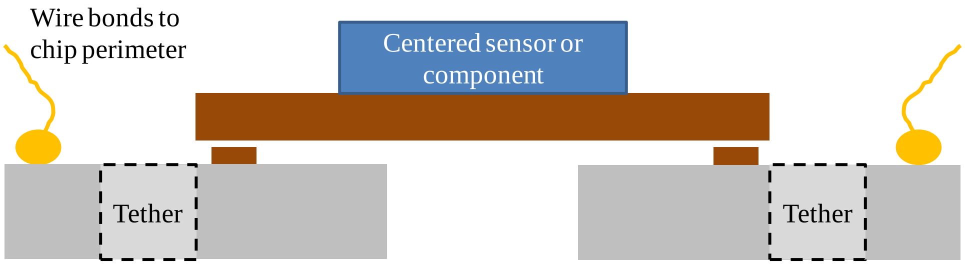

Figure 4.1. Schematic cross-section illustrating the electrical contact location at the chip perimeter to simplify rotor/component integration and wirebonding in ring stators.

4.1.2 Hollow center

The second advantage highlighted above is a hollow center. This feature, though initially uninspiring, creates new opportunity for functionality and utility that could not exist with center-fixed disc stators. One example that can be extended from macro-scale TWUM in cameras is use of the hollow center as viewing hole for optical purposes. This could have potential for miniaturized motors applied to mobile cameras. Wires could also be routed through the hollow center, which would be useful for in miniature devices, which do not have access to micro-slip rings. For example, multiple motors in a kinematic chain could be realized with this approach. Finally, the hollow center could be exploited to produce increased torque by vertically pre-loading the motor. Since the stator drives the rotor through frictional coupling, vertical pre-load results in a higher frictional force and more torque. Applying force at the center of the rotor would allow for the mechanical advantage at the contact points to overcome the frictional resistance from the static component. Since in this configuration, the rotor is inaccessible because of the preloading mechanism, the backside of the handle wafer can be used as the rotor surface. This configuration is illustrated in Figure 4.2.

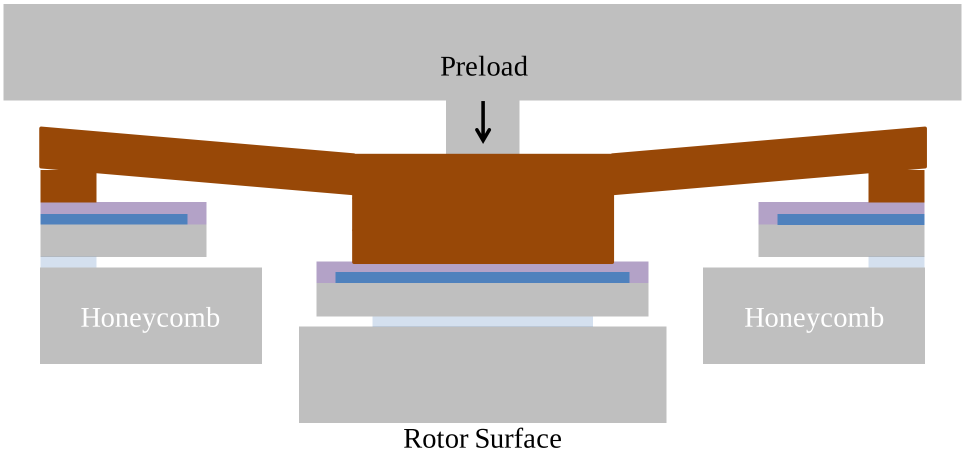

Figure 4.2. Schematic cross-section of the backside rotor configuration showing a possible path to preload that would not be feasible without using a ring stator.

4.2 Ring Stator Drawbacks

Ring stators bring drawbacks that accompany the benefits described above, of specific importance: mechanical support and electrical traces.

4.2.1 Mechanical support

In macro-scale ring stator motors, felt is used as a mechanical support. This allows for the static load to be supported, but the high frequency vibrations to be unimpeded. In a millimeter-scale motor, this support mechanism is impossible. Instead, the ring must be supported from the edge. Supporting the stator ring from the inner edge accomplishes little, as the resulting device would have many limitations similar to disc stators. Supporting the ring stator from the outer edge via tethers allows for a static load to be supported in micro-scale applications, especially MEMS resonators. These tethers introduce new limitations because the support limits the edge deflection of the stator, and the added stiffness affects the resonance behavior of the stator.

4.2.2 Electrical traces

In center-fixed disc stators, the electrical contacts are deposited at the center of the active PZT regions. In ring stators, the electrical pads are located at the edge of the die, so electrical traces need to be included in the design. These electrical traces bring electrical signal to the stator where the PZT is located. The tether described above creates a good platform for electrical traces because it links the anchored substrate, where the bond pads are located, to the stator structure.

4.2.3 Tether effect

Although these tethers address some of the drawbacks of ring stators as they are applied to traveling wave ultrasonic motors, they also introduce challenges of their own. These challenges are discussed below, specifically: shifted resonance, distorted mode shape, dissipated energy, and prevented wave travel.

4.2.3.1 Shift resonance frequency

As has been emphasized throughout, resonance characteristics of the TWUM and the ultrasonic stator are extremely important for proper motor operation. The tethers, added to create mechanical support and provide platforms for electrical traces, affect the resonance characteristics of the stator. Initial attempts at creating a ring stator resulted in severe mode mismatch between the primary orthogonal modes, as shown in Figure 4.3. This figure shows micrographs of a stator with the two orthogonal modes superimposed as measured experimentally using laser Doppler vibrometry.

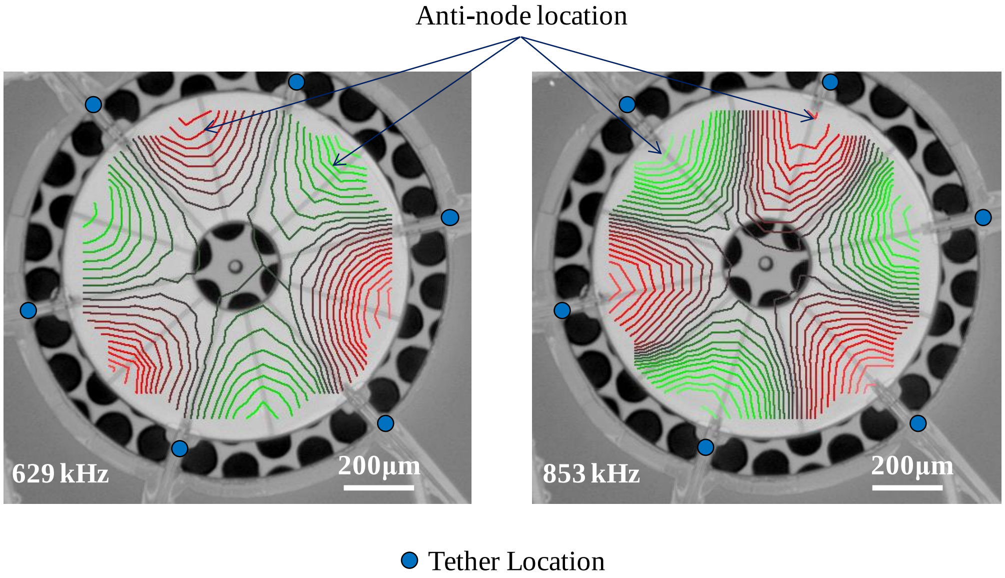

Figure 4.3. Laser Doppler vibrometry data shows frequency mismatch of 35% between orthogonal B_{03} modes. This mismatch means that traveling waves cannot be generated.

The frequency mismatch between the orthogonal B_{03} modes depicted in Figure 4.3 is 224 kHz. At a resonance frequency of 629 kHz, this amounts to a frequency offset of 35%. As described in Section 1.1, a traveling wave is generated by superimposing orthogonal standing waves, excited at the same frequency, but out of phase. Because the frequencies are so drastically different, it is impossible to excite a traveling wave in this stator. This frequency shift arises from the added stiffness from the tether. Because the tether links the edge of the disc (which experiences the peak motion) to the anchored substrate, the stiffness of the tether can have large influence on the overall stiffness of the system. In this specific example, the mode with nodal lines along the tethers is largely unaffected by the presence of the tethers. The orthogonal mode, however, has the antinodes aligned to the tethers, so the tether stiffness is extremely important in determining the modal stiffness of this mode.

4.2.3.2 Distorted mode shape

Beyond shifting the resonance frequencies, the tethers also distort the mode shapes. This is important because these mode shapes are the standing waves that combine to create a traveling wave. Repeating Equation 1.2 from Section 1.1, is helpful for illustrating this point.

$$w(r,\theta,t) = A_{mn}(r)\cos(n\theta)\cos(\omega_{mn}t) + A_{mn}(r)\sin(n\theta)\sin(\omega_{mn}t) \qquad (1.2)$$

In this equation, the value A_{mn} is the amplitude of the standing waves. If the amplitude is suppressed in one of the mode shapes, however, the equation becomes Equation 4.1:

$$w(r,\theta,t) = A_{mn}(r)\cos(n\theta)\cos(\omega_{mn}t) + B_{mn}(r)\sin(n\theta)\sin(\omega_{mn}t) \qquad (4.1)$$

In this form, the trigonometric identity in Equation 1.3 no longer holds and there will be a residual beat in the traveling wave response. This means that as the wave travels around the stator, it will vary in amplitude. This variation in amplitude then results in varied tangential speed at the stator-rotor surface. The speed variation means that the rotor speed will not properly match the stator tangential speed. This speed mismatch reduces the efficiency of the motor and could create localized wear on the stator component.

The tether not only suppresses the amplitude of the standing wave but it also distorts the shape itself. Figure 4.4 shows two rings expressing corresponding modes, one a free ring, one with anchored tethers.

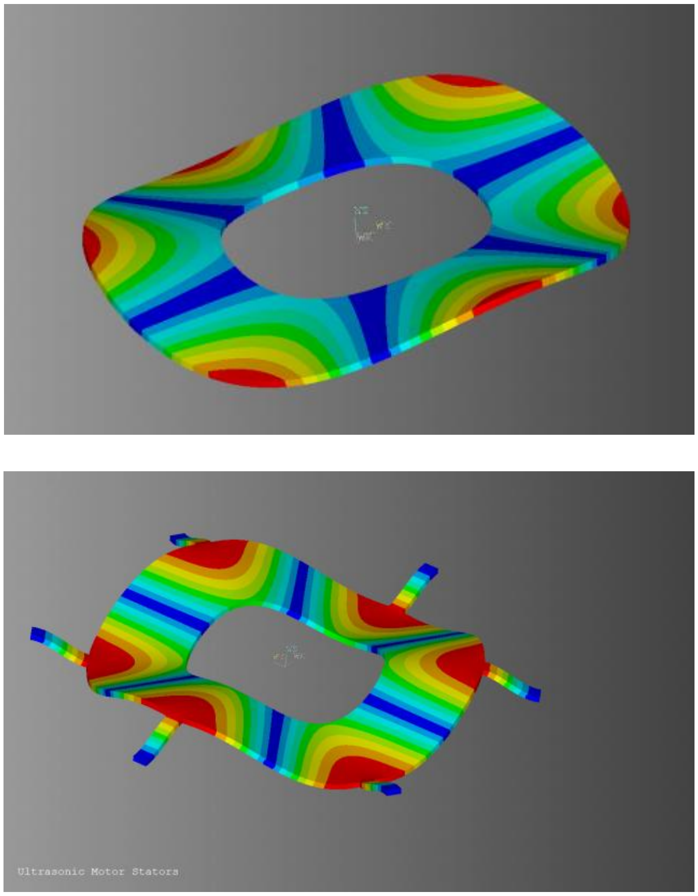

Figure 4.4. FEA simulations illustrating two rings displaying the B_{03} mode shape distortion arising from added stiffness from the tether. This distortion can be problematic for motor operation.

As shown in Figure 4.4, the shape of the resonance mode is changed by the tethers. This change in shape means affects the shape of the wave as it travels around the ultrasonic stator. Equation 4.1 can again be used to show that if $A_{mn}(r)$ is modified, then the traveling wave is distorted. Another important factor is that if the shape is distorted, the location of peak amplitude can shift. Since the stator contacts the rotor at the location of peak amplitude, the contact location can vary around the motor. Contact location is important because quantities like torque and rotational speed are directly related to contact radius. For example, if the contact radius is reduced by 5%, the rotational speed is increased by 5% if the tangential speed is kept constant. This similarly leads to uneven wear and lower efficiency.

4.2.3.3 Dissipates energy

Another important factor to be considered when including tethers into a design is the dissipation of energy into the substrate. Since the tethers are linked to the resonant system at one end, and the anchored substrate at the other, the energy in the stator system can be lost through the tether into the anchored substrate. This energy loss is extremely important because it reduces the quality factor of the system. This reduction in quality factor reduces the motion amplification at resonance, meaning that the stator deflects out of plane less. Because motor performance is directly linked to stator deflection, this reduced out of plane deflection reduces motor speed and potential torque output.

Often when resonant microsystems are suspended with tethers, the attachment point of the tether is a nodal point of the system, such as a length extensional resonator as shown in Figure 4.5. Since this nodal point experiences very little motion, the energy lost through the tether is small. In the traveling wave stator, however, there is no nodal point to attach a tether since the wave travels about the stator at constant amplitude.

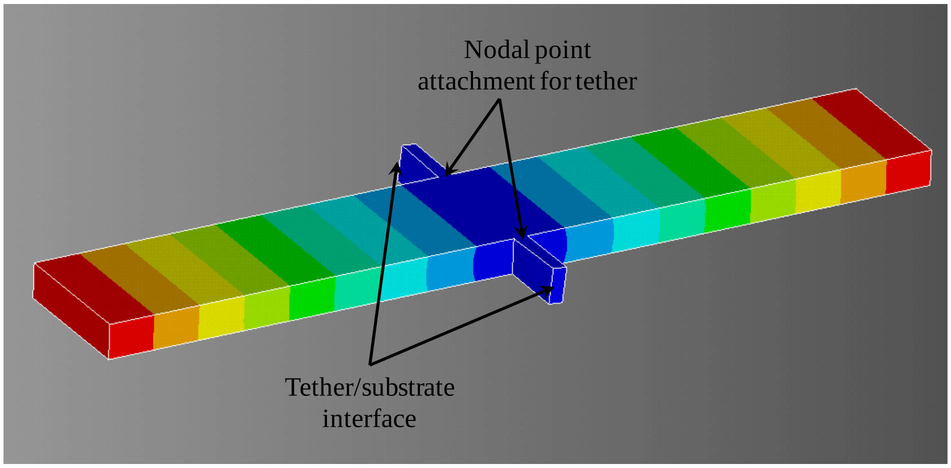

Figure 4.5. A length extensional resonator showing the tether located at the nodal point.

Even in these systems with convenient nodal points for tether attachment, ongoing research has been focused on further reducing tether-related losses in order to increase quality factor. This reduction is often performed either by creating compliant tethers that reduce energy radiated due to impedance mismatch, or by matching the length of the tether to the quarter-wavelength of the vibration in the system, reflecting the energy back into the system. In a traveling wave ultrasonic stator, the compliant tether cannot be used because the mechanical support from the tether is required to support the normal force from the rotor. Without some normal force, there would be no friction force that could be supported. The quarter-wavelength design is also incompatible with traveling wave ultrasonic stators because when the edge of the stator deflects, the stiffness of this tether creates the distortions described in Sections 4.2.3.1 and 4.2.3.2. Furthermore, the length of the tether would change during the out-of-plane motion, spoiling the quarter-wavelength matching.

4.2.3.4 Prevents wave travel

The final note on the undesirable effects arising from a tethered traveling wave stator is that the tethers prevent proper wave travel in the stator. In disc stators, if only two sectors of a 12 sector disc are active, the wave will still propagate at nearly constant amplitude, however in these tethered ring devices, the wave is quickly distorted. This observation confirms that the effects described above are not simply ancillary details, but rather essential challenges for the realization of a tethered ring TWUM.

4.3 Tether design

In the previous sections, the undesirable effects caused by tethers on traveling wave stators were examined. This section describes the process and design used to create a tether which mitigates the described effects, while still providing mechanical support and electrical connection to the stator platform.

4.3.1 Straight tether varying lengths

Initial experiments in tethers included ring stators of various sizes, with straight tethers of varying length. The objective was to determine how long the tethers must be in order to sufficiently mitigate the above-mentioned effects. Once the devices were fabricated, it became clear that even the extremely long tethers were not compliant enough because the resonance frequencies of orthogonal modes were always offset by more than 10%.

4.3.1.1 Simulation of straight tethered rings

To determine the relationship between tether length, straight tethers of various length were simulated in ANSYS finite element software. These simulations determined the resonance frequencies of the two orthogonal modes: one with nodes aligned with the tethers, and the other with anti-nodes aligned with tethers. These frequencies were then compared to the free case and to each other to determine the relationship between tethers and frequency shift. The results of this simulation study are shown in Figure 4.6.

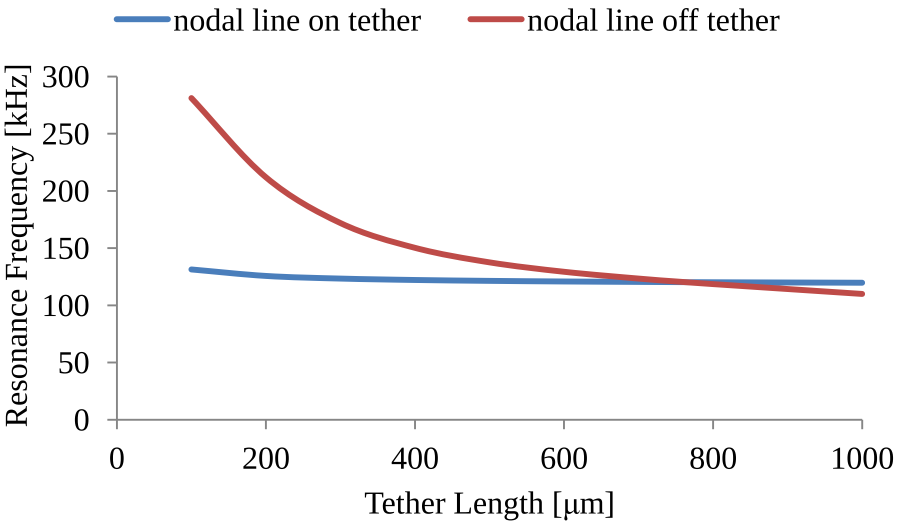

Figure 4.6. Simulation study of tether length and frequency offset between orthogonal modes showing that extremely long tethers are required for frequency matching.

From this study, it was determined that a new design must be employed, which permits the desired motion in the stator, while mechanically supporting the stator because a 750 µm long tether would nearly double the total device size.

4.3.2 Dynamics-driven tether design

Because the conventional designs for low-loss tethered microsystems were unacceptable, a new design was developed for traveling wave stators. In this design, the tether was viewed as its own resonant system, and was matched to the resonator, acting as a mechanical impedance transformer. This concept is described in [57], where resonator tethers are designed to reduce loss at the anchor attachment point. By selecting tether designs that admit large motion at the attachment point and experience small relative strain at the substrate anchor, high anchor quality factors can be achieved. This method of tether design proved to be effective for a wide bandwidth, contrary to quarter-wavelength tether designs. This method is adapted to the more complex conditions presented by the traveling wave ultrasonic stator as described below.

4.3.2.1 Boundary conditions

As described above, conventional techniques for lowering loss through tethers in resonators relies chiefly on the placement of the tethers at nodal points of the system. This is true of the resonators described in [57] as well. Because the stators described herein do not have an inherent nodal location along the edge, the boundary conditions are extremely important for creating an effective tether. The two important boundary conditions are seen from the modal simulation of a free ring, shown in Figure 4.7.

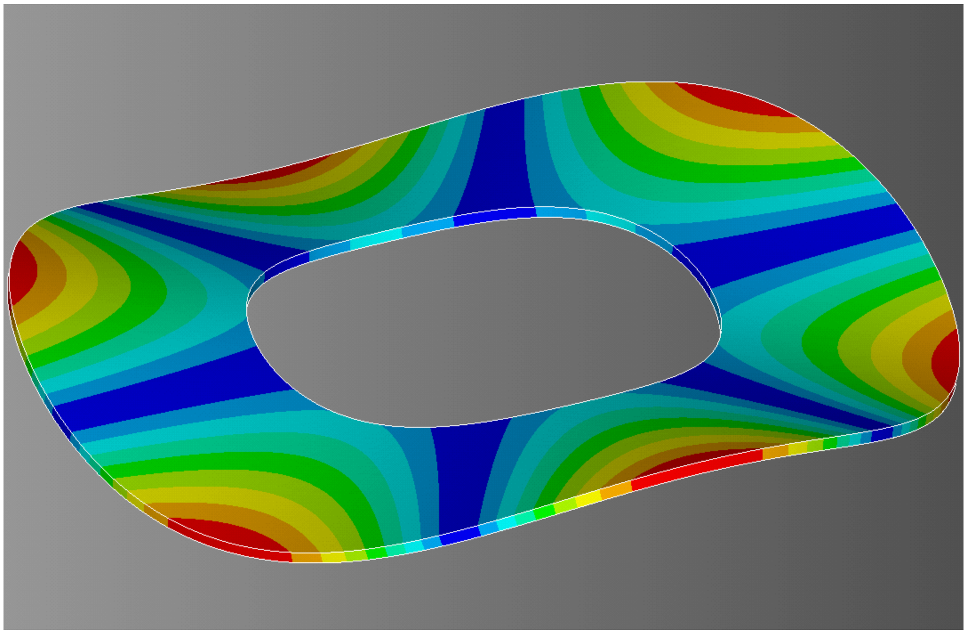

(a)

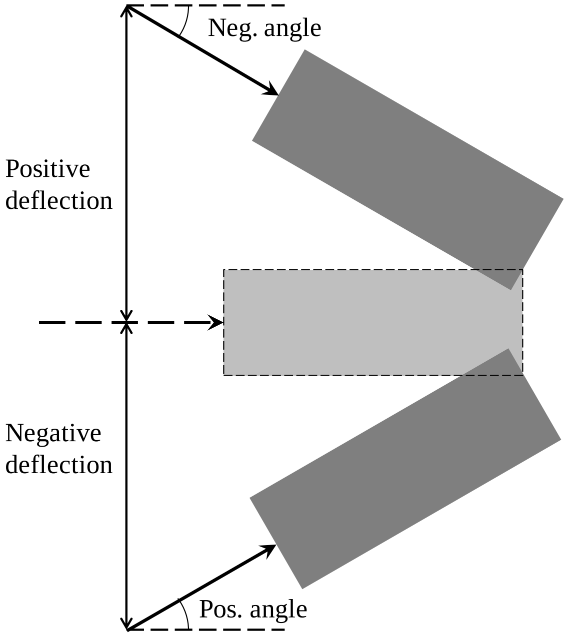

(b)

Figure 4.7. (a) Modal simulation of a free ring, and (b) a diagram showing the boundary conditions that must be satisfied for effective tethering.

From this diagram, it is clear that the tether must allow for no motion or angular deflection at the anchor point, and a positive displacement and a negative slope at the tether tip. This, in part, is why the straight tether, regardless of length, was so ineffective in reducing the tether effects. As shown in Figure 4.8, the straight tether's resonance mode produces a positive displacement with positive slope at the tether tip. Furthermore, the higher modes of the straight tether also display this type of deflection/slope pairing.

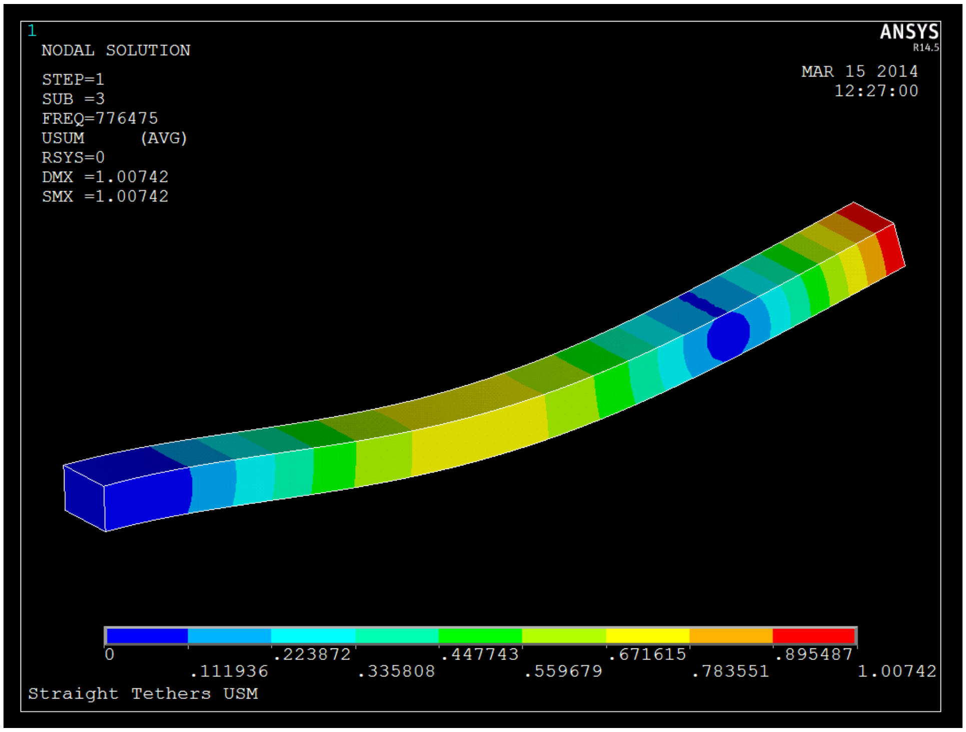

Figure 4.8. ANSYS simulation of the first matching mode of a straight tether, showing the deflection and slope mismatch.

This mismatch between the modes of the straight tether system and the boundary conditions of the stator system mean that the system mismatch must be resolved by distortion of the stator and tether systems, adding stiffness and changing the resulting mode shape and frequency. In order to prevent this boundary condition mismatch, various tether shapes were examined to determine favorable resonance mode shapes.

4.3.2.2 Interface Strain

A second consideration for the design of these tethers, considered as individual dynamic systems, is the role of energy loss through the tether. To determine an upper bound, it can be estimated that the strain energy at the tether/substrate interface is lost each cycle. This energy loss lowers the quality factor of the system, reducing the effectiveness of the stator for motor action.

In order to reduce the energy lost through the tether and maintain a high quality factor, designs were also examined for relative stress at the tether/substrate interface using finite element modal analysis. Since each mode shape is normalized to unity, the relative differences in the stresses experienced can be used to compare two designs. It can be seen, in Figure 4.9, that the straight tether not only results in incompatible boundary conditions, but also supports the maximum stress at the tether/substrate interface.

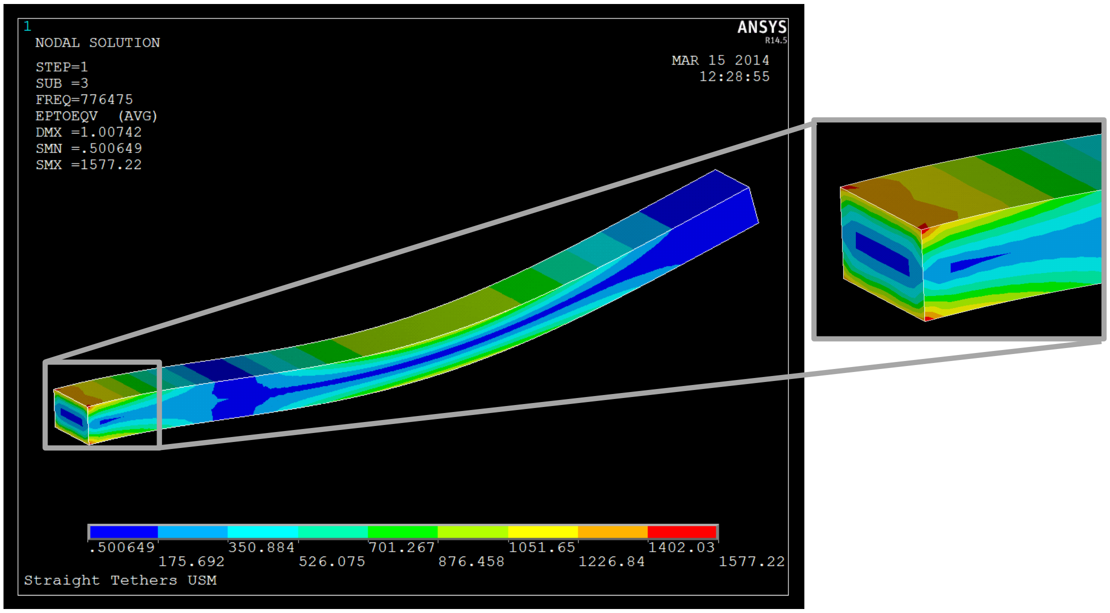

Figure 4.9. ANSYS simulation of a straight tether illustrating the large relative strain experienced at the attachment point, resulting in system energy lost to the substrate.

In contrast to the straight tether, the final design that was fabricated showed good boundary condition matching and relatively small strain at the tether/substrate interface. This design, from here on called a mechanical impedance transformer tether, is shown in a top-down view in Figure 4.10 (a), and simulated in Figure 4.10 (b).

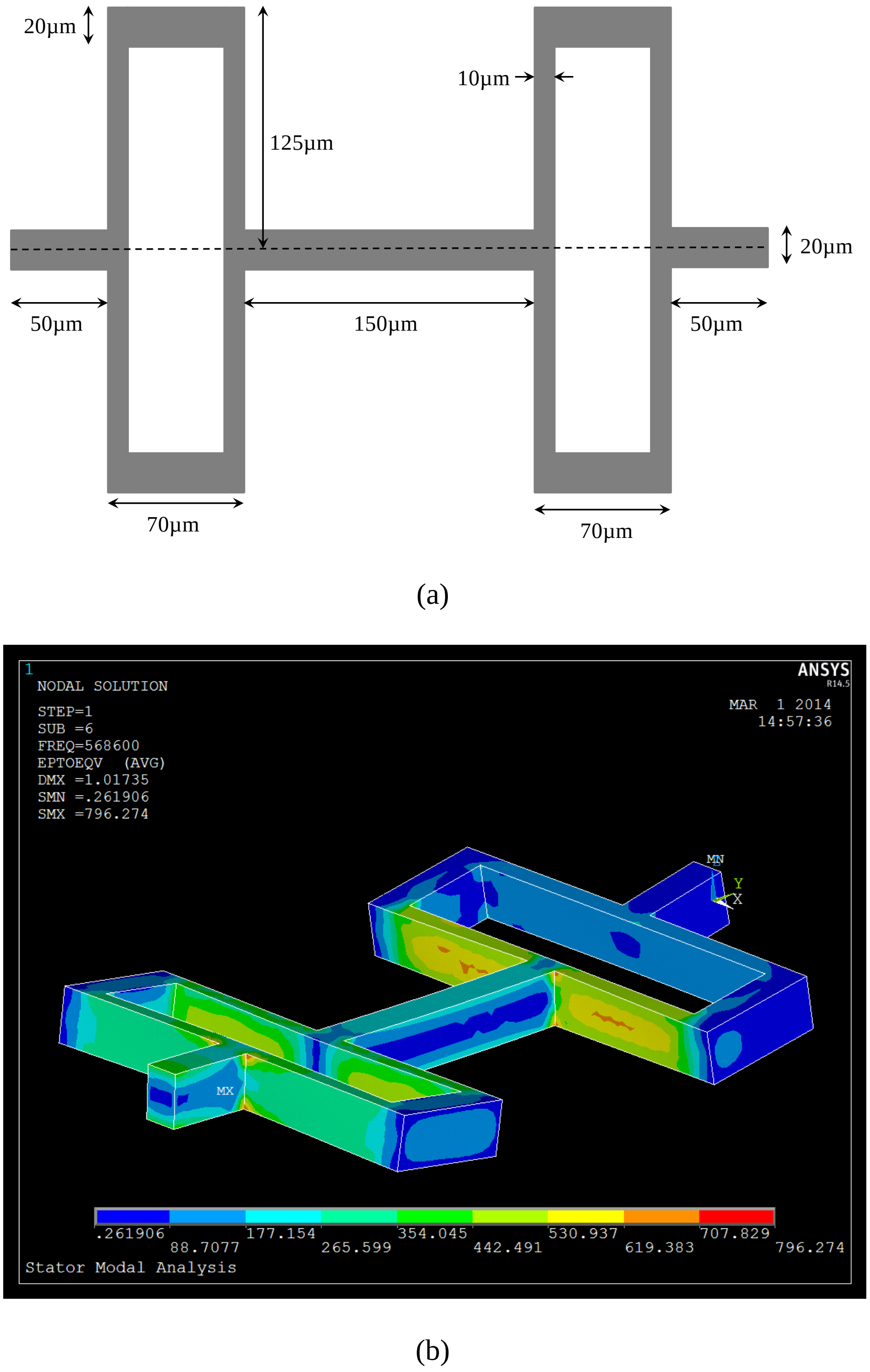

```
NODAL SOLUTION

STEP=1
SUB =6
FREQ=568600
EPTOEQV   (AVG)
DMX =1.01735
SMN =.261906
SMX =796.274

MAR  1 2014
14:57:36

.261906       177.154       354.045       530.937       707.829
       88.7077       265.599       442.491       619.383       796.274
Stator Modal Analysis
```

Figure 4.10. (a) A top down view of the selected design of the tether system. (b) A simulated modal response of the tether system, shown the relatively low strain at the interface and good boundary condition matching.

This mechanical impedance transformer tether design can be simplified by considering it as a collection of spring joints and rigid bodies. The boxes in Figure 4.10(a) act as torsional springs, with the slender beams in the y direction twisting to support rotation. The thicker beams act as rigid bodies, utilizing the angular twist in the joints to create net vertical motion. The two boxes are required to create matching boundary conditions for attachment. Since the slender beams in the boxes support most of the stress, there is relatively low stress at the tether/substrate interface, as shown in Figure 4.10(b).

4.3.2.3 Simulated improvement

With the description of the tether design complete, the results of combining the tether system with the stator system will now be described. It is helpful to outline again the drawbacks of tethered systems and the design goals for a tethered ring device. The drawbacks of tethered ring stators include: shifted resonance frequency, distorted mode shapes, and energy dissipation. The design goals of the tether system, matching boundary conditions and low energy loss, address the drawbacks just listed.

To begin, an ANSYS finite element modal simulation of a free ring stator displaying the targeted mode shape, B_{03}, is presented in Figure 4.11. An ideal tether will allow the ring component to achieve a similar mode shape with little distortion, while allowing the orthogonal mode shapes to occur at identical frequencies.

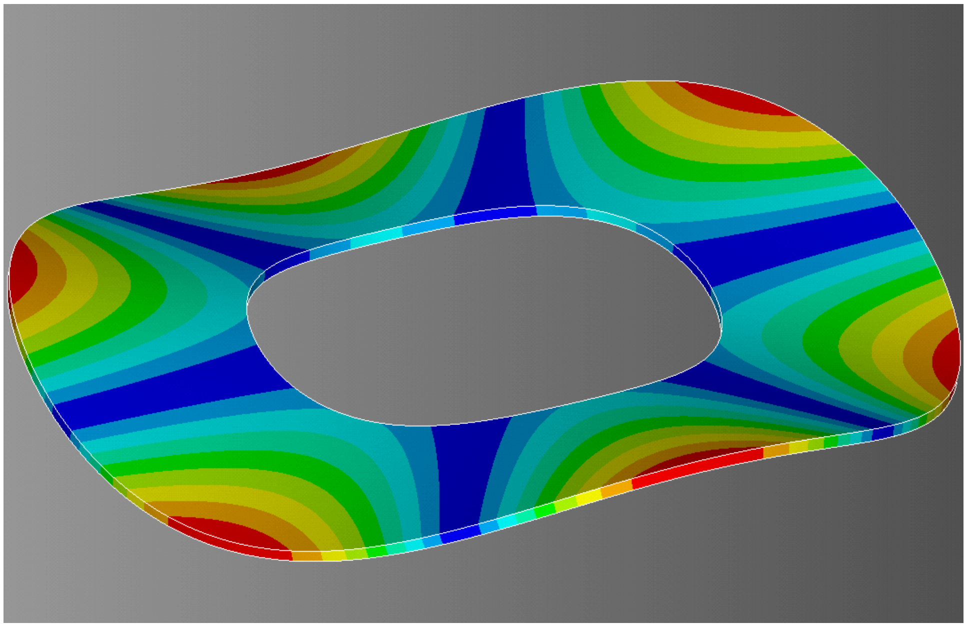

Figure 4.11. ANSYS modal simulation of a free ring stator showing the desired mode shape, B_{03}.

As a baseline, ANSYS modal analysis simulations were performed of a ring stator with 6 straight tethers to determine the effect these tethers have on system response. Modal displacements of the two orthogonal modes of the straight-tethered ring stator are shown in Figure 4.12. Figure 4.13 shows the relative strain, with a cut out showing the strain at the interface between tether and substrate. The simulation parameters and properties are listed in Table 4-1 for reference. The parts are simulated as pure silicon because the thick silicon dominates the response.

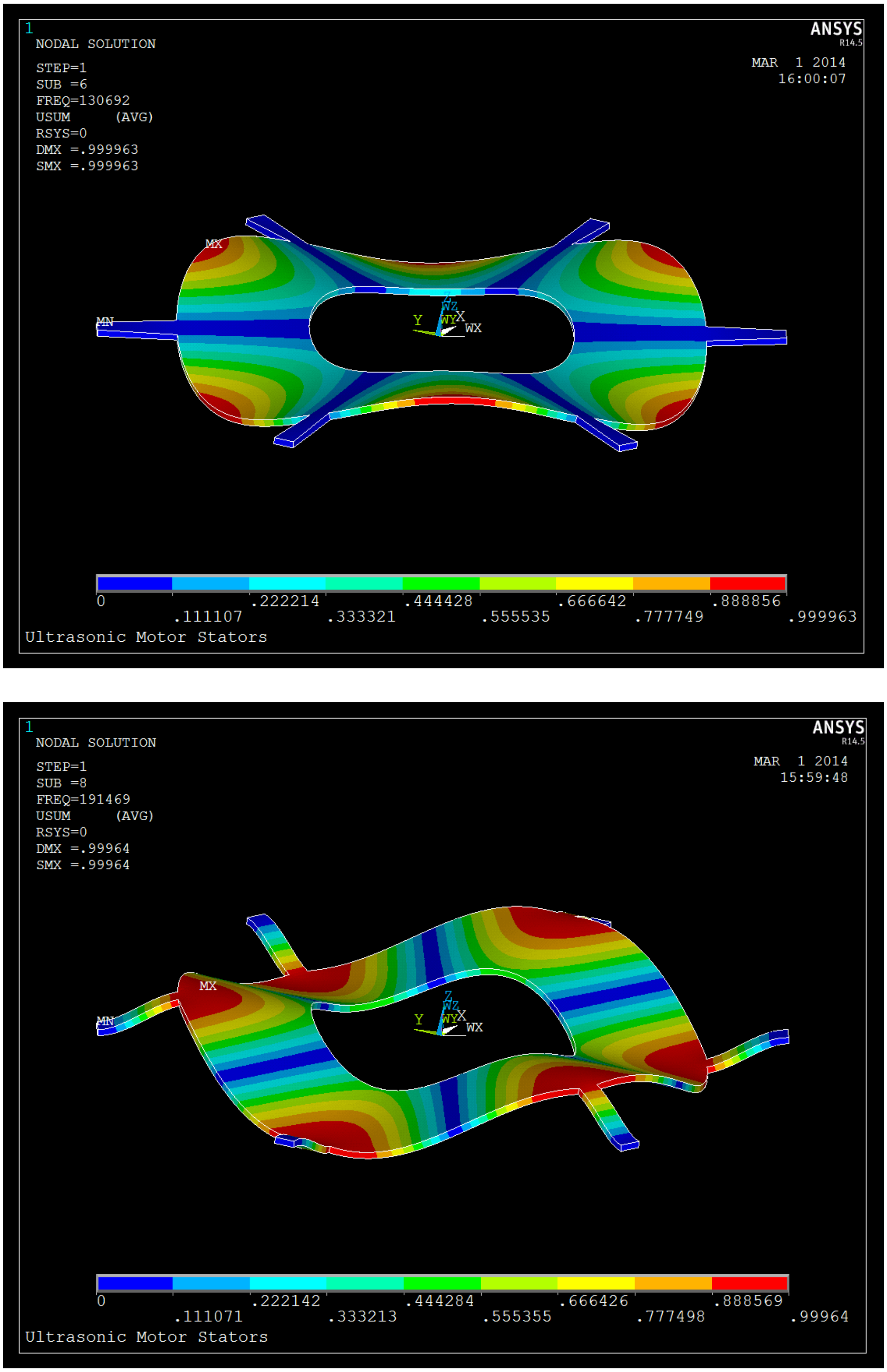

Figure 4.12. ANSYS simulation of two orthogonal B_{03} modes of a straight-tethered ring stator showing frequency mismatch and mode shape distortion.

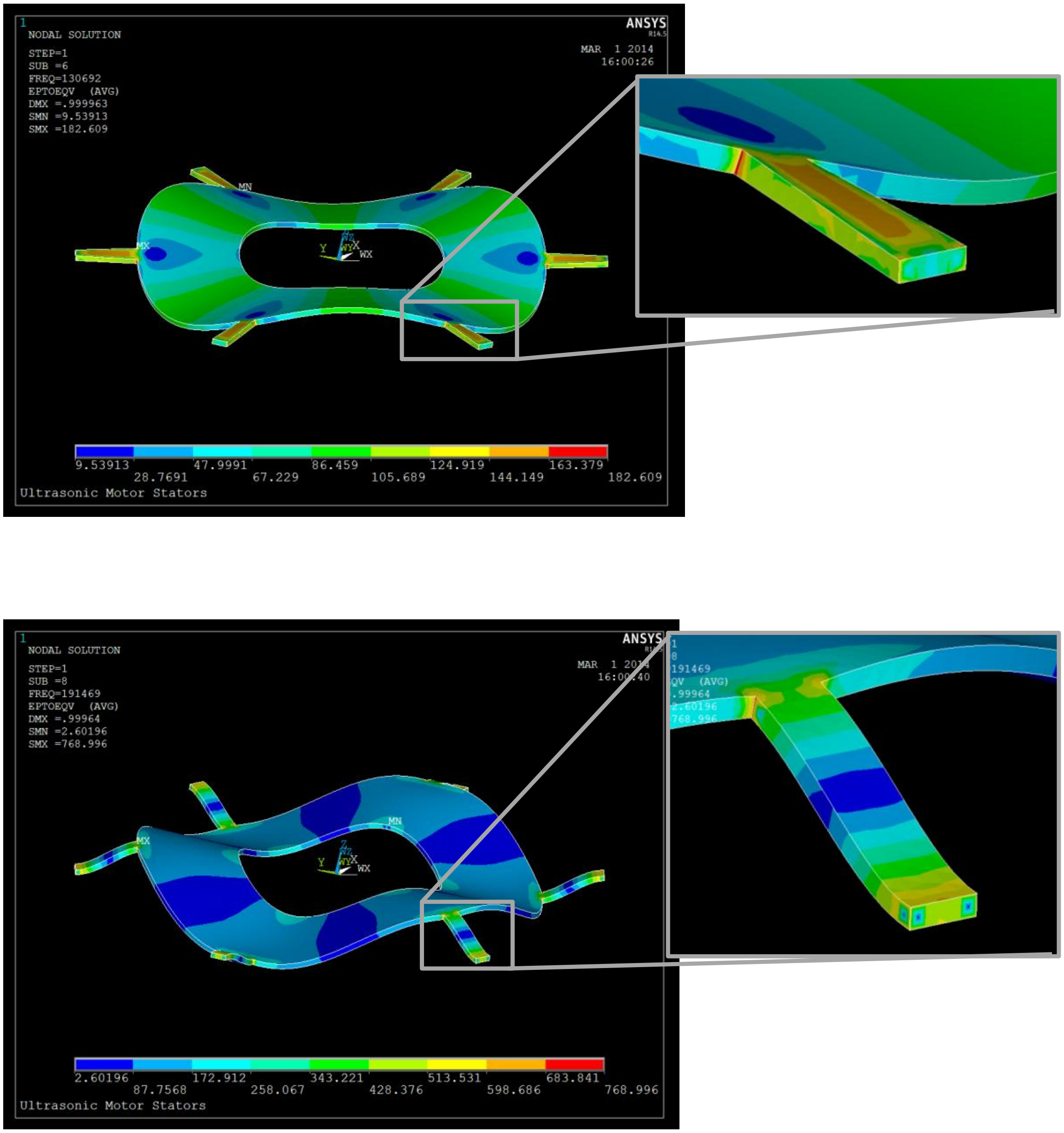

Figure 4.13. ANSYS simulation of two orthogonal B_{03} modes of a straight-tethered ring stator showing frequency mismatch, and relative strain at the interface.

Table 4-1. Simulation parameters used in ANSYS modal analysis of rings

Parameter	Value
Young’s Modulus	170 GPa [50]
Poisson’s Ratio	0.064 [50]
Density	2330 kg/m^3
Mesh Size	10 μm
Inner Diameter	1000 μm
Outer Diameter	2000 μm
Thickness	25 μm

From the simulation of the two orthogonal B_{03} modes of the ring stator tethered with a straight beam in Figure 4.12 and Figure 4.13. From this simulation, it can be observed that the frequency shift is approximately 32%, that the individual mode shapes are distorted, and that there is a significant strain developed at the substrate interface. In contrast to the straight tethered stator, the modal simulations of the stator with the mechanical impedance transformer tether design are presented in Figure 4.14 as modal displacement and in Figure 4.15 representing the relative strain.

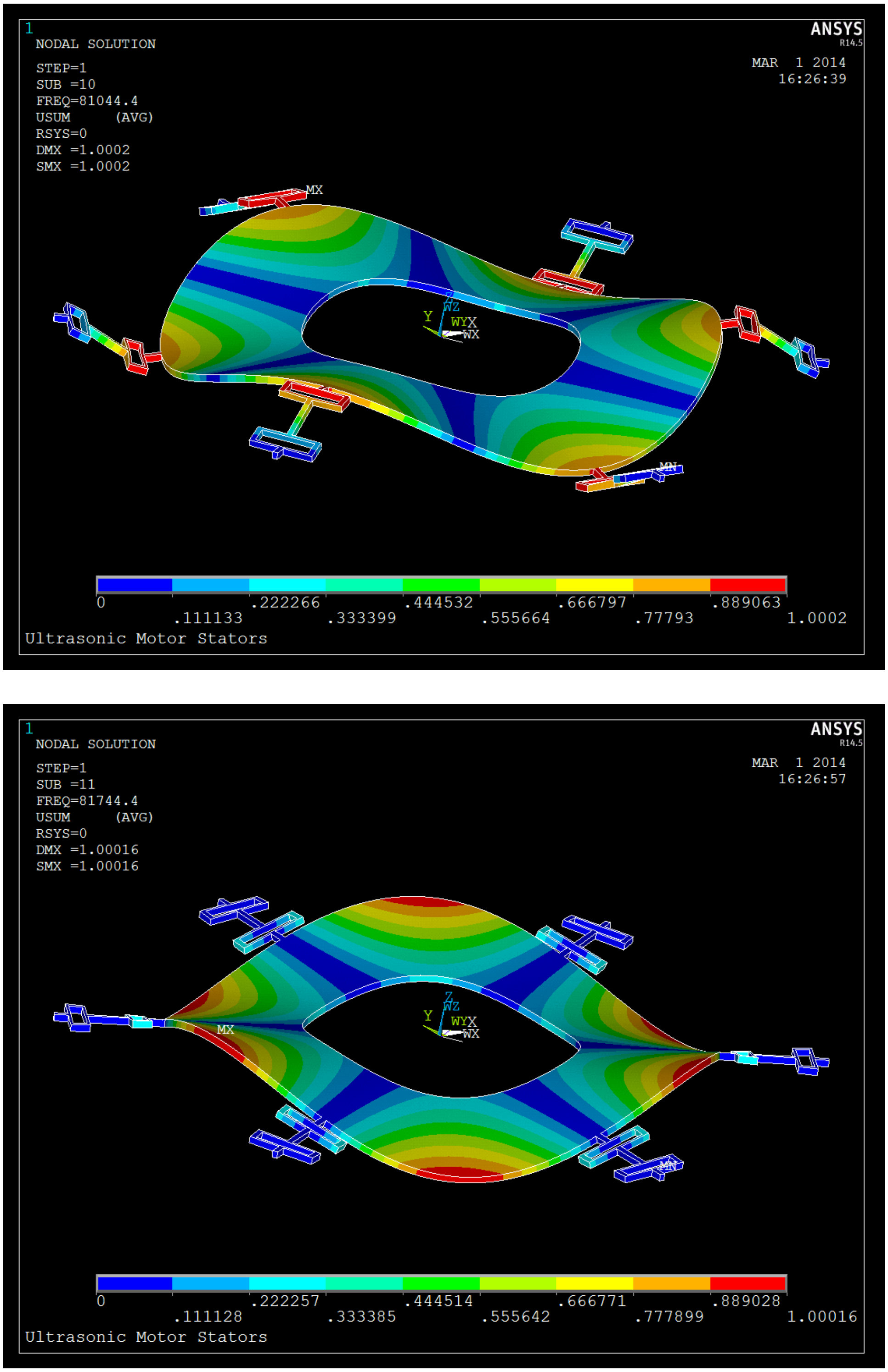

Figure 4.14. ANSYS simulation of two orthogonal B_{03} modes of a ring stator tethered with the mechanical impedance transformer tether showing lower frequency mismatch, mode shape distortion.

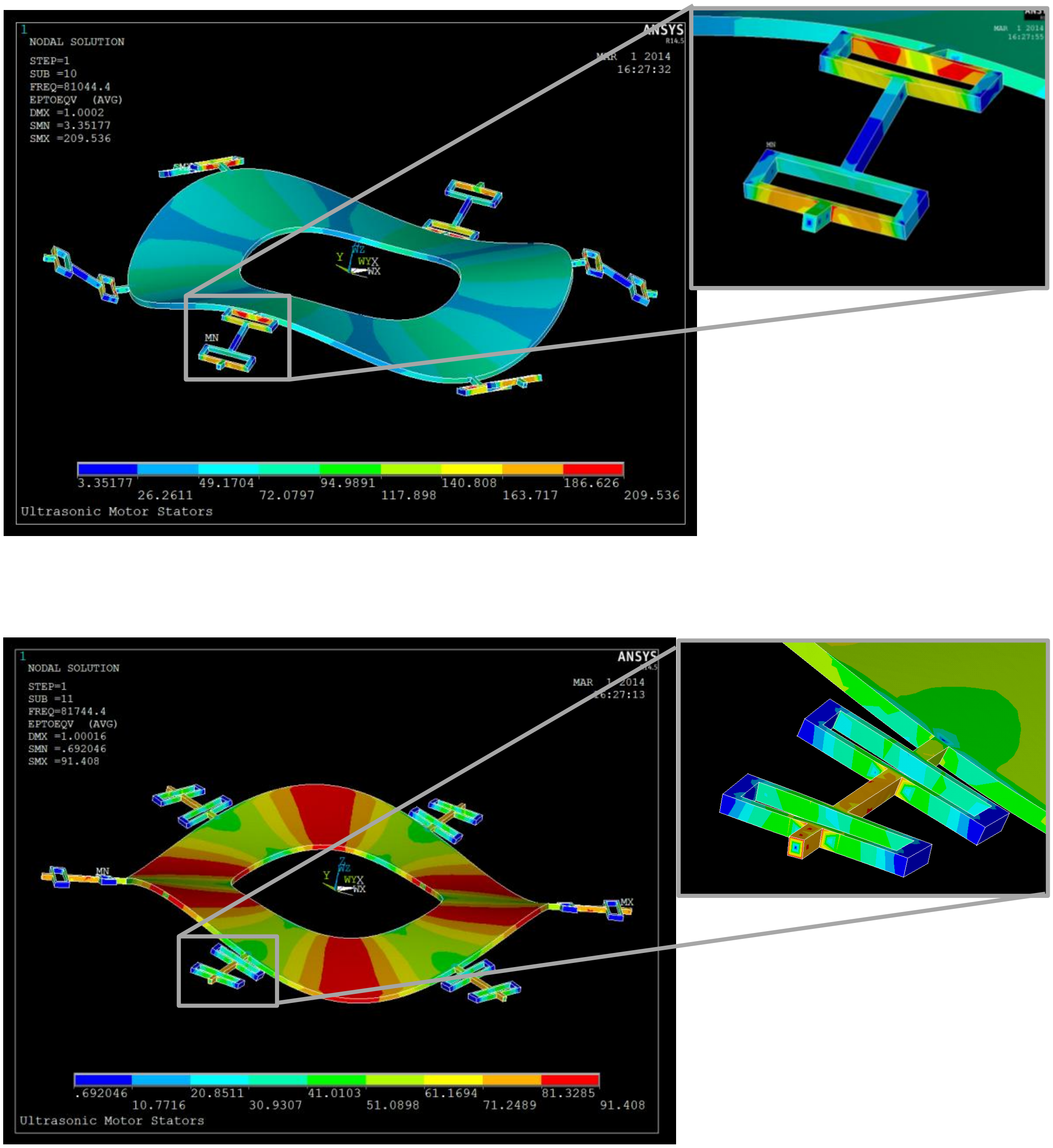

Figure 4.15. ANSYS simulations of two orthogonal B_{03} modes of a ring stator tethered with the mechanical impedance transformer tether illustrating lower frequency mismatch, and stress at the interface.

Figure 4.14 shows an improvement in frequency mismatch from 32% to 0.86%. The mode shapes are also qualitatively much less distorted, and stress at the interface is reduced, which allows for higher quality factors to be achieved. These improvements can be extended by altering the number of tethers in the system. When a stator with 3 nodal diameters has six equally spaced tethers, the orthogonal modes have either nodal lines aligned with the tethers or anti-nodes aligned with the tethers. This alignment exaggerates the tether effects because the modal responses of the tethers are characteristically different. By altering the number of tethers, this nodal line alignment is upset, resulting in the modes being ultimately symmetric. Figure 4.16 contains simulation results from a stator with four tethers, which is the lowest number of tethers to avoid nodal line alignment with tethers in a B_{03} mode. Figure 4.17 shows simulation results from a stator with twelve tethers, allowing the tether alignment to occur for both orthogonal modes. Changing the number of tethers reduces the simulated frequency offset to 7 ppm.

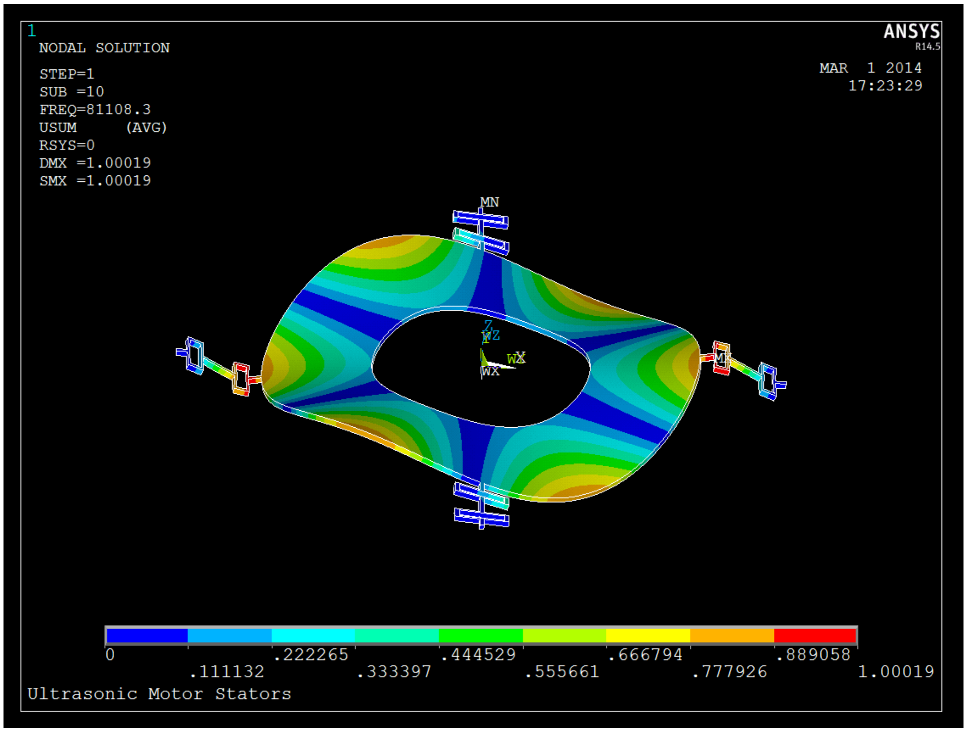

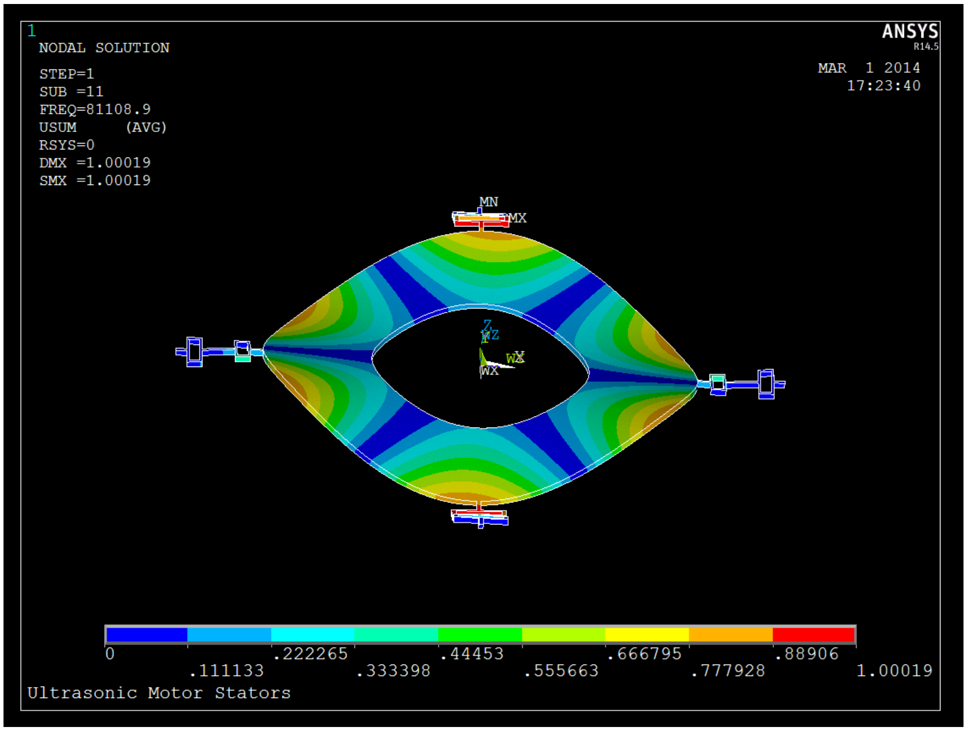

Figure 4.16. ANSYS simulations of the orthogonal B_{03} modes with symmetric responses due to nodal line alignment elimination with four tethers.

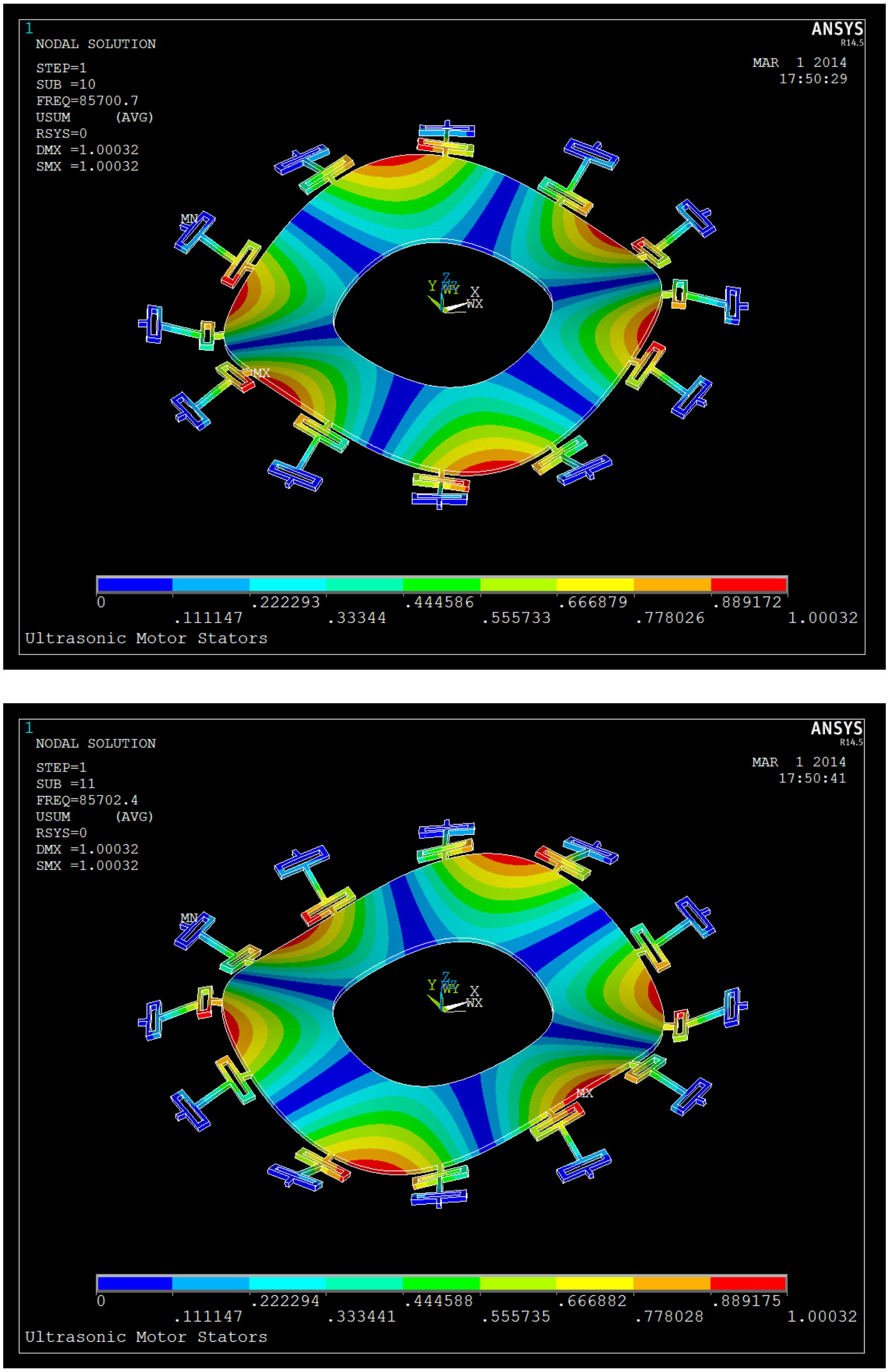

Figure 4.17. ANSYS simulations of orthogonal B_{03} modes with symmetric response due to the symmetric nodal line alignment from twelve tethers.

4.3.3 Characterization of standing waves

In order to experimentally demonstrate the improvement of the mechanical impedance transformer tether design, a set of edge tethered ring stators were fabricated, some with straight tethers and some with the mechanical impedance transformer tether design. Each tether design had the same total length and the same beam width. Stators had either 4 tethers or 12 tethers in order to exploit the nodal symmetry described in the previous section. Figure 4.18 shows a micrograph of a traveling wave ultrasonic ring stator 3 mm in diameter with the mechanical impedance transformer tether design.

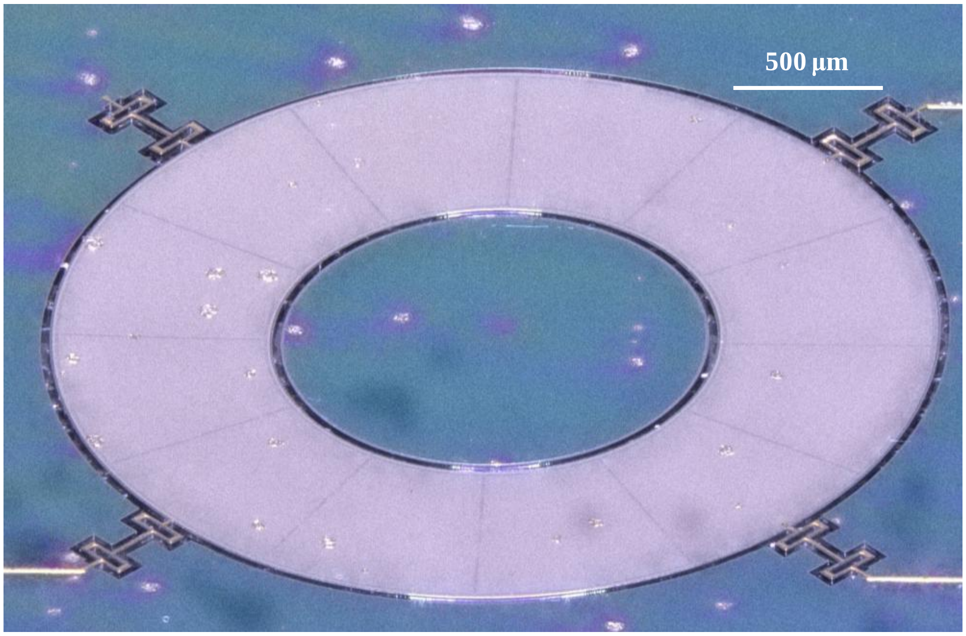

Figure 4.18. A micrograph of a 3mm diameter traveling wave ultrasonic ring stator with the mechanical impedance transformer tether designed to reduce undesirable effects such as mode distortion and frequency shift.

The standing wave deflection can be characterized as a function of frequency and applied voltage as was done with the disc stators. Individual measurements were made for each frequency and applied voltage using a laser Doppler vibrometer. Because nonlinear trends were a concern due to clamped-clamped tether boundary conditions, both sweep up and sweep down were recorded for each frequency and voltage. No nonlinear jumps were observed and sweep up/down plots generally match well. Figure 4.19 shows a plot of stator deflection in a straight tethered ring stator as a function of frequency for three applied voltages (0 V to -3 V, 0 V to -6 V, 0 V to -9 V).

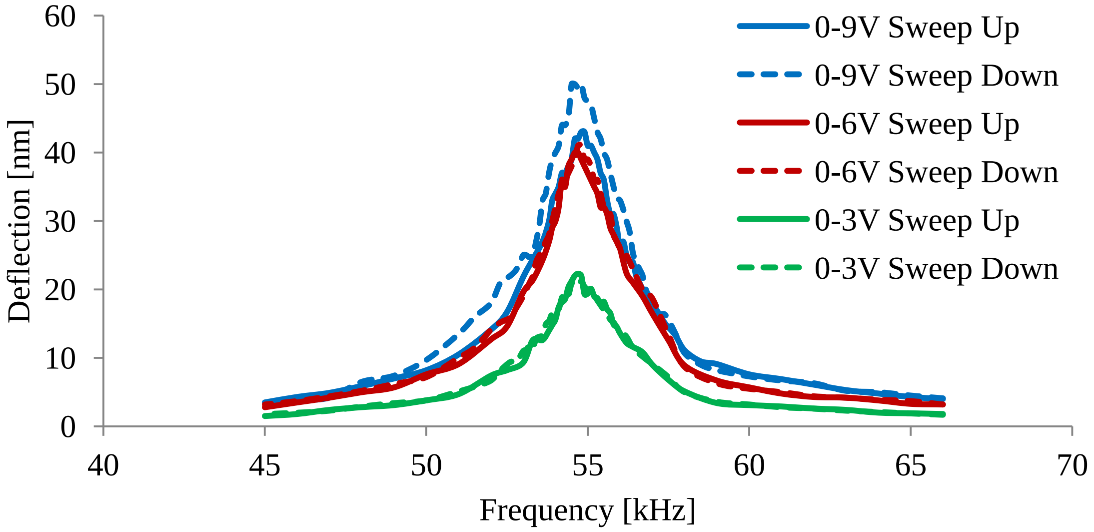

Figure 4.19. Maximum vertical deflection of an anti-node of the ring stator with straight tethers as a function of voltage and frequency.

Figure 4.19 shows a peak deflection of 50nm at $9V_{p\text{-}p}$, and a quality factor of 26. By contrast, Figure 4.20 shows out of plane deflection in a ring stator with the mechanical impedance transformer tether design, plotted as a function of frequency for the same three applied voltages (0 V to -3 V, 0 V to -6 V, 0 V to -9 V). From Figure 4.20 it can be observed that at 9 $V_{p\text{-}p}$, the peak deflection is 101 nm, over two times the deflection of the straight tethered device. A quality factor of 36 is also measured for the stator with the mechanical impedance transformer tether, a 40% improvement over the straight tether. Compared to disc devices, amplitudes and quality factors are lower, likely due to the edge tether, despite design improvements. Figure 4.21 shows a plot with the 9 $V_{p\text{-}p}$ sweep up plots for the two tether types, illustrating the improvement in standing waves generated in the same stator design with different tethers.

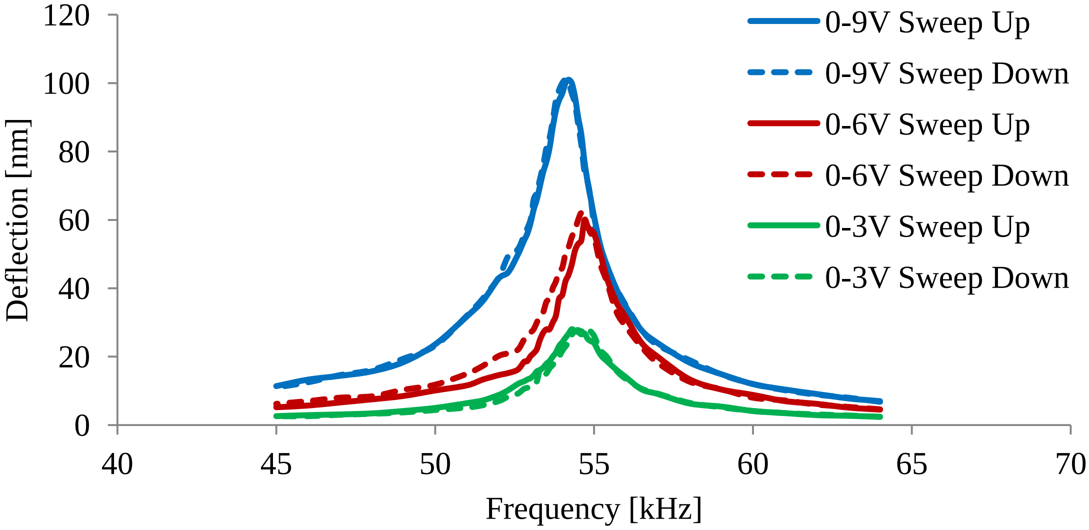

Figure 4.20. Maximum vertical deflection of an anti-node of the ring stator with the mechanical impedance transformer tether design as a function of voltage and frequency.

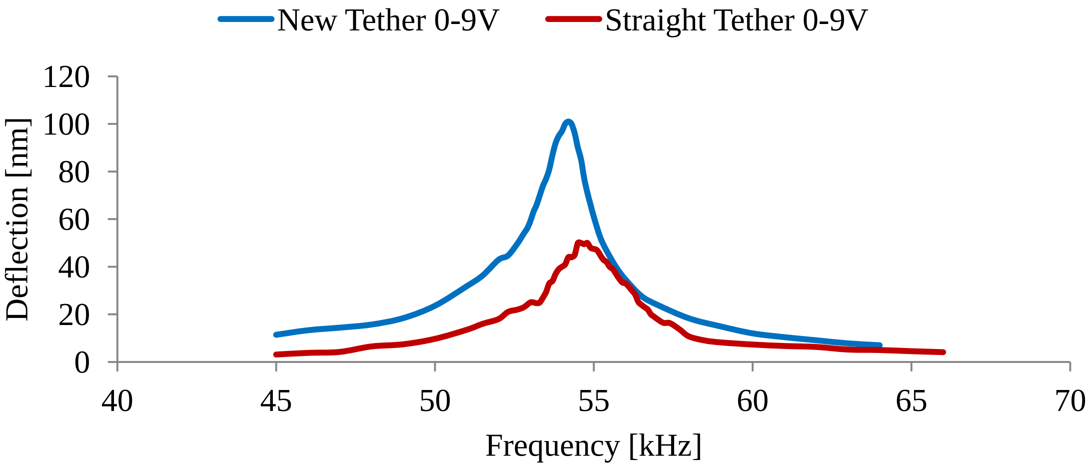

Figure 4.21. Maximum vertical deflection of anti-nodes of the ring stators under 9 $V_{p\text{-}p}$ excitation shows the improvement of the mechanical impedance transformer tether design over a straight tether.

As in disc motors, the initial step in creating a sustained traveling wave is to properly control the nodal line locations of the two orthogonal traveling waves. In a perfect disc motor, the nodal line location could be along any diameter of the disc, however small imperfections lead to a random preferential nodal line location. This random preferential location can be overcome by exciting the resonance mode with shaped electrodes, similar to electrode shaping in linear beams. The piezoelectric forcing, defined by electrode location, determines the nodal line locations, co-locating the anti-node with the center of the electrode.

As described in Section 4.2.3.1 and Figure 4.3, the orthogonal mode shapes in a straight tethered ring stator occurred at different frequencies because of distortion from the straight tether. This tether interaction not only distorted the modal frequencies, but it also fixed the location of the nodal diameters of standing waves. In the low frequency B_{03} mode, the nodal lines are aligned with the tethers, minimizing the tether interaction. In the high frequency B_{03} mode, the anti-nodes are aligned with the tethers, resulting in the maximum distortion from the tethers. In this sample device, the standing wave anti-node aligned to the tether location, rather than the electrode location, indicating that the tether contribution is strong enough to overcome the preferential orientation due to piezoelectric forcing.

A similar test has been performed with the mechanical impedance transformer tether design. Figure 4.22 shows that the anti-nodes are preferentially located at the active electrode. This control of nodal line location by design and actuation input allow for a controlled traveling wave to be generated in these tethered ring devices.

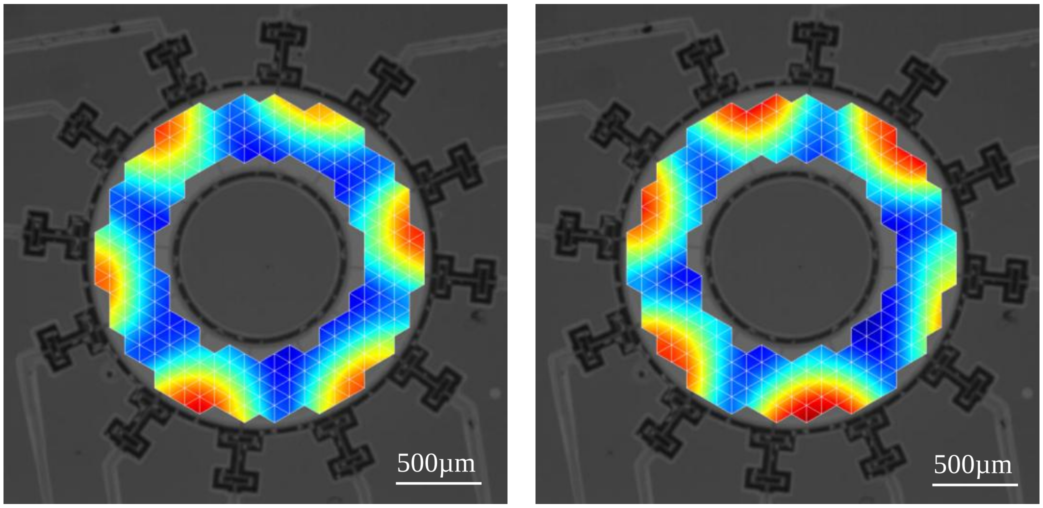

Figure 4.22. Experimental LDV data shows the anti-node, shown in red, preferentially locates to the active electrode, allowing for the controlled generation of orthogonal B_{03} standing waves in the ring stator.

4.3.4 Demonstration of ring traveling wave

With control of the standing waves demonstrated, these standing waves can be combined out of phase 90° and apart in space by a quarter-wavelength to create a traveling wave. Figure 4.23 shows a series of phase-stepped images simulating 7.1 μs and 120° of wave propagation about the ring.

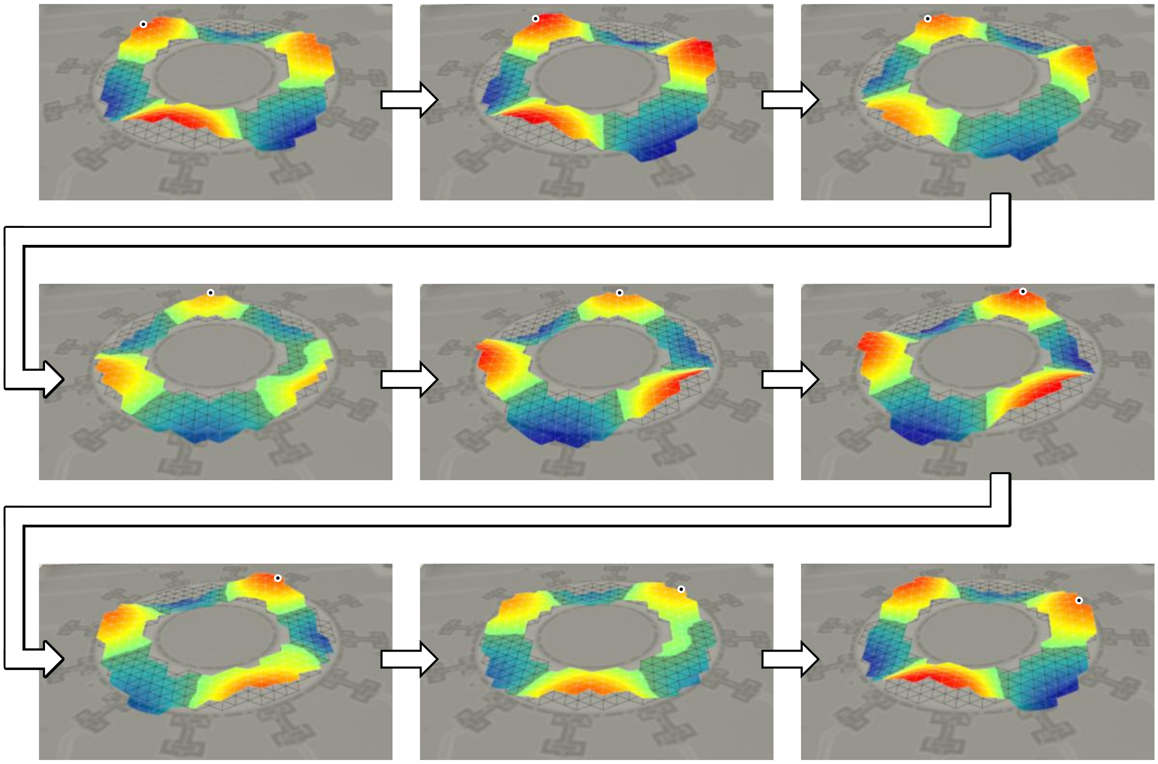

Figure 4.23. Phase-stepped images corresponding to 7.1 μs and 120° of wave travel around the ring. The black dot with white circle tracks the wave peak as it propagates.

4.4 Summary

This chapter highlights the work performed to address the design challenges of ring tethered traveling wave ultrasonic motors. Such devices are attractive due to their potential for easier system integration. Tethering devices from the edge allows electrical routing to be performed on the wafer surface, eliminating the wirebond that extends through the rotor to the center of the ultrasonic disc stator. This process of tether the ring stator to the substrate introduces new challenges. Mode distortion, frequency shift, and quality factor reduction are each highlighted throughout. By treating the tether as its own separate dynamic system, a mechanical impedance transformer tether was designed using finite element analysis and boundary condition analysis which reduces frequency shift, increases quality factor and allows increased out of plane amplitude. The standing waves of these ring stators were characterized and a traveling wave was excited in a tethered ring device. These results are summarized in Table 4-2.

Table 4-2. Summary of ring stator geometry and performance specifications

Parameter	Value
Stator diameter	1 - 3 mm
Stator thickness	25 µm
Actuation frequency	50 - 140 kHz
Simulated modal frequency offset	32% → 7ppm
Measured quality factor enhancement	40%

5 Motor Design, Modeling, and Characterization

With discussion of the traveling wave stators complete, this final section describes the design, modeling, and characterizing of prototype small-scale traveling wave ultrasonic motors (TWUM). Following a short discussion of the motor design and components, a fundamental model is described, and motor characterization results are presented. Some of this work was presented in [58].

5.1 Design

The first task in describing and characterizing the motor is defining the design space and design requirements. In its simplest form, a TWUM consists of two components, a stator and rotor, as described in Section 1.1. The stator is a stationary component that supports a traveling wave, which frictionally propels a freely moving rotor. The rotor can be a linear translation element or a rotary component. In this case, the focus of this work is rotary TWUM.

As described in Section 1.1, the TWUM operates by exploiting the lateral frictional forces arising from the physical contact between the stator and rotor. In macro-scale motors, wear due to this constant frictional contact has been well documented. In recent years, frictional coatings have been incorporated to increase torque and reduce wear, such that motors have been operated continuously for hundreds of millions of revolutions with no performance degradation [1]. Such protective layers are more difficult to incorporate into small motors integrated on a wafer scale, because such integration would require selective deposition or patterning and would also require that the material not affect or be affected by subsequent process steps.

The rotor must also be confined, preventing both lateral and vertical translational motion. This confinement is often accomplished at the macro-scale by incorporating off-the-shelf bearings into the design. Such commercial bearings do not exist at the micro-scale, although recent research in the area has shown promising results [56]. A further use of bearings is to provide a low-friction vertical load. Because the lateral frictional forces between the stator and the rotor are directly related to the normal forces, such vertical loadings increase motor torque and performance. The bearing provides the unique benefit of applying this vertical load without frictionally loading the rotor. Without bearings, any applied static load creates drag on the rotor, reducing the performance benefit of additional vertical load. Such complicated pre-loading structures are extremely difficult to create using microfabrication techniques and are beyond the scope of this work. Some potential solutions are described and discussed along with other future work in Section 6.2.5.

5.1.1 Silicon DRIE rotor

In order to create a proof-of-concept system, a prototype TWUM was created using a silicon rotor fabricated using through-wafer deep reactive ion etching. This proof-of-concept motor is shown in Figure 5.1.

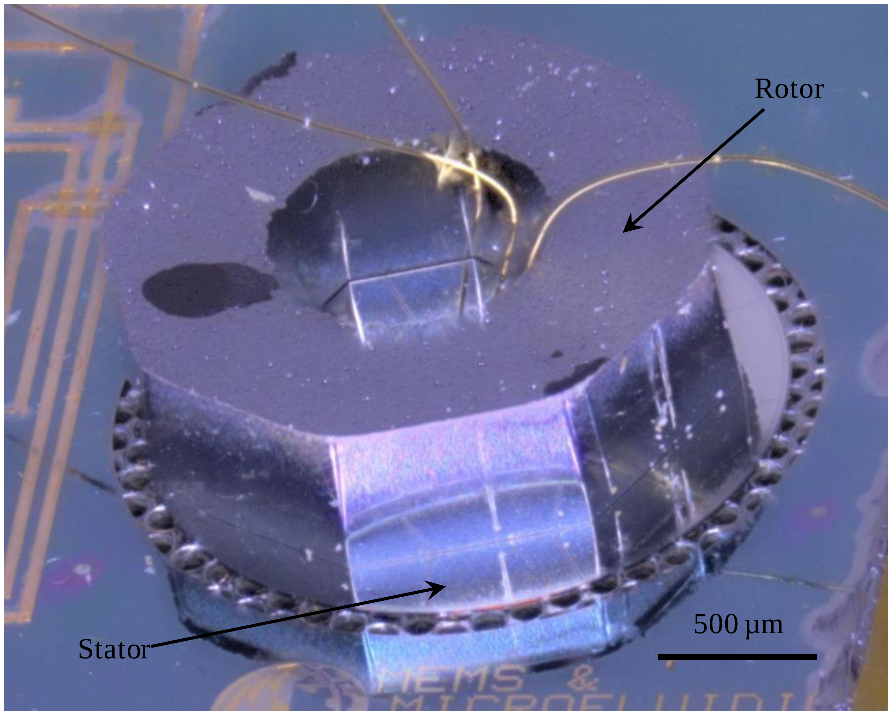

Figure 5.1. Micrograph of the proof-of-concept TWUM system with a silicon rotor.

In this prototype, stator teeth are omitted and wire bonds to the center are used to make electrical connection and also to confine the rotor laterally. The individual rotor is manually positioned before wirebonding to allow the bond wires to extend through the center hole in the silicon rotor. This silicon rotor TWUM was then used to characterize motor performance over a variety of conditions.

5.2 Modeling

In order to describe motor performance and characterization, it is first necessary to highlight the expected or modeled characteristics. While numerous techniques exist for determining motor performance, the fundamental model is well described in [13]. In this model, the contact between the stator and rotor is modeled and the resulting friction forces determine torque, while the speed of the stator and the stick/slip regions of the rotor determine rotor speed.

5.2.1 Model Formulation

This section will outline the model presented in [13]. This model is used here with no changes or modifications from the published model in [13]. Some of the underlying advantages and limitations of the model will also be discussed.

5.2.1.1 Stator Motion

As described in Section 1.1, the excitation of a traveling wave produces motion at the surface of the stator. The peak vertical motion can be characterized by laser Doppler vibrometry. This peak vertical motion is an essential piece in determining motor performance because it can be used to obtain the elliptical motion at the surface of the stator as shown in Figure 5.2.

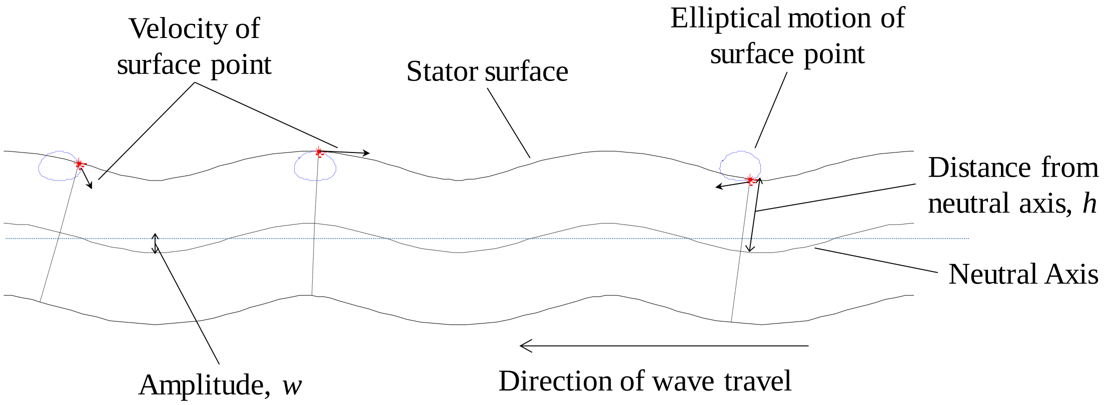

Figure 5.2. Schematic illustration of the stator deflection and elliptical motion with relevant variables highlighted.

In Figure 5.2, the elliptical motion of the surface of the stator is traced in a blue dashed line. This motion creates a local horizontal velocity near the crests of the traveling wave. To determine the elliptical motion at the surface, it is necessary to examine the traveling wave equation, Equation 5.1:

$$z = w\cos(k\theta - \omega t) \tag{5.1}$$

In this equation, z is the vertical deflection of the neutral axis, w is the wave amplitude, k is the wave number, θ is the angular position, ω is the excitation frequency, and t is time. This equation describes the motion of the neutral axis of the traveling wave, however the geometric and elastic properties of the stator transform this relationship into elliptical motion at the stator surface. A small angle assumption can be made since the length scales are much longer than the deflections in question. With this assumption, the vertical deflection approximately matches the wave shape:

$$\xi = w\cos(kx - \omega t) \tag{5.2}$$

Equation 5.2 approximately expresses the vertical motion of the stator surface, ξ. The horizontal motion of the stator surface, ζ, is then described by Equation 5.3.

$$\zeta = -whk\sin(kx - \omega t) \tag{5.3}$$

Here, *h* represents the distance between the surface point and the neutral axis. The horizontal speed of the stator surface, v_h, which is the motion tangential to the rotor, is the time derivative of the horizontal position.

$$v_h = \frac{d}{dt}\zeta = -w\omega hk\cos(kx - \omega t) \tag{5.4}$$

From Equation 5.4, it can be seen that the peak horizontal velocity can be expressed as in Equation 5.5.

$$v_{h_{max}} = -w\omega hk \tag{5.5}$$

It is also important to note that this peak horizontal speed also occurs at the peak vertical deflection, such that the crests of the traveling wave carry the largest tangential speed.

5.2.1.2 Rotor Motion

In the simplest formulation, this peak stator speed corresponds directly to the maximum rotor speed, or $\omega_{\text{rotor,max,}}$ through Equation 5.6, where *r* is the contact radius.

$$\omega_{rotor_{max}} = \frac{v_{h_{max}}}{r} = \frac{-w\omega hk}{r} \tag{5.6}$$

This occurs when the speed of the rotor matches the horizontal speed of the stator at the crest of the wave. This, however, is a limited case. In normal operation, there is small penetration of the stator into the rotor. This results in a variation of stator surface speed in the contact region. This speed range is resolved by introducing slip regions as shown in Figure 5.3.

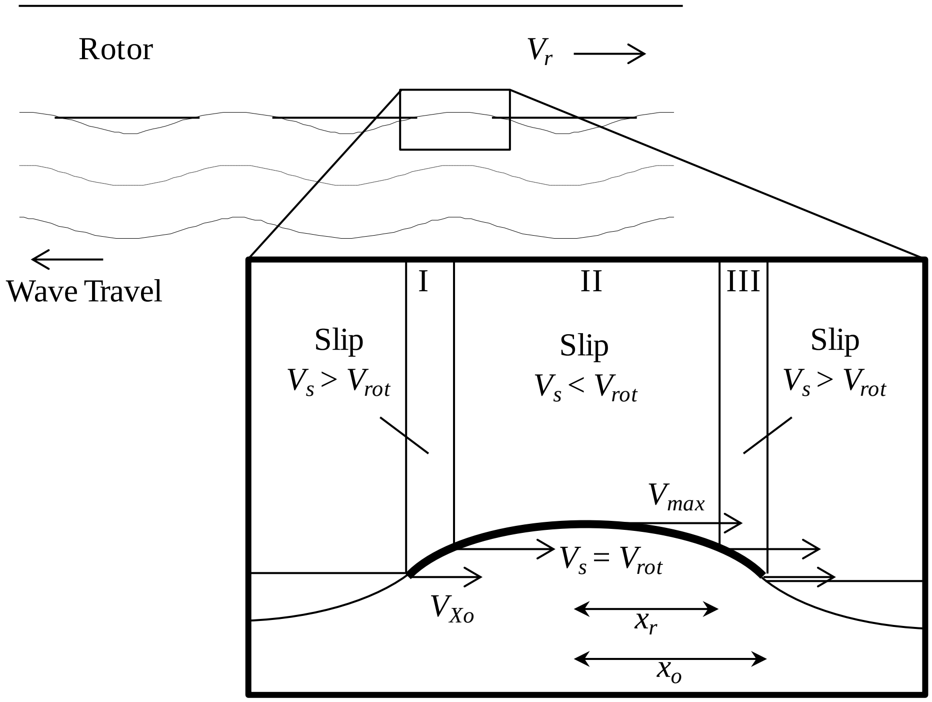

Figure 5.3. Illustration of the slip regions in the stator with relevant variables highlighted outline the torque and speed formulation for the motor model.

Figure 5.3 shows the regions of slip within the contact region between the stator and rotor. There are three distinct slip regions each separated by a point where the rotor speed matches the horizontal speed of the stator. In the outer slip regions (regions I and III), the rotor speed is higher than the horizontal speed of the stator surface. This speed difference causes a drag on the rotor. In the center slip region, region II, the tangential speed of the stator surface is higher than the rotor speed. The slip within this region, therefore acts to provide torque to the rotor. Combining the drag from regions I and III, with the force provided by region II, the net torque from the stator to the rotor can be expressed according to Equation 5.7.

$$\tau_{net} = 2r_{cont}\mu A \int_0^{x_r}[cos(kx) - cos(kx_0)]dx - 2r_{cont}\mu A \int_{x_r}^{x_0}[cos(kx) - cos(kx_0)]dx \tag{5.7}$$

Here, $= \frac{F_N k}{2[\sin(\mathrm{kx_0}) - \mathrm{kx_0}\cos(\mathrm{kx_0})]}$, r_{cont} is the radius of stator-rotor contact, and μ is the coefficient of friction. The normal force, F_N, geometric parameters, and material properties determine the value of x_0, whereas the rotor speed determines the location of since this point lies where stator speed and rotor speed match. With these two quantities, F_N and x_r, the net torque transmitted to the rotor can be determined. With this formulation, a torque speed curve can be developed for a given normal force (see Section 5.2.2.

5.2.1.3 Contact

In order to determine how normal forces relate to stator-rotor penetration, a contact model must be used. Flynn uses a Hertzian contact model that is proposed to be a good model for the given system [13]. In this model, the stator-rotor interface is modeled as a cylinder contacting an elastic halfspace. Under this formulation, the location of the contact point, x_0, can be determined from Equation 5.8, with R and C_E determined from Equation 5.9 and Equation 5.10 respectively.

$$x_0 = 0.8\sqrt{2F_N R C_E} \tag{5.8}$$

$$R = \frac{\lambda}{4\pi^2 w_0} \tag{5.9}$$

$$C_E = \frac{1-\nu_s{}^2}{E_s} + \frac{1-\nu_r{}^2}{E_r} \tag{5.10}$$

In these equations, F_N is the normal force, R is the radius of curvature, C_E accounts for material properties, λ is the wave length, w_0 is the peak deflection of the stator at the contact location, ν_s, ν_r, E_s, and E_r are the Poisson ratios and elastic moduli in the contact area of the stator and rotor respectively.

5.2.2 Model Conclusions

The model presented here is a simple representation of the operation of a TWUM. The model has been proven to sufficiently describe the performance and operation of TWUM as described in [13]. This model will be used to compare the expected and measured speeds with no applied load. Figure 5.4 shows the modeled results for a three millimeter diameter motor under various applied normal loads. The 18 µN load is approximately the preload due to weight of the rotor in the experimental system. From here it can be observed that increasing normal load has a direct effect on the maximum torque. Under reasonable normal loads less than 1 mN, the motor model suggest that torques up to 0.2 N·mm can be generated. In this platform, 0.2 N·mm torque would represent a torque density of 64 mN·mm / mm^3, an order of magnitude larger than the bulk PZT motor reported in [26]. If the power consumption is unaffected by preload, then peak efficiency would be approximately 28%.

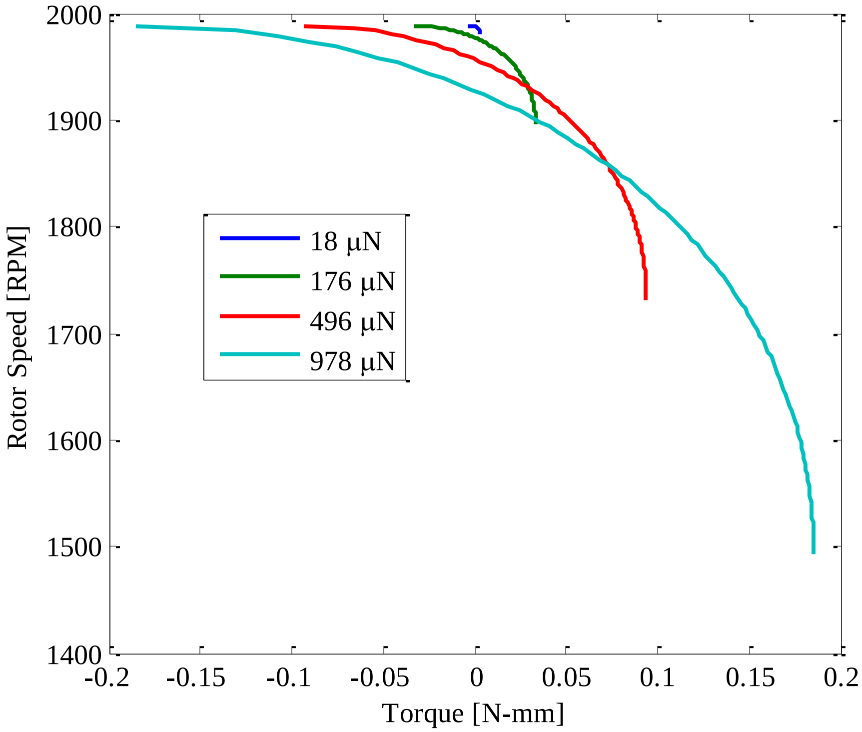

Figure 5.4. Modeled torque-speed curve for the 3 mm diameter thin-film TWUM described below. This shows the potential for increased torque with larger normal forces.

This model is excellent for its simplicity and transparency. It also sufficiently describes the steady state behavior of the motors without extensive fit parameters. The major disadvantage of this model is that known stator deflection is essential in determining motor performance, both in speed and contact area. This deflection, though measurable, cannot be easily determined a priori. This drawback results in a model that is predictive for the motor performance, but cannot be used to improve the design of the stator component. This limitation is described further in Section 6.2.4.

5.3 Characterization

This section is focused on the characterization of the prototype TWUM described above. The results include torque, speed, and power consumption as a function of phase, frequency, and actuation voltage. A motor with a 3 mm diameter stator and a motor with a 2 mm diameter stator were characterized. Each motor used a rotor with an outer diameter of 2 mm. Motion was characterized using a Keyence VW-9000 high speed microscope. To determine motor characteristics, individual frames of the high speed video were analyzed. In each frame the angular position of the rotor was determined by measuring the angle formed by two points opposite each other on the rotor. These angles were then tracked for the frames as time progressed. Instantaneous speed was approximately determined by dividing the change in angle over time.

A proof of concept motor with a stator 3 mm in diameter and 30 μm thick was used to characterize the motor speed behavior. In this stator, the B_{13} resonance mode occurs at 252.2 kHz. The 500 μm thick silicon rotor is made using deep reactive ion etching. The rotor is manually positioned on the stator and the assembled motor is wirebonded to a 24-pin dual in-line package (DIP). Two 252.2 kHz electrical signals 0-Vp, where Vp is the peak actuation voltage, are delivered to the device, offset by 90° in phase. Figure 5.5 shows the speed and power consumption as a function peak actuation voltage as reported in [58].

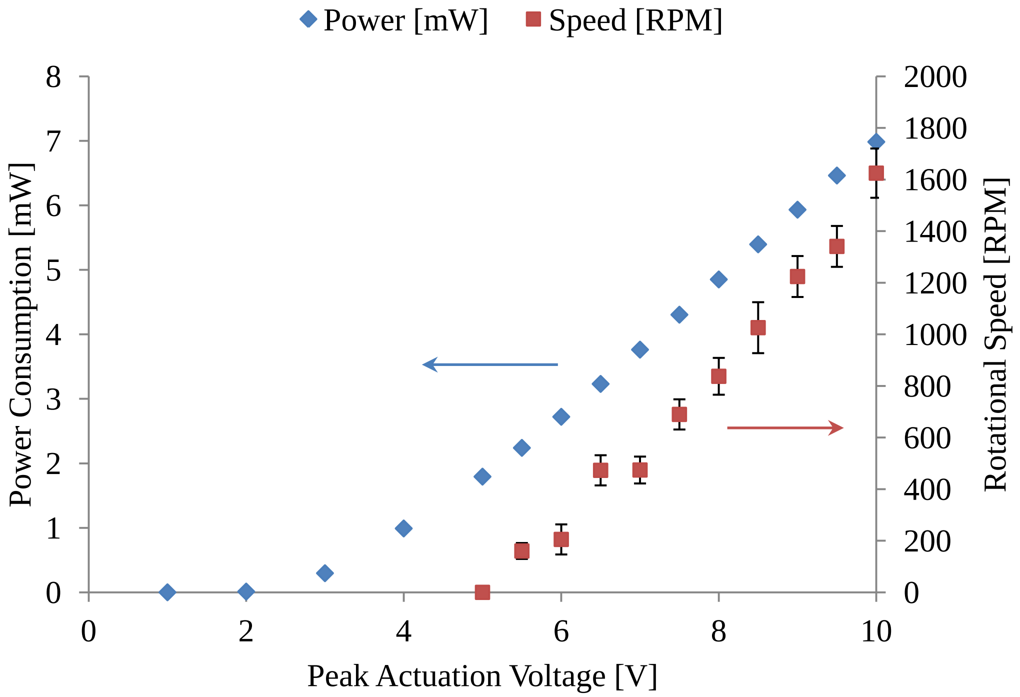

Figure 5.5. Experimental results show speed and power as a function of actuation voltage. Error bars on rotational speed represent standard deviation [58].

Observations from other PZT based MEMS devices fabricated at the US Army Research Laboratory [36] highlighted a degree of polarity bias, or imprint, in the piezoelectric response of the final devices. The imprint creates a preferred bias operation for the device such that one polarity bias can create larger strains than the opposite polarity [59]. For TWUMs, a negative bias applied to the top Pt electrode results in a larger strain generation, creating larger out-of-plane deflections. As a result, the increased out-of-plane deflection in the stator increases the speed of operation at a given voltage and also decreases the required starting voltage of the motor. Speed and power consumption as a function of voltage for the proof-of-concept motor is plotted in Figure 5.6, showing the smaller starting voltage and higher speeds under a negative bias voltage.

Additionally, Figure 5.6 shows that input voltage can be used to control motor speed. These speeds match well with the predicted no-load speeds from the motor model.

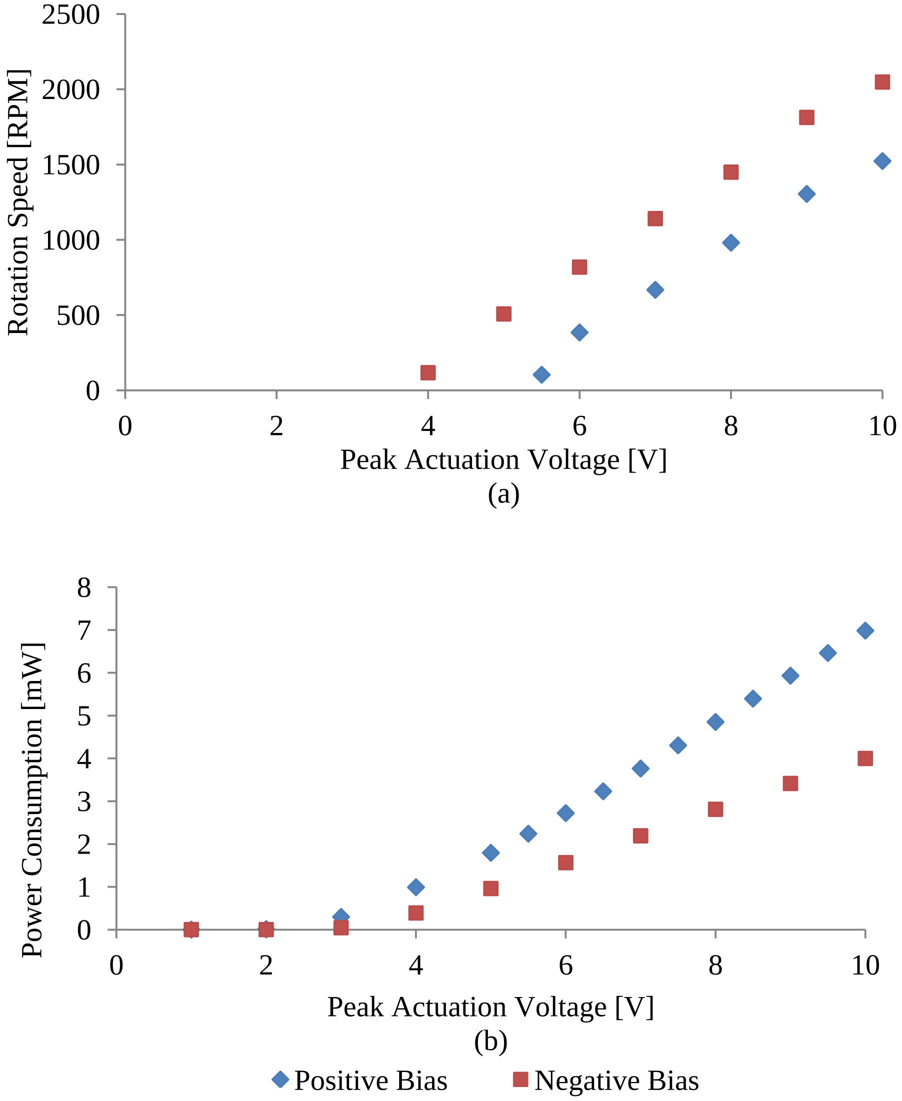

Figure 5.6. (a) Rotation speeds as a function of peak actuation voltage for positive and negative bias shows that higher speeds and lower starting voltages can be obtained by operating with negative bias. (b) Power consumption under negative bias is lower than under positive bias and trends linear above 5V.

Characterization of motor speed as a function of phase was also performed and is shown in Figure 5.7. Phase control has been used in macro-scale TWUMs to allow for a slow start and stop, although this is accomplished at a lower efficiency [60]. Additionally, rotation direction can be controlled by changing the phase by 180°. This ability to change rotation direction with changing phase is a main advantage of traveling wave motors over standing wave motors. One interesting note is that the zero speed crossing occurs at a non-zero phase, and by extension the rotor moves when the phase offset between the two excitation signals is zero. Furthermore, the rotor moves when only one set of electrodes is active. This behavior is likely due to small imperfections in the disk which serve to split the degenerate resonance frequencies, resulting in a natural phase offset between the orthogonal modes at a specific drive frequency. This natural phase offset can be exploited to create a TWUM that can be operated with a single phase source (as opposed to the dual phase requirement for traditional TWUM) as described in [53]. This frequency splitting was confirmed in smaller devices that exhibit larger frequency split using laser Doppler vibrometry.

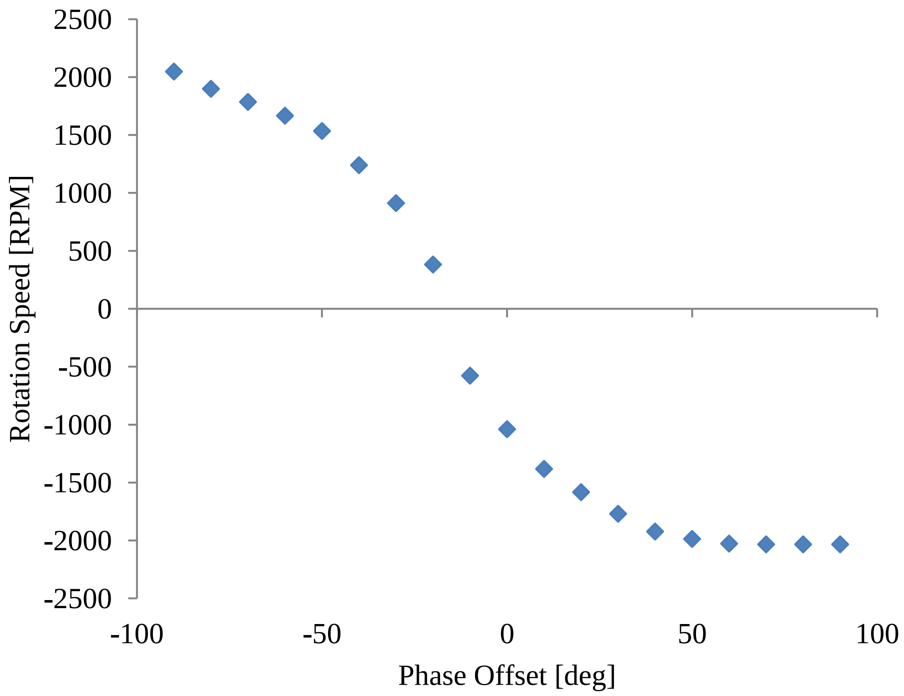

Figure 5.7. Rotation speed as a function of phase shows a smooth but nonlinear response. The zero speed crossing occurs at a non-zero phase offset, demonstrating that traveling waves may be generated within the stator using input signals with no phase offset.

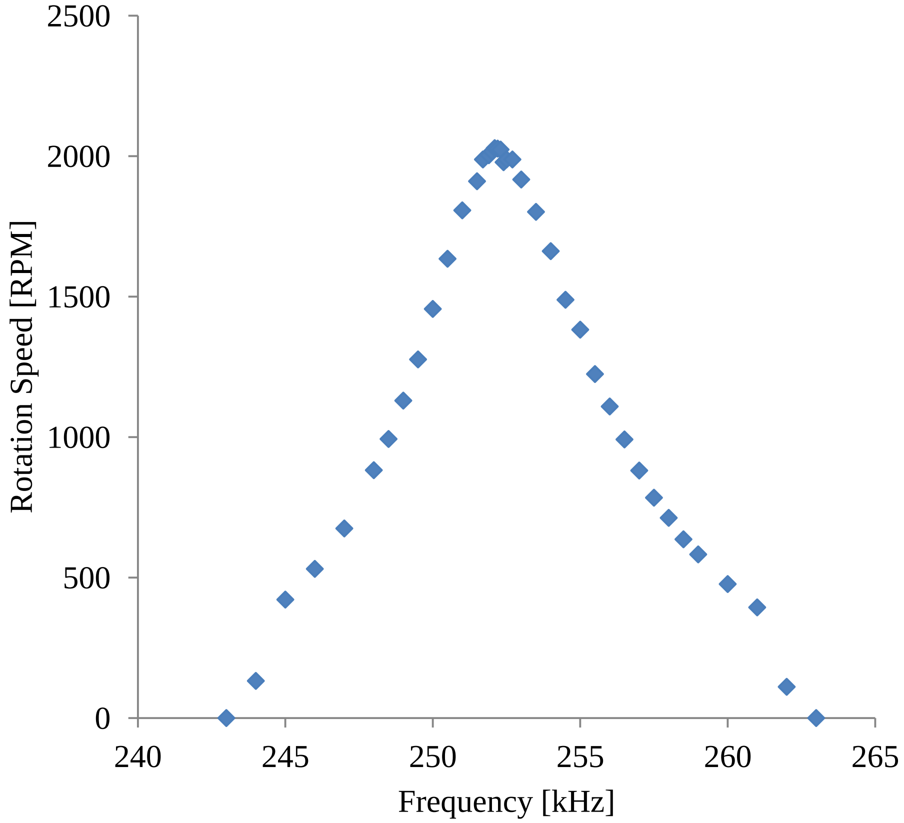

Figure 5.8. The speed-frequency relationship, shown here, does not exhibit any significant Duffing behavior typically observed in macro-scale motors.

Rotation speed as a function of frequency has also been characterized and is shown in Figure 5.8. Frequency control can also be used to control motor speed, however it is often not used in macro-scale motors because researchers have noted that the motor suddenly stops when gradually decreasing the frequency. Sattel attributes this to a catastrophic jump due to non-linear dynamics and shows Duffing-like behavior experimentally [61]. Sattel argues that the catastrophic jump causes a sudden decrease in deflection, which drops below the level required for motion [8]. Because this Duffing behavior exists in macro-scale motors, temperature change can shift the resonance frequency, leading to a catastrophic jump during operation. To avoid this catastrophic jump, macro-scale motors must operate away from the peak resonance condition, reducing the performance of the motor. Contrary to what is observed in macro-scale motors, there is no softening resonance curve observed in these micro-scale motors for either the stator component or the motor. This allows the motor to operate at peak resonance condition without concern for the sudden stop seen in their macro-scale counterparts.

A separate 2 mm diameter motor was used to characterize the torque performance as a function of speed as shown in Figure 5.9. A starting torque of 2.5 μN·mm was calculated using a high speed camera by monitoring the change in angle over time during the start-up phase. This change of angle over time was used to determine the angular acceleration. Torque is obtained by multiplying the angular acceleration by the rotational inertia of the rotor according to the equation, $\tau = \alpha I$, where τ is the torque, α is the angular acceleration, and I is the rotational inertia. This torque value does not match the predicted stall torque value shown in Figure 5.4, approximately 3 mN·mm, likely due to contact with the wirebonds and the large amount of slip that exists during the change in phase. It should be noted that the motor torque could be greatly increased by providing a larger normal force beyond merely the self-weight of the rotor since the frictional force applied between the stator and rotor is related to the normal force applied. Given the applied load and size, the motor torque compares favorably to the pseudo-traveling wave motor in [14] at 41 nN·mm, the 8 mm diameter magnetoelastic standing wave motor [32] at 30 μN·mm, and the standing wave bulk PZT motor with preload [6] at 3.2 mN·mm. In order to account for the various shapes and sizes of these motors, torque density can be used to compare the torque normalized by volume. Table 5-1 shows the some of the previously mentioned motors in terms of torque density using available dimensions to estimate device volume.

Table 5-1. Reported ultrasonic motor preload and torque density

Motor Description	Ref.	Preload [μN]	Torque Density [μN·mm / mm^3]
Thin-film TWUM	This work	18	1.6
Thin- film Pseudo-TWUM	[14]	81	0.034
Magnetoelastic standing wave motor	[32]	215	1.2
Thin-film PZT tube motor	[24]	5300	87

Other miniature ultrasonic motors that are significantly larger than this thin-film TWUM (8 mm to 10 mm in diameter) have demonstrated increased torque under increased normal load using custom watch dynamometers [13] and [62] which can also be seen from [24] in Table 5-1. These motors demonstrate that with larger applied normal loads, much larger torques can be produced. This large applied normal force, however, is difficult to achieve at such small scales, especially if the motors are to be applied in a system, and not simply tested on a micro-dynamometer. Potential methods for accomplishing this are discussed in the proposals for future work in Section 6.2.5.

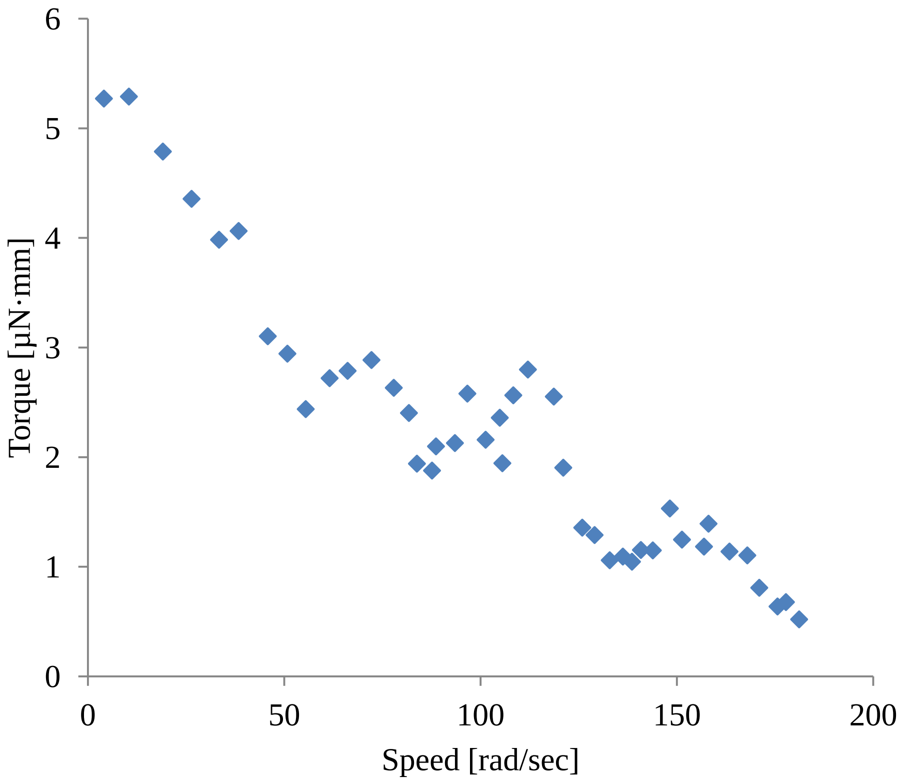

Figure 5.9. Torque is plotted here as a function of speed, both quantities calculated using high speed video capture to measure angle over time.

5.4 Summary

The design and results described within this section describe the first demonstrated wafer-scale traveling wave ultrasonic motor. At 2 mm in diameter and 1 mm thick (including the nearly 0.5 mm thick substrate), this motor is also the smallest traveling wave ultrasonic motor ever reported in the literature. Motor speeds compare favorably to the predicted unloaded speed from the model. Reported startup torque values compare favorably to other work given the small normal load applied. Larger normal loads will proportionally increase the torque. These results are summarized in Table 5-2.

Table 5-2. Summary of motor geometry and performance specifications

Parameter	Value
Speed	100-2050 RPM
Power consumption	0.4 – 4.0 mW
Starting voltage	4V
Start-up torque	2.5 μN·mm
Motor diameter	2 – 3 mm
Frequency	50-350 kHz

6 Conclusion

Miniature rotary systems have long been studied in micro-electromechancal systems (MEMS) to varying degrees of success. Because of the millimeter scale, these rotary platforms often operate at high speeds with little potential for output torque beyond single micronewton-meters. This dissertation outlines the development and demonstration of a miniaturized traveling wave ultrasonic motor (TWUM), which provide rotations at practical speeds (0 to 2000 RPM) and potential for significant output torque on the order of 0.2 mN-m under reasonable normal loads. Through thin-film deposition and microfabrication techniques, this work has produced the first successful and smallest wafer-scale microfabricated TWUM.

Table 6-1. Summary of motor geometry and performance ranges

TWUM Parameter	Value
Speed	100 - 2050 RPM
Power consumption	0.4 - 4.0 mW
Motor diameter	2 - 3 mm
Rotor thickness	500 µm
Stator thickness	20 - 30 µm
Frequency	50 - 350 kHz

6.1 Summary and Contributions

The demonstration of this thin-film microfabricated TWUM is accompanied by several further contributions to the field, which will be summarized below by section. Included in the summary of contributions are: a backside vapor HF release, microfabricated disc stators with asymmetric anchor conditions, ring stator tether design, and single phase TWUM.

6.1.1 Fabrication

The fabrication process of the traveling wave ultrasonic motors, described in Section 2, leverages many accepted microfabrication techniques while providing new fabrication methods that could be more widely applied. One new technique is the backside release of the traveling wave ultrasonic stator. The disc stator design requires that a continuous surface, 1-3 mm in diameter, be fully released except for a center anchor tied to the substrate. This means that undercut lengths from 0.4 to 1.3 mm must be etched. These large undercut lengths are difficult to achieve, especially without over-etching the center anchor. In order to shorten the etch time and control the release process, backside holes were etched into the handle wafer silicon. These holes allowed vapor hydrofluoric acid to travel to the buried silicon dioxide and etch this buried sacrificial layer away. A modification of this process, involving over-etch during the deep reactive ion etching, created small outcrops at the buried silicon dioxide layer. This outcropping, called footing, is usually undesirable because it can change the properties of the affected device. However, with the disc stator, the etch is performed from the backside of the wafer stopping at the buried oxide beneath a 20 to 40 µm thick device Si layer and, the device Si geometries and properties are unaffected by footing in the handle wafer. The footing allows the device undercut time to be significantly reduced, and in some cases, can even eliminate the need for a vapor HF release etch all together for silicon-on-insulator devices.

6.1.2 Disc Stator Design and Characterization

The design of the resonant disc stator components and their characterization, using laser Doppler vibrometry, are presented in Section 3. The design of the disc stators borrowed largely from previous work in macro-scale traveling wave ultrasonic motors. The design is intended to allow excitation and control of two orthogonal standing waves, using a piezoelectric material. The characterization of these standing waves in the microfabricated stators as a function of frequency, peak voltage, and bias voltage is described in Section 3.2. These standing waves, when combined out of phase, create a traveling wave, which is used for rotary drive of the rotor. This traveling wave was observed experimentally using laser Doppler vibrometry.

Although the design of the disc stator was largely leveraged from previous work, the center anchoring condition required a unique fabrication process, as described above. This process resulted in asymmetric anchor conditions, offsetting the resonance frequencies, and shifting the location of nodal diameters in some small discs. This asymmetric anchor condition prevented traveling wave generation in the small discs. A study of these small discs correlated the nodal line location with etch holes that were significantly larger than the surrounding holes. This larger hole caused faster etching and more footing, allowing for preferential etching of the silicon dioxide layer. The preferential etch created hexagonal anchors, rather than the intended circular ones, resulting in the asymmetric anchor that prevented the generation of the traveling wave. The etch hole design was modified and standing wave control was subsequently demonstrated in these discs with little frequency offset. This work highlights the importance and influence of all aspects of the fabrication process and how they relate to the mechanical design.

The standing waves and traveling waves in these disc stators were characterized using laser Doppler vibrometry. Amplitudes over 1 μm of out of plane deflection were demonstrated in 2 mm diameter discs at frequencies over 450 kHz, with the thickness of the buried oxide layer limiting further deflection. Quality factors in air of 95 were achieved, unaffected by drive amplitude.

Table 6-2. Summary of stator geometry and performance specifications

Parameter	Value
Stator diameter	1 - 3 mm
Stator thickness	20 - 30 μm
Actuation frequency	50 - 600 kHz
Deflection	0 - 1 μm
Quality Factor	95

6.1.3 Ring Stator Design and Characterization

Ring stators, which provide integration benefits for traveling wave motors, are described in Section 4. The ring stators are tethered from the outer edge and have potential to provide easier integration, while providing other unique functionality, such as a through-motor hole for optical purposes. Although the stator design is very similar to the disc stator, the tether design provided significant challenges. Experimental demonstration of 30% frequency mismatch due to tethers was presented. To reduce this frequency mismatch, the tethers were modeled as individual resonant systems. The negative effects of tethers were mitigated by reducing boundary condition mismatch and strain at the anchor point. Through design and finite element analysis, the designed frequency mismatch was reduced to 0.86% for mismatched designs and to 7 ppm for frequency symmetric designs.

The ring stators with the mechanical impedance transformer were fabricated and tested. Experimental results using laser Doppler vibrometry showed a two-fold increase in deflection and a 40% increase in quality factor compared to ring stators with straight tethers. Traveling waves were demonstrated in these ring stators and presented as phase-stepped images.

6.1.4 Motor Modeling and Characterization

Modeling and characterization of motor performance were presented in Section 5. In this section, a fundamental model developed in [13] is described. A 3mm diameter stator with a 2 mm diameter rotor was used to characterize speed as a function of voltage, frequency, and phase, as well as power as a function of voltage. This matched well with the modeled no-load speeds. This 3 mm diameter rotary motor was the first demonstration of a wafer-scale thin-film TWUM. This motor also exhibited rotary motion with zero phase offset, implying that the motor could be altered to create a single source drive.

A 2 mm diameter stator with a 2 mm diameter rotor was used to characterize the start up torque of the motor. Although the limited normal force resulted in a small output torque of 5.3 μN•mm, the motor compares well with similarly loaded and sized ultrasonic motors. More importantly, the motor has the capability to increase the output torque dramatically with larger normal forces, up to 0.2 mN-m under 1 mN applied load. This 2 mm diameter motor is composed of a 500 μm thick silicon rotor, a 30μm thick PZT/silicon stator, and 450 μm of inactive substrate. Even including this inactive substrate, this motor represents the smallest traveling wave ultrasonic motor ever reported.

6.2 Future Works

This section highlights potential extensions of this project for further work and development. Some of these concepts and questions cannot currently be attempted or answered, but are provided here as a guide for future research. Included here is discussion of the following topics: robust stator release process, stator teeth, reduction of loss mechanisms, model expansion to account for inaccuracies, rotor pre-load, wafer-scale integrated rotors, and potential device application.

6.2.1 Robust stator release process

The current process for release is cumbersome, long, and potentially harmful to the structural and active materials in the stator. The below sections outline potential extensions of this work toward creating a more robust release process. The first section discusses removing the timed aspect of the etch. The second section discusses material compatibility challenges in the current process.

6.2.1.1 Untimed

If the process could be modified so that hard etch stop could be introduced, then the release process could become significantly more repeatable. Because undercut times vary based on undercut length as well as etch rate, the current process does not consistently release devices within the desired etch time. To test if devices are released, residual stress curvature of the stator can be monitored, however this does not guarantee full release. Figure 6.1 shows a laser Doppler vibrometry scan of a disc stator that exhibits residual stress curvature, yet is not completely released.

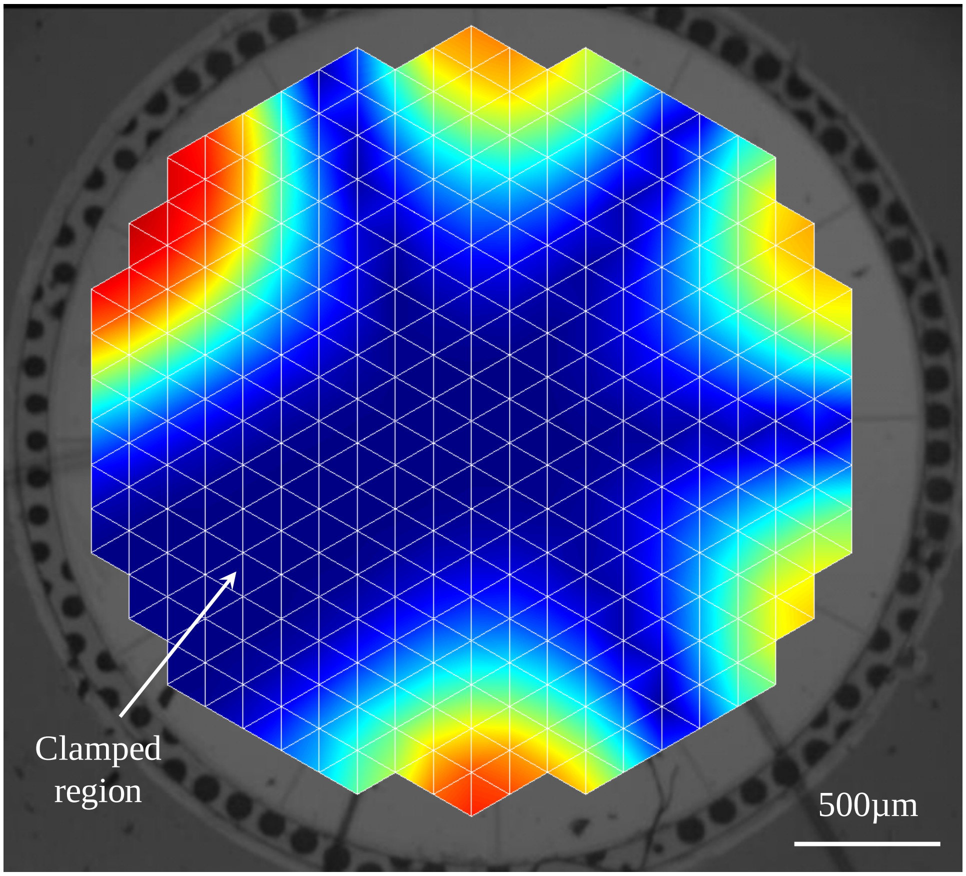

Figure 6.1. Laser Doppler vibrometry data showing a clamped portion of an otherwise released disc stator.

This uncertainty of release could be eliminated if a hard etch stop could be designed in the process. Furthermore, the etch stop would allow for faster undercut speeds to be achieved, because the etch stop would define the stator structure rather than the progressive etch front in the current process. Conceptual cross sections including a hard etch stop is illustrated Figure 6.2.

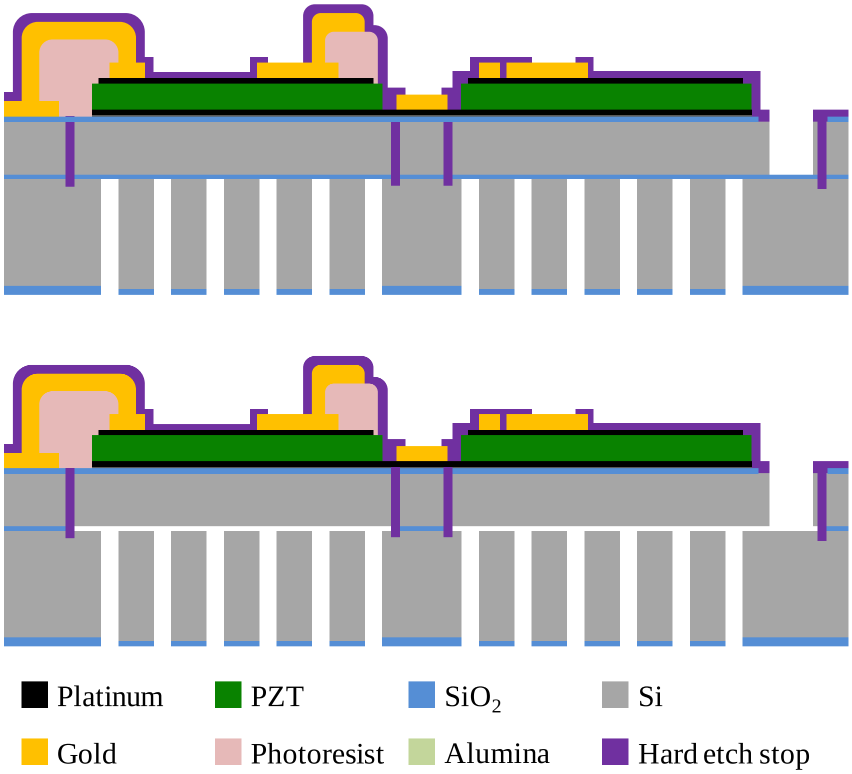

Figure 6.2. Conceptual cross-sections showing a hard etch stop incorporated into the traveling wave ultrasonic motor process.

Alternatively, if ring stators are used, the need for the backside etch holes and vapor HF undercut are eliminated because the stator would be supported from the side with tethers, rather than from the center through the buried oxide. This would simplify the fabrication process and eliminate the need for a hard etch stop.

6.2.1.2 Material compatibility

Some of the problems with release could also be solved by incorporating a more effective passivation layer. Although the alumina is effective at shielding the field oxide from etch during release, it is clear that it is an ineffective barrier for sidewall protection. Further, if the HF begins attacking the oxide under metal traces, the etch runs away along the metal trace, resulting in 30 µm wide traces that are completely undercut. The passivation is still necessary because the HF will attack the silicon dioxide insulating layer between the bottom platinum electrode and the silicon. This silicon dioxide is not only an insulating layer, but also functions as a template for oriented PZT growth. Furthermore, the PZT can also be attacked by the HF, degrading its effectiveness within the system. If instead, a different release was used that was more compatible, the stator fabrication process could become more flexible and the release less problematic.

6.2.2 Stator teeth

Small posts protruding from the surface of the stator, called stator teeth, could provide increased speed and performance from these traveling wave motors. The maximum speed of the traveling wave motor is determined by the wave number, frequency, deflection, and distance from the neutral axis. Because the stator teeth are small and independent, they have little effect on wave number, frequency or deflection, however they can dramatically increase the distance from the neutral axis. This increased distance results in increased speed of the motor according to Equation 6.1.

$$\omega_{rotor_{max}} = \frac{-w\omega k(h+h_{tooth})}{r} \tag{6.1}$$

Here, w is deflection, ω is frequency, k is the wave number, h is the distance from neutral axis to stator surface, h_{tooth} is the height of the tooth, and r is the contact radius.

Potential methods for incorporating stator teeth into the traveling wave ultrasonic stator were investigated, including aerosol deposition and electroplated metal. Electroplated metal was the more desirable choice, due to fine resolution and alignment possible with photolithographically defined molds, however our collaborators specializing in such electroplated metal patterns were set back due to tool malfunctions which required an entire process redesign. If this fabrication can be accomplished in the future, the expected performance gains should easily be attained.

6.2.3 Reduction of loss mechanisms

As described in Section 5.2.1.2, out of plane deflection is extremely important for determining the motor performance characteristics. This deflection can be increased by reducing the loss mechanisms in the traveling wave stator. This is of particular note for ring stators, where the quality factor is less than half of the disc stator quality factor. To reduce loss in these devices, design optimization could be performed on the tethers to reduce the strain at the interface.

Another potential way to achieve higher deflections is to shape electrodes to specifically excite one mode [63]. In beams, this is easily performed by matching the width of the electrode with the mode shape in order to exploit orthogonality. This electrode shaping is not as simple in the two dimensional case because there is no equivalent to electrode width that can be exploited. Still, the shape of the electrodes could be modified to prevent cancelation. For example, with the current electrode layout a B_{13} mode in the disc sees positive excitation both inside the nodal circle and outside the nodal circle despite these sections producing opposite strain states. This inevitably causes some cancelation to occur. Modifying the electrode layout to prevent such cancelation may result in larger deflection.

6.2.4 Model expansion to account for inaccuracies

The model described in Section 5.2 provides a good baseline for expected performance for the TWUM, however there are some phenomena that are not captured in this model. One important point when discussing the presented model is that the model requires a known out-of-plane deflection. This deflection must be obtained experimentally before motor performance can be determined. If, however, the deflection can be modeled from geometric and material properties, then motor optimization can be performed without the need for experimental testing. This is of particular importance for microfabricated motors due to the long fabrication process which can only produce a subset of designs per run. For this reason, modeling the motor performance before fabrication would lead to improved designs in significantly less time.

Hagood described using a Hamiltonian approach to determine out of plane deflection in a motor [64], and this was later modified by Hagedorn to include rotor flexibility in determining motor performance [65]. This modeling, however, produced incorrect results for out of plane deflection. Hagedorn describes the electromechanical transformation factor (which he calls the electromechanical coupling factor, not to be confused with the piezoelectric electromechanical coupling factor, k_{31}) which relates actuation voltage to deflection results by stating, “It turns out that the calculated value of the electromechanical coupling factor differs greatly from the value identified using the experimental data” [65]. Potential explanations offered in the paper include inadequate modeling of the bonding layer and uncertainty in the piezoceramic parameters, especially in e_{31}. Significant mismatch between modeled deflection and experimentally observed deflection were also observed in these microfabricated stators. Here, there is no concern over the bonding layer (because it does not exist) or in material properties, because they are measured. The model was validated for the one dimensional case of a beam in [66]. It is unclear what causes this model inaccuracy, perhaps inaccuracies in accounting for two-dimensional strain effects in the disc or ring stators. If the model can be properly developed, then the motor model could be used to determine performance before fabrication, allowing for design optimization. Such a model would be of great benefit beyond traveling wave motors, having application in microfabricated resonators and filters as well.

If this fundamental problem can be solved, then further refinements by Hagood [65] and Hagedorn [65], transient dynamics and rotor flexibility respectively, can be added into the model for a more complete understanding of the motor operation, including these secondary effects.

6.2.5 Rotor preload

The first of two future work proposals related to an integrated motor involves increasing the normal load between stator and rotor. It has been shown by Flynn [13], that increased load increases torque generation at a near linear rate up to a limit. This increased torque potential is one of the advantages of the TWUM over the electrostatic or electromagnetic motor. Unfortunately, this increased load is extremely difficult to create in such a small platform. Because microelectromechanical systems (MEMS) are essentially two dimensional systems, large forces in the out of plane direction are incredibly hard to create. Furthermore, commercial off the shelf bearings which can be used in macro-scale motors do not exist for MEMS-scale parts.

6.2.5.1 Non-MEMS Package

Flynn [13] and Dubois [62] used a non-MEMS package to provide preload. Specifically, custom-made dynamometers were created by watch manufacturers. This of course would not be used as a system integrated motor, but simply highlights the fact that jewel bearings from watch manufacturers offers a potential solution to the rotor preload problem.

6.2.5.2 Micro ball bearings

Hanrahan [56] has produced a micro ball bearing supported rotating stage. This stage could be integrated with the traveling wave ultrasonic stator to create a motor with preload, supported through the ball bearings. The bearings have been shown to produce very little friction, while able to support significant loads. Communication with the author has indicated that in order for the two platforms to be integrated, the stator component would need to allow for 25 µm of sag in the rotor. This rotor sag can be covered by including stator teeth (discussed above) which extend up from the stator surface as shown in Figure 6.3.

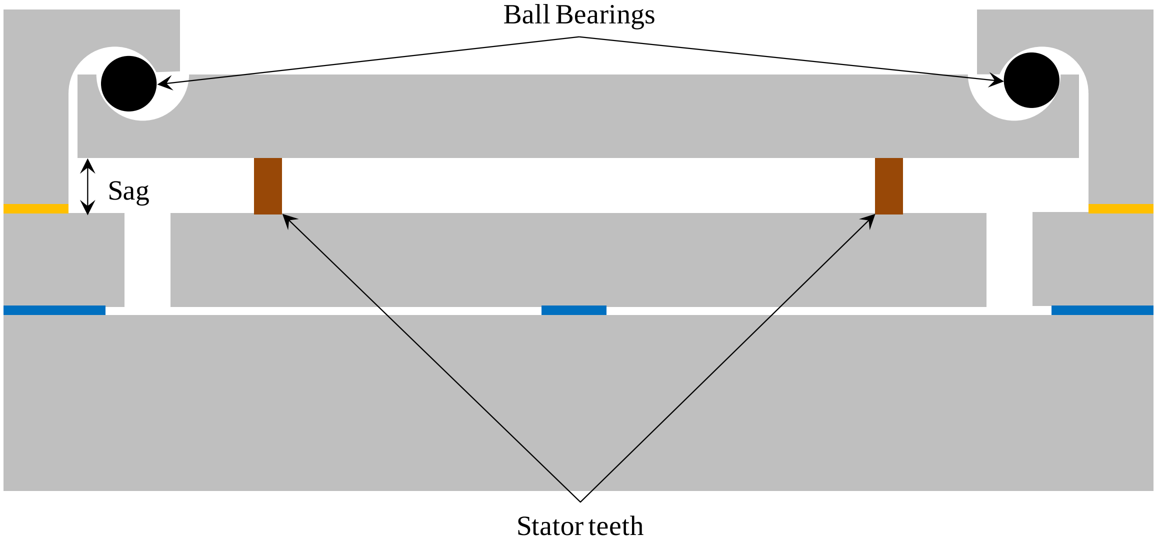

Figure 6.3. Stator teeth can account for the rotor sag from the ball bearing platform.

6.2.5.3 Magnetic preloading

Preloading the rotor using magnetic attraction was also explored as a potential solution for the normal load problem [67]. Small nickel rings were used as rotors with a permanent magnet placed beneath the package to provide a magnetic field. This attempt was unsuccessful because the rotor was not pulled directly down on to the stator, but was rather rotated or pulled to one side depending on the orientation of the magnetic field. This may have been due to the presence of the package or the silicon substrate distorting the magnetic field.

6.2.5.4 Bonding preload

Section 4.1.2 discusses a potential benefit of the hollow center in a ring stator for rotor preloading. This would be similar to the bonding preload shown in [6]. The elastic strain created during the wafer bonding process would create a constant preload on the surface, increasing the torque. Applying force at the center of the rotor would allow for the mechanical advantage at the contact points to overcome the frictional resistance from the static component, especially if the center contact point is small in diameter. Since in this configuration, the top side of the rotor is inaccessible because of the preloading mechanism, the backside of the handle wafer can be used as the rotor surface. This configuration is illustrated in Figure 6.4. This three layer preload component could be made using the multi-layer electroplated copper process described in [68].

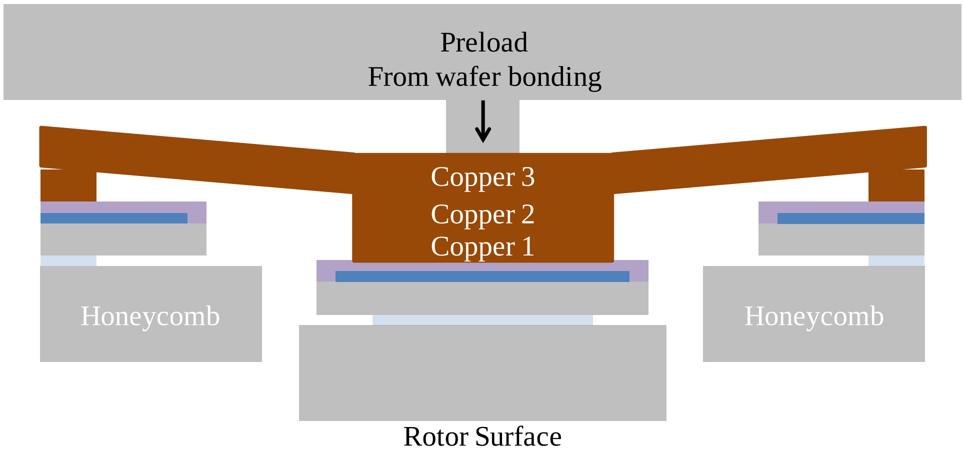

Figure 6.4. This backside rotor conceptual diagram shows a possible path to preload that would not be feasible without using a ring stator.

6.2.6 Wafer-scale integrated rotor

The ideal motor process would include some sort of wafer-scale integrated rotor, to create a batch producible, no assembly millimeter-scale traveling wave ultrasonic motor. Since early in the development in micromotors [69], electroplated rotors have been reported in the literature, such as [70], [71], and [72], specifically for in-plane motor drive. Early on, it was noted that it can be difficult to drive passive components since multi-layer components would be necessary [73]. One approach which showed immense promise was leveraging an electroplated copper process which was integrated into the PiezoMEMS process at ARL [74]. This process uses multiple photolithographic molds for electroplating to create complex multi-layer structures. Figure 6.5 shows a sample electroplated rotor as a rack and pinion system with interlocking gear teeth.

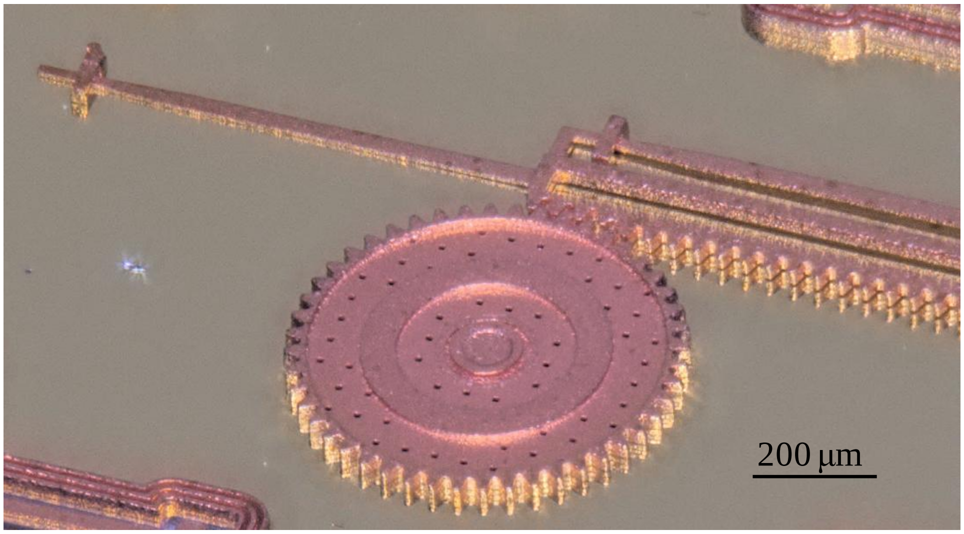

Figure 6.5. Fabricated rack and pinion test rotor (no stator) using a multilayer electroplating process.

Many rotor designs were created which used the high resolution photolithographic molds to create complex interlocking mechanism. Samples of these designs are shown in Figure 6.6 through Figure 6.9.

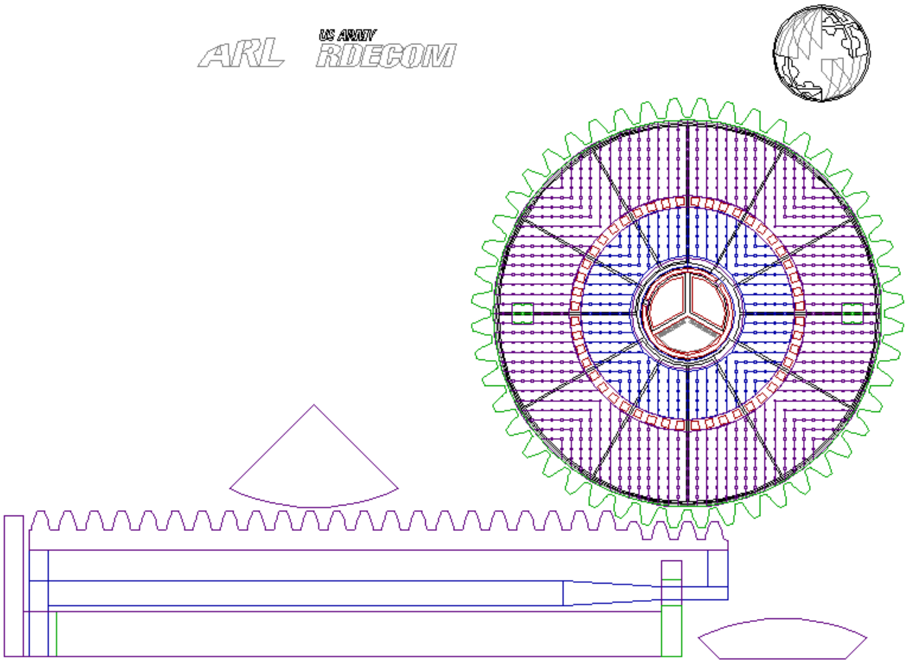

Figure 6.6. Rotor design using a multi-layer electroplating process to create a rack and pinion.

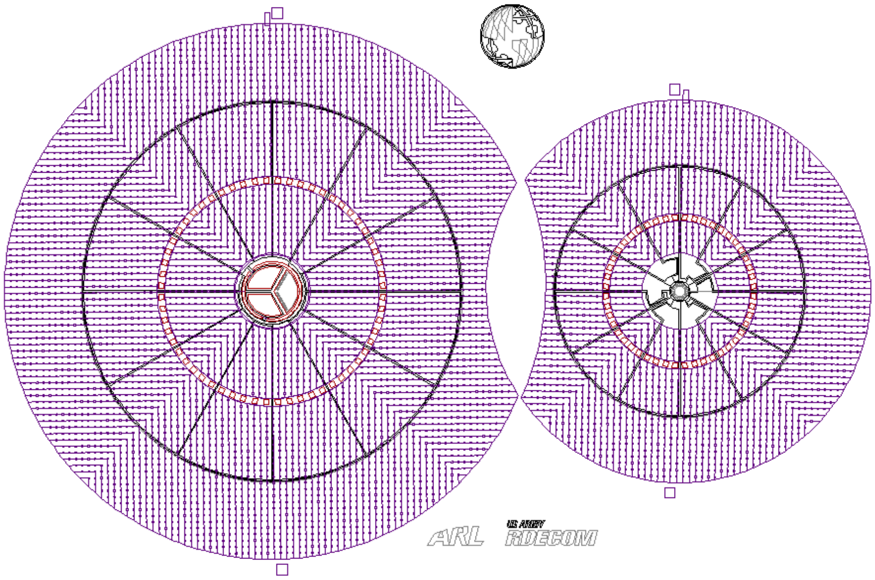

Figure 6.7. Rotor design using a multi-layer electroplating process to create interlocking rotors.

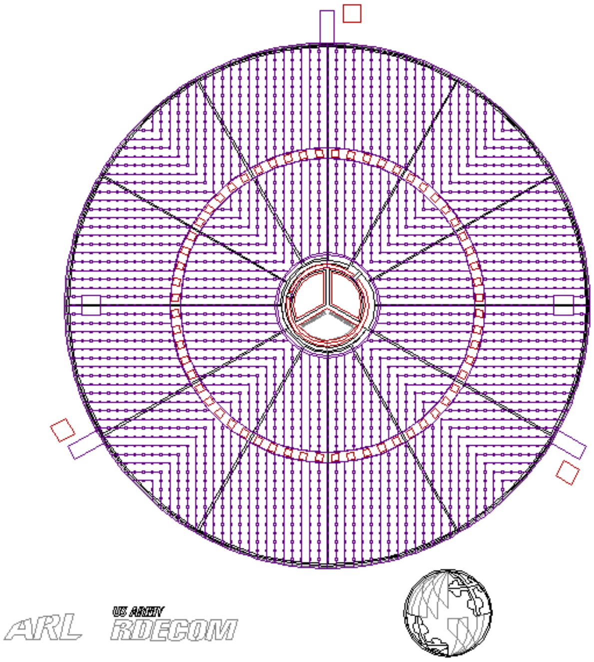

Figure 6.8. Rotor design using a multi-layer electroplating process to create a rotor with mechanical stops.

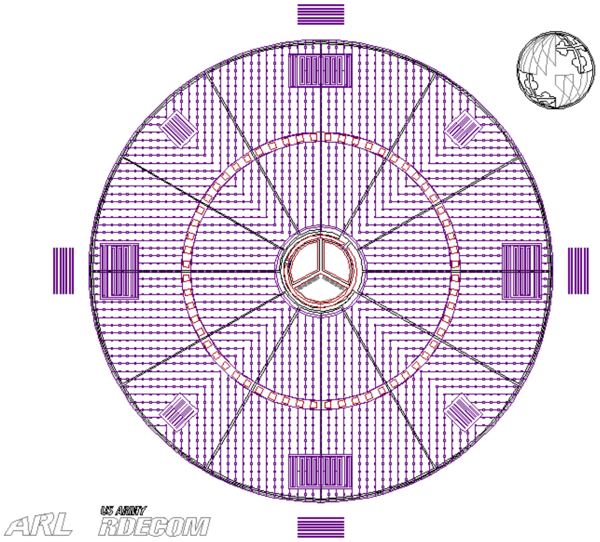

Figure 6.9. Rotor design using a multi-layer electroplating process to create a self-calibrating inertial sensor (in collaboration with the *SonicMEMS* Laboratory at Cornell).

Ultimately, these designs were unrealizable as our collaborators specializing in the multi-layer electroplating process have lost the infrastructure capabilities necessary to create these multi-layer structures due to tool malfunctions and process inconsistencies. A complete process redesign was performed, however only inset structures were able to be demonstrated, eliminating the possibility of rotor integration. If this process can be re-created, or re-designed with different materials that are less sensitive to process temperature, these designs for wafer-scale integrated rotors could be realizable.

6.2.7 Device application

As these motors develop in capability and complexity, it is possible that some of these potential applications can be further investigated.

6.2.7.1 Fuzing Systems

Small scale safe and arm devices, or fuzes, have been created using microfabrication techniques using inertial forces from the spin of the round [21] and thermal actuation [4] [5]. Both of these actuation techniques require large power, either from the spin of the round, or electrical power for thermal actuation. For some applications (low-G setback power), there is limited energy available for fuze actuation. Ultrasonic motors provide a potential for filling the technology gap for this subset of applications.

To create a MEMS fuze, two steps are necessary. The device must be first unlocked, and then the explosive must be moved into line. The explosive is separated to prevent unintended triggering. The locking mechanism is a physical lock which prevents the motion of the explosive. Using two traveling wave ultrasonic motors would allow for two motors to function as a command lock and one component as an explosive carrier. Such a configuration could looks something like Figure 6.10.

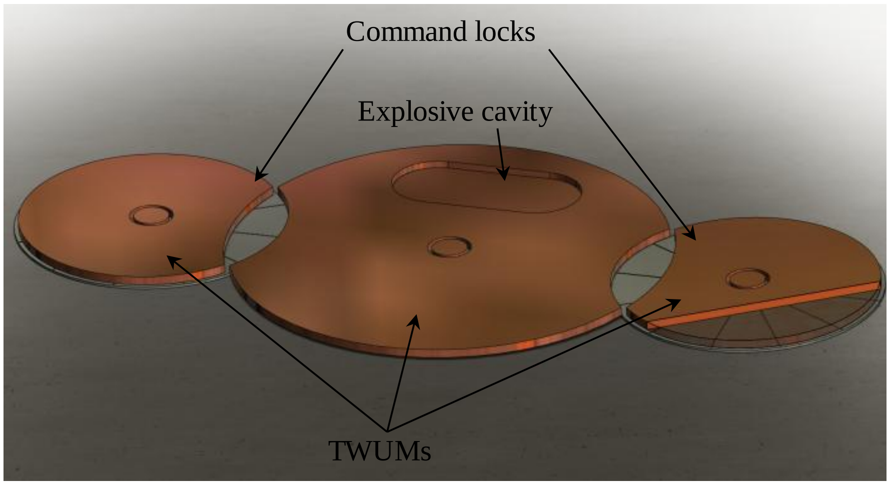

Figure 6.10. Conceptual illustration of a traveling wave ultrasonic motor fuze system.

Furthermore, because the motors act in a rotary capacity, a TWUM fuze could be combined with a linear MEMS fuze to increase reliability, while eliminating common mode failures. This would result in high reliability with a very small footprint. A geared rotor could also be used to move a linear rack device to function as this linear fuze.

6.2.7.2 Intravascular ultrasound

An interesting application for small scale motors is in intravascular ultrasonic imaging [75]. This imaging technique uses a rotating piezoelectric ultrasound transducer to investigate the structure of the vascular tissue, and is used to diagnose and monitor atherosclerosis (artery wall thickening) [20]. To accomplish this rotation of the ultrasound element, a torsion rod (connected to a motor outside of the body) is inserted with the catheter tip. This torsion rod must be sufficiently stiff to transfer the torque from the motor, however this stiffness limits the depth to which the catheter can reach. Placing the motor at the tip allows the catheter to reach deeper into the body in a less invasive manner. The tip motor could also reduce wobble that is one of the problems experienced during imaging [20].

6.2.7.3 Rotary position actuator

Some applications require a motor that can rotate to a precise position, or scan over a range of these positions. One example would be portable lidar systems, which use laser ranging scanned in two dimensions to create a three dimensional real time image. These systems carry large and expensive lasers in order to maintain high signal at oblique angles because the receiver is fixed. If the receiver could be rotated to align to the incoming beam, the required laser power could be reduced such that the laser could be replaced by a lower power, smaller, cheaper source. Such a replacement would allow the system to be constructed at half the size for half of the cost. To accomplish this, the motor would require positional feedback.

6.2.7.4 Rotary toggle actuator with mechanical stops

The motor could also be used as a rotary toggle, eliminating the need for positional measurement. The toggle positions could be determined by mechanical stops, which would allow the motor to rotate between these points without feedback control. Applications such as optical switching or the fuze command lock described above would be good candidates for such a toggle actuator.

7 Bibliography

[1] K. Uchino, "Piezoelectric ultrasonic motors: overview," *Smart Materials and Structures,* vol. 7, pp. 273-285, 1998.

[2] T. Morita, "Miniature piezoelectric motors," *Sensors and Actuators A,* vol. 103, pp. 291-300, 2003.

[3] K. Uchino and J. R. Giniewicz, Micromechatronics, New York, NY: Marcel Dekker Inc., 2003.

[4] D. Jean, M. Beggans, G. Laib and D. Olson, "MEMS microdetonator/initiator apparatus for a MEMS fuze". USA Patent 7 490 552, 17 February 2009.

[5] L. Fan, M. Beggans, E. Chen, G. Laib, D. Olson, D. Jean and J. Hendershot, "MEMS Fuze Assembly". USA Patent 7 913 623, 29 March 2011.

[6] Y. Suzuki, K. Tani and T. Sakuhara, "Development of a new type piezoelectric micromotor," *Sensors and Actuators,* vol. 83, pp. 244-248, 2000.

[7] T. Ishii, S. Ueha, K. Nakamura and K. Ohnishi, "Wear properties and life prediction of frictional materials for ultrasonic motors," *Japanese Journal of Applied Physics,* vol. 34, pp. 2765-2770, 1995.

[8] S. Thesis, *Dynamics of ultrasonic motors,* Darmstadt: App. Mech, Technische Universitat Darmstadt, 2002.

[9] T. Sashida and T. Kenjo, An Introduction to Ultrasonic Motors, New York, NY: Oxford University Press, 1993.

[10] I. Okumura and H. Mukohjima, "A Structure of Ultrasonic Motor for Auto Focus Lenses," in *Proceedings from MOTOR-CON,* Long Beach, CA, 1987.

[11] T. Maeno, T. Tsukimoto and A. Miyake, "The contact mechanism of an ultrasonic motor," in *International Symposium on Applications of Ferroelectrics*, Urbana-Champaign, IL, 1990.

[12] D. S. McCosh, "Wireless Motor Tilts Wheel," *Popular Science,* p. 37, February 1999.

[13] A. M. Flynn, *Piezoelectric Ultrasonic Micromotors,* Cambridge, MA: Dept. Elect.

Eng. and Comp. Sci., Massachusetts Institute of Technology, 1997.

[14] A. M. Flynn, L. S. Tavrow, S. F. Bart, R. A. Brooks, D. J. Ehrlich, K. R. Udayakumar and L. E. Cross, "Piezoelectric micromotors for microrobots," *Journal of Microelectromechanical Systems,* vol. 1, no. 1, pp. 44-51, 1992.

[15] D. A. Henderson, Q. Xu and D. Piazza, "Continuous Auto Focus for Next Generation Phone Cameras," in *ACTUATOR 2010*, Bremen, Germany, 2010.

[16] A. M. Flynn, "Gnat robots: a low-intelligence low-cost approach," in *Solid-State Sensor and Actuator Workshop*, Hilton Head, SC, 1988.

[17] A. M. Flynn, R. A. Brooks and L. S. Tavrow, "Twilight Zones and Cornerstones," Massachusetts Institute of Technology, Cambridge, MA, 1989.

[18] K. Y. Ma, P. Chirarattananon, S. B. Fuller and R. J. Wood, "Controlled Flight of a Biologically Inspired, Insect-Scale Robot," *Science,* vol. 340, no. 6132, pp. 603-607, 2013.

[19] I. Yamano and T. Maeno, "Five-fingered robot hand using ultrasonic motors and elastic elements," in *Proceedings of the International Conference Robotics and Automation*, Barcelona, Spain, 2005.

[20] G. Mishkel and N. Goswami, "IVUS Training Video #1: An Introduction to IVUS [video]," Boston Scientific, 2009. [Online]. Available: http://www.bostonscientific.com/templatedata/imports/HTML/virtual-learning-center/ivus-intro-video/ivus-intro-video-landing.html. [Accessed 1 December 2012].

[21] C. H. Robinson, R. H. Wood, M. R. Gelak, T. Q. Hoang and G. L. Smith, "Ultra-miniature electro-mechanical safety and arming device". USA Patent 8 276 515, 2 October 2012.

[22] P. Muralt, M. Kohli, T. Maeder, A. Kholkin, K. Brooks, N. Setter and R. Luthier, "Fabrication and characterization of PZT thin-film vibrators for micromotors," *Sensors and Actuators A,* vol. 48, pp. 157-165, 1995.

[23] T. Morita, M. K. Kurosawa and T. Higuchi, "A cylindrical micro ultrasonic motor using PZT thin film deposited by single process hydrothermal method (2.4 mm, Ls10 mm Stator transducer)," *IEE Transactions on Ultrasonics, Ferroelectics, and Frequency Control*, vol. 45, no. 5, pp. 1178-1187, 1998.

[24] T. Morita, M. K. Kurosawa and T. Higuchi, "A cylindrical shaped micro ultrasonic motor utilizing PZT thin film (1.4 mm in diameter and 5.0 mm long stator transducer)," *Sensors and Actuators A,* vol. 83, pp. 225-230, 2000.

[25] S. Dong, S. P. Lim, K. H. Lee, J. Zhang, L. C. Lim and K. Uchino, "Piezoelectric Ultrasonic Micromotor with1.5 mm Diameter," *IEEE Transactions on Ultrasonics, Ferroelectrics, and Frequency Control,* vol. 50, no. 4, pp. 361-367, 2003.

[26] S. Cagatay, B. Koc, P. Moses and K. Uchino, "A Piezoelectric Micromotor with a Stator of d = 1.6 mm and l = 4 mm Using Bulk PZT," *Japanese Journal of Applied Physics,* vol. 43, no. 4A, pp. 1429-1433, 2004.

[27] V. Kaajakari and A. Lal, "Optimization of a bulk-driven surface micromachined ultrasonic micromotor," in *IEEE Ultrasonics Symposium,* Atlanta, GA, 2001.

[28] V. Kaajakari and A. Lal, "Micromachined ultrasonic motor based on parametric polycrystalline silicon plate excitation," *Sensors and Actuators A,* vol. 137, pp. 120-128, 2007.

[29] S. Piratla, M. Pandey and A. Lal, "Nanogap ultrasonic actuator for non-contact control of levitated inertial sensor rotor," in *Proceedings of the Solid-State Sensors, Actuators, and Microsystems Workshop,* Hilton Head, SC, 2012.

[30] C. Zhao, Ultrasonic Motors: Technologies and Applications, Beijing: Science Press, 2007.

[31] J. Tang, S. R. Green and Y. B. Gianchandani, "Miniature wireless resonant rotary motor actuated by lithographically micromachined magnetoelastic foil," in *Proceedings of the Solid-State Sensors, Actuators, and Microsystems Workshop,* Hilton Head, SC, 2012.

[32] J. Tang, S. R. Green and Y. B. Gianchandani, "Miniature Wireless Magnetoelastic Resonant Motor With Frequency Selectable Bidirectional Rotation," *Journal of Microelectromechanical Systems,* vol. 22, no. 3, pp. 730-738, 2013.

[33] A. Iino, K. Suzuki, M. Kasuga, M. Suzuki and T. Yamanaka, "Development of a self-oscillating ultrasonic micro-motor and its application to a watch," *Ultrasonics,* vol. 38, no. 1, pp. 54-59, 2000.

[34] PCBMotor, "Rotary Ultrasonic Piezo Motors | PCBMotor," PCBMotor, 2014. [Online]. Available: http://pcbmotor.com/. [Accessed 17 March 2014].

[35] N. S. Technologies, "New Scale Technologies - smart systems for precision motion in small spaces," New Scale Technologies, 2014. [Online]. Available: http://www.newscaletech.com/. [Accessed 17 March 2014].

[36] G. L. Smith, J. S. Pulskamp, L. M. Sanchez, D. M. Potrepka, R. M. Proie, T. G. Ivanov, Q. R. Rudy, W. D. Nothwang, S. S. Bedair, C. D. Meyer and R. G. Polcawich, "PZT-Based Piezoelectric MEMS Technology," *Journal of the American*

Ceramic Society, vol. 95, no. 6, pp. 1777-1792, 2012.

[37] T. Fujii, Y. Hishinuma, T. Mita and T. Arakawa, "Preparation of Nb doped PZT film by RF sputtering," *Solid State Communications,* vol. 149, pp. 1799-1802, 2009.

[38] L. Sanchez, *Personal Communication,* 2014.

[39] L. M. Sanchez, D. M. Potrepka, G. R. Fox, I. Takeuchi, K. Wang, L. A. Bendersky and R. G. Polcawich, "Optimization of PbTiO3 seed layers and Pt metallization for PZT-based piezoMEMS actuators," *Journal of Materials Research,* vol. 28, no. 14, pp. 1920-1931, 2013.

[40] D. M. Potrepka, G. R. Fox, L. M. Sanchez and R. G. Polcawich, "Pt/TiO2 growth templates for enhanced PZT films and MEMS devices," in *Materials Reseach Society Symposium - Microelectromechanical Systems – Materials and Devices IV*, Warrendale, PA, 2011.

[41] S. Trolier-McKinstry and P. Muralt, "Thin film piezoelectrics for MEMS," *J. Electroceramics,* vol. 12, no. 1-2, pp. 7-17, 2004.

[42] *AZ5200 Positive Photoresists,* AZ Electronic Materials Datasheet.

[43] G. L. Smith, R. G. Polcawich, J. S. Pulskamp, T. Waggoner and J. F. Conley, "Atomic Layer Deposited Alumina for use as an Etch Barrier Against Xenon Difluoride Etching," in *Proceedings of the Solid-State Sensors, Actuators, and Microsystems Workshop*, Hilton Head, SC, 2010.

[44] K. R. Oldham, J. S. Pulskamp, R. G. Polcawich and M. Dubey, "Thin-Film PZT Lateral Actuators With Extended Stroke," *Journal of Microrelectromechanical Systems,* vol. 17, no. 4, pp. 890-899, 2008.

[45] R. M. Proie, R. G. Polcawich, J. S. Pulskamp, T. Ivanov and M. E. Zaghloul, "Development of a PZT MEMS Switch Architecture for Low-Power Digital Applications," *Journal of Microelectromechanical Systems,* vol. 20, no. 4, pp. 1032-1042, 2011.

[46] J. Yoon, G. Y. Oh, C. Han, E. Yoon and C. Kim, "Planarization and trench ifihing on severe surface topography with thick photoresist for MEMS," in *Proc. SPIE 3511, Micromachining and Microfabrication Process Technology IV*, Santa Clara, CA, 1998.

[47] G. L. Smith, R. Q. Rudy, D. L. DeVoe and R. G. Polcawich, "Integrated thin-film piezoelectric traveling wave ultrasonic motors," in *Solid-State Sensors, Actuators and Microsystems Conference (TRANSDUCERS), 2011 16th International*, Beijing,

China, 2011.

[48] G. L. Smith, R. Q. Rudy, R. G. Polcawich and D. L. DeVoe, "Integrated thin-film piezoelectric traveling wave ultrasonic motors," *Sensors and Actuator A: Physical,* vol. 188, pp. 305-311, December 2012.

[49] T. B. Gabrielson, "Frequency constants for transverse vibration of annular disks," *Journal of Acoustical Society of America,* vol. 105, no. 6, pp. 3311-3317, 1999.

[50] M. A. Hopcroft, W. D. Nix and T. W. Kenny, "What is the Young's Modulus of Silicon?," *Journal of Microelecromechanical Systems,* vol. 19, no. 2, pp. 229-238, 2010.

[51] T. Sashida, "Motor device utilizing ultrasonic oscillation". USA Patent 4 562 374, 31 Dec 1985.

[52] J. Rho, K. Oh, H. Kim and H. Jung, "Characteristic Analysis and Design of a B14 Rotary Ultrasonic Motor for a Robot Arm Taking the Contact Mechanism into Consideration," *IEEE Transactions on Ultrasonics, Ferroelectrics, and Frequency Control,* vol. 54, no. 4, pp. 715-728, 207.

[53] S. Ueha and Y. Tomikawa, Ultrasonic Motors: Theory and Applications, New York, NY: Oxford University Press, 1993.

[54] S. Hutcherson and W. Ye, "On the squeeze-film damping of micro-resonators in the free-molecule regime," *Journal of Micromechanics and Microengineering,* vol. 14, pp. 1726-1733, 2004.

[55] R. G. Polcawich and J. S. Pulskamp, "Additive Processes for Piezoelectric Materials: Piezoelectric MEMS," in *MEMS materials and Processes Handbook*, New York, NY, Springer, 2011, pp. 273-344.

[56] R. Ghodssi, B. Hanrahan and M. Beyaz, "Microball bearing technology for MEMS devices and integrated microsystems," in *Proceedings of the International Solid-State Sensors, Actuators and Microsystems Conference (TRANSDUCERS),* Beijing, China, 2011.

[57] J. S. Pulskamp, S. S. Bedair, R. G. Polcawich, D. Judy and S. A. Bhave, "Ferroelectric PZT RF MEMS resonators," in *Frequency Control and the European Frequency and Time Forum (FCS), 2011 Joint Conference of the IEEE International* , San Francisco, CA, 2011.

[58] R. Q. Rudy, G. L. Smith, D. L. DeVoe and R. G. Polcawich, "Traveling wave ultrasonic motor using thin-film piezoelectrics," in *Proceedings of the Solid-State*

Sensors, Actuators, and Microsystems Workshop, Hilton Head, SC, 2012.

[59] J. Lee, C. H. Choi, B. H. Park, T. W. Noh and J. K. Lee, "Built-in voltages and asymmetric polarization switching in Pb(Zr,Ti)O3 thin film capacitors," *Applied Physics Letters*, vol. 72, no. 25, pp. 3380-3382, 1998.

[60] F. Giraud, B. Semail and J. T. Audren, "Analysis and phase control of a piezoelectric traveling-wave ultrasonic motor for haptic stick application," *IEEE Transactions on Industry Applications*, vol. 4, pp. 1541-1549, 2003.

[61] T. Sattel, P. Hagedorn and J. Schmidt, "The Contact Problem in Ultrasonic Traveling-Wave Motors," *Journal of Applied Mechanics*, vol. 77, no. 3, pp. 031014-1 - 031014-11, 2010.

[62] M. Dubois and P. Muralt, "PZT Thin FIlm Actuated Elastic Fin Micromotor," *Transactions on Ultrasonics, Ferroelectrics, and Frequency Control*, vol. 45, no. 5, pp. 1169-1177, 1998.

[63] J. S. Pulskamp, S. S. Bedair, R. G. Polcawich, G. L. Smith, J. Martin, B. Power and S. A. Bhave, "Electrode-shaping for the excitation and detection of permitted arbitrary modes in arbitrary geometries in piezoelectric resonators," *IEEE Transactions on Ultrasonics, Ferroelectrics and Frequency Control*, vol. 59, no. 5, pp. 1043-1060, 2012.

[64] N. W. Hagood and A. J. McFarland, "Modeling of a piezoelectric rotary ultrasonic motor," *IEEE Transactions on Ultrasonics, Ferroelectrics, and Frequency Control*, vol. 42, no. 2, pp. 210-224, 1995.

[65] P. Hagedorn, T. Sattel, D. Speziari, J. Schmidt and G. Diana, "The importance of rotor flexibility in ultrasonic traveling wave motors," *Smart Materials and Structures*, vol. 7, pp. 352-368, 1998.

[66] N. W. Hagood, W. H. Chung and A. Flotow, "Modelling of Piezoelectric Actuator Dynamics for Active Structural Control," *Journal of Intelligent Materials, Systems, and Structures*, vol. 1, pp. 327-354, 1990.

[67] K. Tani, M. Suzuki, K. Furuta, T. Sakuhara and T. Ataka, "Development of a new type piezoelectric micromotor," in *International Workshop on Micro Electro Mechanical Systems*, Heidelberg, Germany, 1998.

[68] C. D. Meyer, S. S. Bedair, B. C. Morgan and D. P. Arnold, "High-Inductance-Density, Air-Core, Power Inductors, and Transformers Designed for Operation at 100–500 MHz," *IEEE Transactions on Magnetcis*, vol. 46, no. 6, pp. 2236-2239, 2010.

[69] L. Fan and R. S. Muller, "IC-processed electrostatic micro-motors," in *Proceedings from the Electron Devices Meeting*, San Francisco, CA, 1988.

[70] C. H. Ahn, Y. J. Kim and M. G. Allen, "A planar variable reluctance magnetic micromotor with fully integrated stator and wrapped coils," in *Proceedings from IEEE Micro Electro Mechanical Systems Workshop*, Fort Lauderdale, FL, 1993.

[71] H. Guckel, T. R. Christenson, K. J. Skrobis, T. S. Jung, J. Klein, K. V. Hartojo and I. Widjaja, "A first functional current excited planar rotational magnetic micromotor," in *Proceedings from IEEE Micro Electro Mechanical Systems Workshop*, Fort Lauderdale, FL, 1993.

[72] T. Furuhata, T. Hirano, L. H. Lane, R. E. Fontana, L. S. Fan and H. Fujita, "Outer rotor surface-micromachined wobble motor," in *Proceedings from IEEE Micro Electro Mechanical Systems Workshop*, Fort Lauderdale, FL, 1993.

[73] Y. Gianchandani and K. Najafi, "Batch fabrication and assembly of micromotor-driven mechanisms with multi-level linkages," in *Proceedings from IEEE Micro Electo Mechanical Systems Workshop*, Travemunde, GE, 1992.

[74] S. S. Bedair, J. S. Pulskamp, C. D. Meyer, M. Mirabelli, R. G. Polcawich and B. Morgan, "High-Performance Micromachined Inductors Tunable by Lead Zirconate Titanate Actuators," *IEEE Electron Device Letters,* vol. 33, no. 10, pp. 1483-1485, 2012.

[75] K. Uchino, S. Cagatay, B. Koc, S. Dong, P. Bouchilloux and M. Strauss, "Micro Piezoelectric Ultrasonic Motors," *Journal of Electroceramics,* vol. 13, pp. 393-401, 2004.